Volatile Abundances, Extended Coma Sources, and Nucleus Ice Associations in Comet C/2014 Q2 (Lovejoy)

Neil Dello Russo[1] , Ronald J. Vervack, Jr.[1] , Hideyo Kawakita[2] , Boncho P. Bonev[3] , Michael A. DiSanti[4,5] ,
Erika L. Gibb[6] , Adam J. McKay[3,4] , Anita L. Cochran[7] , Harold A. Weaver[1] , Nicolas Biver[8] , Jacques Crovisier[8] ,
Dominique Bockelée-Morvan[8] , Hitomi Kobayashi[9] , Walter M. Harris[10] , Nathan X. Roth[11,12] , Mohammad Saki[13] , and
Younas Khan[6]

[1] Space Exploration Sector, Johns Hopkins University Applied Physics Laboratory, Laurel, MD 20723, USA
[2] Koyama Astronomical Observatory, Kyoto Sangyo University, Motoyama, Kamigamo, Kita-ku, Kyoto 603-8555, Japan
[3] Department of Physics, American University, Washington, DC 20016, USA
[4] Solar System Exploration Division, Planetary Systems Laboratory, MS 693, NASA Goddard Space Flight Center, Greenbelt, MD 20771, USA
[5] Goddard Center for Astrobiology, NASA Goddard Space Flight Center, Greenbelt, MD 20771, USA
[6] Department of Physics and Astronomy, University of Missouri–St. Louis, Saint Louis, MO 63121, USA
[7] McDonald Observatory, University of Texas at Austin, Austin, TX 78712, USA
[8] LESIA, Observatoire de Paris, Université PSL, CNRS, Sorbonne Université, Université de Paris, 5 place Jules Janssen, F-92195 Meudon, France
[9] Kyoto Nijikoubou, LLP 17-203, Iwakura Minami-Osagicho, Sakyo-ku, Kyoto 606-0003, Japan
[10] Lunar and Planetary Laboratory, University of Arizona, Tucson, AZ, USA
[11] Universities Space Research Association, Columbia, MD 21046, USA
[12] Solar System Exploration Division, Astrochemistry Laboratory Code 691, NASA Goddard Space Flight Center, Greenbelt, MD, 20771 USA
[13] Physics Department, Leach Science Center, Auburn University, Auburn, AL, USA

Abstract

High-resolution infrared spectra of comet C/2014 Q2 Lovejoy were acquired with NIRSPEC at the W. M. Keck Observatory on two post-perihelion dates (UT 2015 February 2 and 3). H_2O was measured simultaneously with CO, CH_3OH, H_2CO, CH_4, C_2H_6, C_2H_4, C_2H_2, HCN, and NH_3 on both dates, and rotational temperatures, production rates, relative abundances, H_2O ortho-to-para ratios, and spatial distributions in the coma were determined. The first detection of C_2H_4 in a comet from ground-based observations is reported. Abundances relative to H_2O for all species were found to be in the typical range compared with values for other comets in the overall population to date. There is evidence of variability in rotational temperatures and production rates on timescales that are small compared with the rotational period of the comet. Spatial distributions of volatiles in the coma suggest complex outgassing behavior. CH_3OH, HCN, C_2H_6, and CH_4 spatial distributions in the coma are consistent with direct release from associated ices in the nucleus and are peaked in a more sunward direction compared with co-measured dust. H_2O spatial profiles are clearly distinct from these other four species, likely due to a sizable coma contribution from icy grain sublimation. Spatial distributions for C_2H_2, H_2CO, and NH_3 suggest substantial contributions from extended coma sources, providing further evidence for distinct origins and associations for these species in comets. CO shows a different spatial distribution compared with other volatiles, consistent with jet activity from discrete nucleus ice sources.

1. Introduction

Ices stored in comets are relics from the formation of the solar system. The degree to which these ices retain their natal composition is uncertain owing to difficulties in pinpointing where and when individual comets formed in the vast regions of the early solar system and how they have subsequently evolved. Information about the origin and evolution of comets can be obtained by studying how ices are stored and associated in the nucleus through the determination of the relative abundances and spatial distributions of these sublimated volatiles in the coma.

The overall comet population is generally represented by two broad dynamical categories: those with orbital inclinations near the ecliptic plane and fed mostly from the scattered Kuiper disk (known as Jupiter-family comets or JFCs), and longer-period comets with random orbital inclinations from the Oort cloud reservoir (known as Oort cloud comets or OCCs). Measurements of coma volatiles suggest that there is substantial chemical diversity within the comet population as a whole, as well as some distinctions between these dynamical classes. For example, studies of hundreds of comets at optical wavelengths indicate a depletion of carbon-chain product species (C_2 and C_3) relative to CN and OH in a significantly higher fraction of JFCs compared with OCCs (A'Hearn et al. 1995; Schleicher et al. 2007; Fink 2009; Langland-Shula & Smith 2011; Cochran et al. 2012). Infrared (IR) studies on a smaller but growing sample of comets (now ∼50) suggest notable similarities in the chemical composition of simple parent volatiles with respect to H_2O between some JFCs and OCCs; however, evidence from the global population indicates more prevalent depletion on average in some of the more volatile species (CO, CH_4, C_2H_6, and C_2H_2) in JFCs compared with OCCs (e.g., Dello Russo et al. 2016a). Our understanding of these trends in parent volatile abundances observed between JFCs and OCCs is evolving as more comets are sampled.

This apparent depletion of carbon-chain product species and volatile parents in JFCs could be explained by a higher degree

of thermal processing on average owing to many more perihelion passages for ices within JFCs compared with OCCs. However, it is also possible that the dominant processes that shape the relative compositions of JFCs and OCCs today occurred before parent ices were incorporated into comets. A study of product species within the large optical database shows no correlation between carbon-chain depletion and dynamical age, providing one line of evidence suggesting that chemical differences at least in some comets are natal (A'Hearn et al. 1995). For example, measured compositions in multiple fragments of 73P/Schwassmann-Wachmann 3 were consistent with each other and the pre-fragmented nucleus, strongly suggesting the retention of its natal composition (Dello Russo et al. 2007; Schleicher & Bair 2011). Dynamical models for the young solar system suggest that OCCs and JFCs may have formed in overlapping regions within the protosolar disk (Gomes et al. 2005; Tsiganis et al. 2005), which is consistent both with the similarities in the composition of parent volatiles between some JFCs and OCCs and with some global differences in average chemistry between JFCs and OCCs in the overall population.

Systematic comparisons of chemical abundances of parent volatiles in comets at IR wavelengths have provided insights into chemical diversity of comets and the relationships among volatile species (e.g., Mumma & Charnley 2011; Dello Russo et al. 2016a; Lippi et al. 2021 and references therein). Although these compositional interrelationships provide information on global molecular associations within the comet population, they do not reveal how ices are stored or associated in the nuclei of comets. Clues to the associations of ices in the nucleus have been obtained at IR wavelengths through the study of spatial distributions of volatiles in the coma (e.g., DiSanti et al. 1999; Dello Russo et al. 2011; Villanueva et al. 2011a; Bonev et al. 2014, 2021; Paganini et al. 2014); however, data are generally not of sufficient quality to perform coma spatial studies of more than a few species with the strongest and most spatially extended emissions. In particular, information on the spatial distributions of C_2H_2, NH_3, and H_2CO in comets from IR studies is sparse.

The 2014/2015 apparition of C/2014 Q2 (Lovejoy) was an exceptional opportunity to determine the volatile abundances and coma spatial distributions for a large suite of volatiles, including weaker, more rarely measured species, in a dynamically evolved OCC. Investigations of C/2014 Q2 (Lovejoy) have already revealed its detailed organic chemistry (Biver et al. 2015) and volatile isotopic ratios (Biver et al. 2016; Shinnaka & Kawakita 2016; Paganini et al. 2017). Other long-term observations show asymmetric gas production around perihelion, with significantly higher productivity after perihelion (Venkataramani et al. 2016; Combi et al. 2018). Here we report IR spectroscopic observations of C/2014 Q2 (Lovejoy) with NIRSPEC at the W. M. Keck Observatory obtained on UT 2015 February 2 and 3 (hereafter all given dates are in UT) a few days after perihelion. Twenty-seven independent determinations of gas rotational temperatures were obtained over these two dates from multiple species, including H_2O, CO, CH_4, C_2H_6, C_2H_2, H_2CO, CH_3OH, and HCN. Production rates and abundances with respect to both H_2O and C_2H_6 are reported for H_2O, CO, CH_4, C_2H_6, C_2H_4, C_2H_2, H_2CO, CH_3OH, NH_3, HCN, and HC_3N. We present strong evidence for the first ground-based detection of C_2H_4 in a comet. A detailed investigation of the distribution of H_2O, CH_4, C_2H_6, C_2H_2, H_2CO, CH_3OH, HCN, NH_3, NH_2, OH, and co-measured dust in the coma is also presented. Lastly, the ortho-to-para ratio (OPR) of H_2O was

determined. The overall composition of C/2014 Q2 (Lovejoy) and the volatile associations revealed by spatial distributions in the coma are compared with those measured in other comets within the high-resolution IR spectroscopy database.

2. Observations

Spectra of C/2014 Q2 (Lovejoy) reported here were acquired with NIRSPEC (McLean et al. 1998) at the W. M. Keck Observatory atop the summit of Maunakea, Hawaii. We used a $24'' \times 0''.432$ slit ($\sim 14,000 \times 250$ km projected at the comet on 2015 February 2 and 3), resulting in a spectral resolving power $(\lambda/\Delta\lambda) \sim 25,000$. NIRSPEC pixels subtend $0''.19$ in the spatial direction, so the spatial sampling at the comet was ~ 110 km pixel^{-1} on February 2 and 3. However, the spatial resolution is limited by the seeing, which was average to below average over each observing period. On February 2 observing conditions were stable with clear skies but with higher-than-typical wind speeds; seeing averaged (in FWHM) $\sim 0''.9$, and there was ~ 3 precipitable millimeters (pr-mm) of water vapor burden in the atmosphere. Conditions were significantly worse and more variable on February 3, with continued high winds and occasional high clouds; seeing averaged $\sim 1''.3$, and there was ~ 6 pr-mm of water vapor in the atmosphere. On February 2 we obtained spectra in three L-band settings (KL1, KL2, and KL3) targeting H_2O, C_2H_6, C_2H_4, C_2H_2, CH_3OH, H_2CO, NH_3, HCN, and HC_3N and one M-band setting (M1) targeting H_2O and CO. On February 3, weather conditions affected efficiency, so spectra were obtained in only two L-band settings (KL4 and KL5) and one M-band setting (M2). A detailed log of our observations is summarized in Table 1.

On February 2 the slit was put into image rotator mode, whereby it was mechanically rotated in order to keep the slit position angle on the comet constant and along the extended heliocentric radius vector (position angle = $69°.6$). On February 3, the same approximate slit orientation in image rotator mode was used for the M2 setting (position angle = $68°.8$). For the two L-band settings on February 3, however, the slit was kept in rotator stationary mode such that it was mechanically stationary and the slit position angle on the comet changed with time. This resulted in the position angle ranging from $106°.8$ to $80°.7$ and from $74°.6$ to $61°.7$ for settings KL4 and KL5, respectively. This still resulted in the slit orientation remaining close to the extended heliocentric radius vector for these settings. The decision to use rotator stationary mode for settings KL4 and KL5 on February 3 was the result of small grating bobbles (where the grating position moves slightly in the spectral dimension during a scan before returning to its original position) that occasionally occurred in image rotator mode on February 2, rendering those scans unusable, coupled with efficiency losses due to poorer observing conditions on February 3. On both dates the Sun–Comet–Observer (i.e., solar phase) angle was $\sim 50°$.

All spectra were acquired using successive sequences of four scans. During a sequence of scans, the telescope was nodded $12''$ between A and B positions ($\pm 6''$ from the center of the $24''$ long slit) in an ABBA pattern, keeping the comet on the slit for all integrations. Multiple ABBA sequences were obtained in each setting, with the range of clock time in UT and the mid-UT (in parentheses) listed in Table 1. The total on-source integration time (I_{time}) per setting is a fraction of the clock time based on the efficiency of the observations (Table 1). On February 2, for the L-band settings where direct visual (SCAM)

Table 1
Observing Log for Observations of C/2014 Q2 (Lovejoy)

UT Date[a]	UT Time[a]	R_h [b] (au)	Δ [b] (au)	$d\Delta/dt$ [b] (km s^{-1})	Grating Setting[c]	ν_c [c] (cm^{-1})	Volatile Targets	Lines Used[d]	I_{time} [e] (minutes)
Feb 2	4:46–5:40 (5:13)	1.291	0.794	+33.1	KL3	2792	H_2CO	34	36
						2924	C_2H_6	10	
						3056	CH_4	4	
							CH_3OH	3	
							C_2H_4	7	
						3321	H_2O	16	
							HCN	14	
							C_2H_2	4	
							NH_3	2	
							HC_3N	5	
						3453	H_2O	41	
							NH_3	3	
Feb 2	5:53–6:15 (6:04)	1.291	0.795	+33.2	KL1	2854	CH_3OH	39	8
							H_2CO	3	
						2983	C_2H_6	14	
							CH_3OH	9	
							CH_4	4	
						3112	CH_4	1	
							C_2H_4	8	
						3241	C_2H_2	2	
							NH_3	1	
						3370	H_2O	31	
							NH_3	5	
						3499	H_2O	20	
Feb 2	6:17–6:57 (6:37)	1.291	0.795	+33.2	KL2	2762	H_2CO	30	24
						2893	C_2H_6	30	
						3024	CH_4	2	
							CH_3OH	8	
						3285	H_2O	6	
							HCN	7	
							C_2H_2	12	
							NH_3	2	
						3416	H_2O	37	
							NH_3	4	
Feb 2	7:15–7:37 (7:26)	1.291	0.796	+33.3	M1	2143	H_2O	13	7
							CO	8	
Feb 3	5:27–6:24 (5:56)	1.292	0.814	+33.4	KL4	2787	H_2CO	31	28
						2919	C_2H_6	10	
						3051	CH_4	4	
							CH_3OH	2	
							C_2H_4	4	
						3315	H_2O	8	
							HCN	11	
							C_2H_2	2	
							NH_3	2	
						3447	H_2O	24	
Feb 3	6:39–7:13 (6:56)	1.292	0.815	+33.5	KL5	2852	CH_3OH	37	14
							H_2CO	3	
						2981	C_2H_6	16	
							CH_3OH	9	
							CH_4	3	
						3368	H_2O	19	
							NH_3	1	
						3497	H_2O	4	
Feb 3	7:18–7:28 (7:23)	1.292	0.815	+33.5	M2	2009	H_2O	4	2.5
						2143	H_2O	7	
							CO	8	

Notes.
[a] Dates and times in UT (2015) are given as the range (and the midpoint within a range) for the given grating setting.
[b] The heliocentric distance (R_h), geocentric distance (Δ), and geocentric velocity ($d\Delta/dt$).
[c] NIRSPEC L-band settings (KL1, KL2, KL3, KL4, KL5) contain six orders (orders 21–26 for KL2, KL3, and KL4; orders 22–27 for KL1 and KL5) with $\sim$40–50 cm^{-1} spectral grasp per order, M1 contains a single order (order 16), and M2 contains two orders (orders 15 and 16) with $\sim$35 cm^{-1} spectral grasp per order. ν_c is the central wavenumber of a particular order within a given setting.
[d] The total number of lines used in determining line fluxes, production rates, or upper limits for each species within a grating setting. Emissions that are a blend of more than one line from the same species are counted only once.
[e] On-source integration time.

guiding on the target was employed, a total I_{time} of 1 minute per scan was used (4 minutes for each ABBA sequence). Only off-axis guiding is possible with NIRSPEC in M-band settings. This method is typically less efficient at keeping the comet in the slit for long periods of time, largely due to inaccuracies in comet rates, possibly from nongravitational effects. Any variability in the sky signal in M band is a larger fraction of the comet signal compared to L band, so a shorter I_{time} of 30 s was used per scan (2 minutes for each ABBA sequence) for the M-band setting. On February 3, owing to more rapidly changing sky conditions, only 30 s per scan for L-band settings and 15 s per scan for the M-band setting were used. In order to convert comet spectra from counts to flux units, spectra of bright IR flux standard BS 1641 were obtained through the widest NIRSPEC slit ($24'' \times 0.''72$). Flat-field and dark frames were obtained either directly before or after each comet or star setting to allow correction of pixel-to-pixel and sensitivity variations within each order and setting.

3. Data Analysis

General data processing techniques for high-resolution IR studies of comets are explained in detail elsewhere (e.g., Bonev 2005; Dello Russo et al. 2006; Villanueva et al. 2009; DiSanti et al. 2014); here we discuss aspects relevant to the C/2014 Q2 (Lovejoy) data processing. Column burdens of terrestrial atmospheric absorbers are obtained through comparison of sky line positions, widths, and intensities with modeled telluric absorbance spectra. The fully resolved atmospheric transmittance function is then used to correct each measured line flux for telluric extinction at the Doppler-shifted frequency of the line. We employed the Planetary Spectrum Generator (PSG; https://psg.gsfc.nasa.gov/; Villanueva et al. 2015, 2018) to generate transmittance models. The best-fit model is obtained through an iterative process using an algorithm developed previously for interpreting the atmosphere of Mars (Villanueva et al. 2008) and adapted to comet spectra (DiSanti et al. 2016). The position of the comet can drift by a few pixels during multiple scan sequences obtained over hours of clock time; therefore, each individual comet frame within a grating setting was registered to a common spatial position in order to best preserve the spatial distribution of coma species. In the case of C/2014 Q2 (Lovejoy), this is straightforward because the comet continuum is clearly visible in all orders in a single A–B difference, allowing the continuum position of each A and B spectrum to be determined by a Gaussian fit to the nearest 1/10 of a pixel.

Once spectral frames are spatially registered, spectra are extracted by summing over the desired spatial extent (i.e., number of pixels or rows). An example of a flux-calibrated, nine-row spectral extract centered on the peak of the gas emission (which is only slightly offset from the peak of the dust continuum—in most cases by less than a pixel) is shown in Figure 1. The modeled telluric spectrum is scaled to continuum points in regions of the comet spectrum that have high atmospheric transmittance and are also free of any known or apparent cometary molecular emissions (Figure 1). In this way, gas-phase molecular emissions are isolated from dust emission by subtracting the modeled telluric spectrum from the comet spectrum row by row, yielding the net cometary molecular emission intensities along the slit (shown in the bottom of the panels in Figure 1, and on the top of panels in Figures 2, 3, 4, A1, A2, A3, A4, along with the estimated $\pm 1\sigma$ stochastic noise envelope). These emissions represent the line intensities after
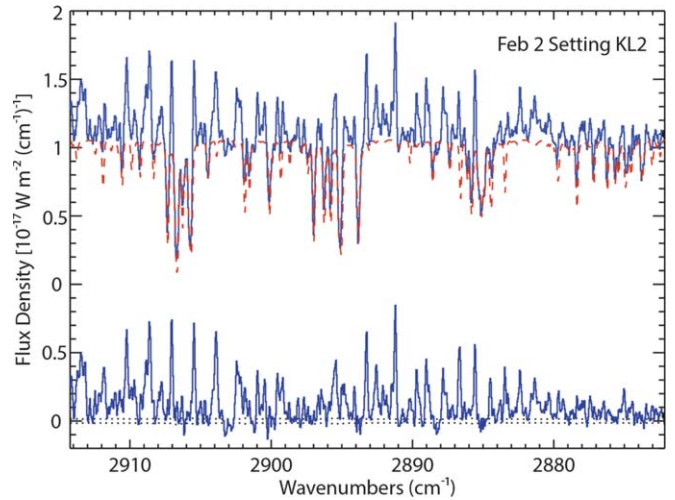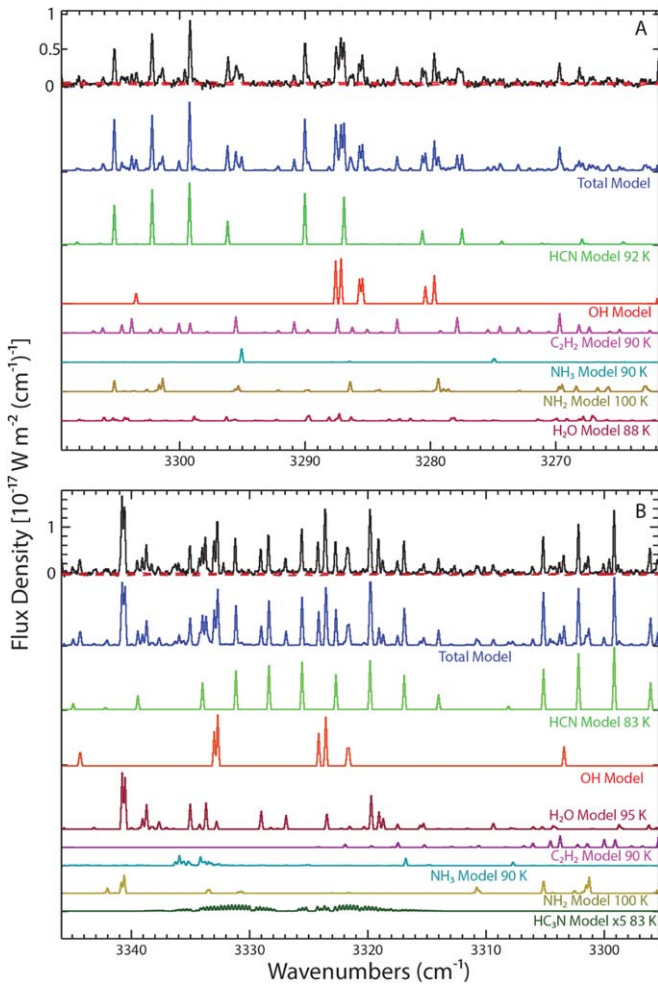

Figure 1. Flux-calibrated, high-resolution ($\lambda/\Delta\lambda \sim 25{,}000$) spectral extracts and residuals in C/2014 Q2 (Lovejoy) in setting KL2 order 22. The spectrum is co-added over a 3 spectral $\times$ 9 spatial pixel extract ($0.''432 \times 1.''71$) centered on the peak of the gas emission. The solid blue trace at the top of the panel is the comet spectrum with the best-fit synthetic atmospheric model superimposed (dashed red trace). Molecular lines from the comet are seen as emissions in the comet spectrum above the atmospheric model. The Solid blue trace on the bottom of the panel is the continuum-subtracted spectral residuals. The dotted black curves superimposed on the comet residuals represent the estimated $\pm 1\sigma$ channel-by-channel photon noise envelope.

transmission through the atmosphere as convolved with the instrument resolution. The true flux incident at the top of the terrestrial atmosphere for each line is derived within a given aperture by dividing the observed integrated line flux by the monochromatic transmittance at the Doppler-shifted line frequency (Tables A1–A7). We note that the position of the continuum baseline level has an uncertainty associated with the stochastic noise envelope. Although the uncertainty in the local continuum baseline is small compared with the total continuum flux, it can be a significant but difficult-to-quantify source of uncertainty in the measured fluxes of weak cometary volatile emission lines. Figure 1 illustrates the difficulties and inherent uncertainties in fitting the continuum baseline, especially in spectral regions where many cometary and atmospheric lines are present.

Molecular production rates, rotational temperatures, and H_2O OPRs are derived from the line fluxes within 3 spectral $\times$ 9 spatial pixel extracts ($0.''432 \times 1.''71$) centered on the peak of the gas emissions by applying a coma model that assumes spherical symmetric gas outflow with uniform velocity. In this case we assume an outflow velocity $v = 800 \, m \, s^{-1}$ on February 2 and 3 based on radio measurements of the highest signal-to-noise ratio (S/N) CH_3OH lines measured pre-perihelion, about 2 weeks earlier than these observations but at approximately the same heliocentric distance (Biver et al. 2015). Because the transit time for molecules released from the nucleus to reach the edge of the field of view in the plane of the sky is short compared with the photodissociation lifetime of most of the measured molecules (NH_3 and H_2CO may be exceptions), the derived production rates are proportional to the assumed outflow velocity. Thus, errors in assumed outflow velocity affect absolute production rates derived for each species but do not significantly affect OPRs, rotational temperatures, or relative abundances. Gas coma asymmetries can affect production rates derived assuming spherical symmetry; however, errors from this assumption are expected to be small in most cases, as production rates from either side of the nucleus
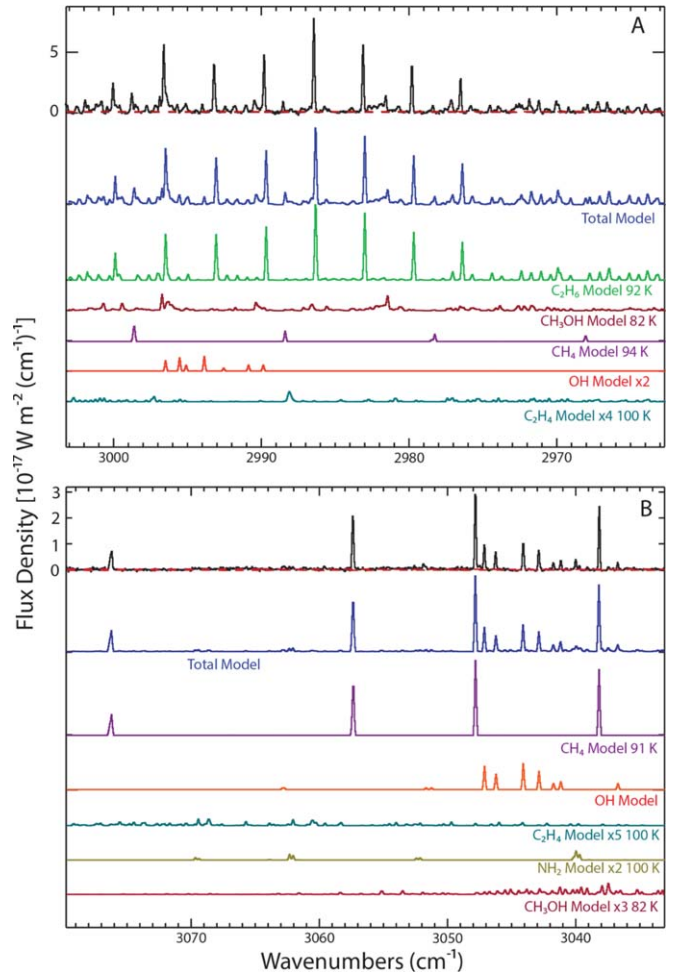
Figure 2. Flux-calibrated, high-resolution ($\lambda/\Delta\lambda \sim 25,000$) spectral residuals and best-fit fluorescence models for C/2014 Q2 (Lovejoy) on (a) February 2, setting KL2 order 25, and (b) February 2, setting KL3 order 25. On the top of each frame are spectral residuals co-added over 3 spectral $\times$ 9 spatial pixel extracts ($0\rlap{.}''432 \times 1\rlap{.}''71$) centered on the peak of the gas emission. The dashed red curves superimposed on the comet residuals represent the estimated $\pm 1\sigma$ channel-by-channel photon noise envelope. The solid blue curves directly below the spectral residuals are the total best-fit fluorescence models convolved to the resolution of the comet spectra including all molecules. Color traces below this are the best-fit fluorescence models at the derived or assumed rotational temperatures for each individual molecule. Zoomed-in regions of these spectra are given in Figure A4.

Figure 3. Similar to Figure 2, but for (a) February 2, setting KL1 order 23, and (b) February 2, setting KL3 order 23.

are averaged (Xie & Mumma 1996). Similarly, variations in outflow velocities in the sunward versus antisunward direction are expected to have only a minor influence on the shape of volatile spatial profiles and should similarly affect the spatial profiles of parents released directly from the nucleus.

Production rates derived from nucleus-centered extracts are always underestimated owing to slit losses that suppress the expected fraction of molecules within such an extract compared with the idealized model. Therefore, a correction, referred to as the multiplicative growth factor, is applied using regions offset from the nucleus where the model is less affected by slit losses such as seeing, any drift perpendicular to the slit length, and optical depth effects if they are important (e.g., Dello Russo et al. 1998; DiSanti et al. 2001; Bonev 2005; Villanueva et al. 2011a). The multiplicative growth factors that are used to obtain slit-loss-corrected global production rates for each line

are given in Table A8. Multiplicative growth factors are a representation of how molecular fluxes are projected along the slit, with larger values reflecting more extended emission. Slit losses are basically the same for all species sampled within the same setting when differences between the peak flux positions of these volatiles are small compared to the slit width. This is the case for C/2014 Q2 Lovejoy, so multiplicative growth factors are directly comparable for species sampled within the same setting. For species with lines of insufficient number or strength to enable an independent determination of multiplicative growth factors (e.g., C_2H_4 and HC_3N), values are either adopted from those measured for other species obtained within the same order (HCN in the case of HC_3N) or assigned a reasonable value based on other species observed within that setting (C_2H_6 in the case of C_2H_4).

Derived production rates are based on temperature-dependent fluorescence efficiencies (g-factors) for individual emissions of each species. Fluorescence efficiencies for CO, HCN, HC_3N, and C_2H_2 are based on simple linear models. For other molecules, g-factors were determined as follows: CH_3OH ν_2 band (DiSanti et al. 2013), with other CH_3OH lines derived from the PSG (Villanueva et al. 2015, 2018), H_2O (Dello Russo et al. 2004; Villanueva et al. 2012, 2018), H_2CO (DiSanti et al. 2006), C_2H_6 (Dello Russo et al. 2001; Villanueva et al. 2011b, 2018), NH_3 (Pine & Dang-Nhu 1993; Kleiner et al. 1999; Villanueva et al. 2018), CH_4 (Gibb et al. 2003), and C_2H_4 at
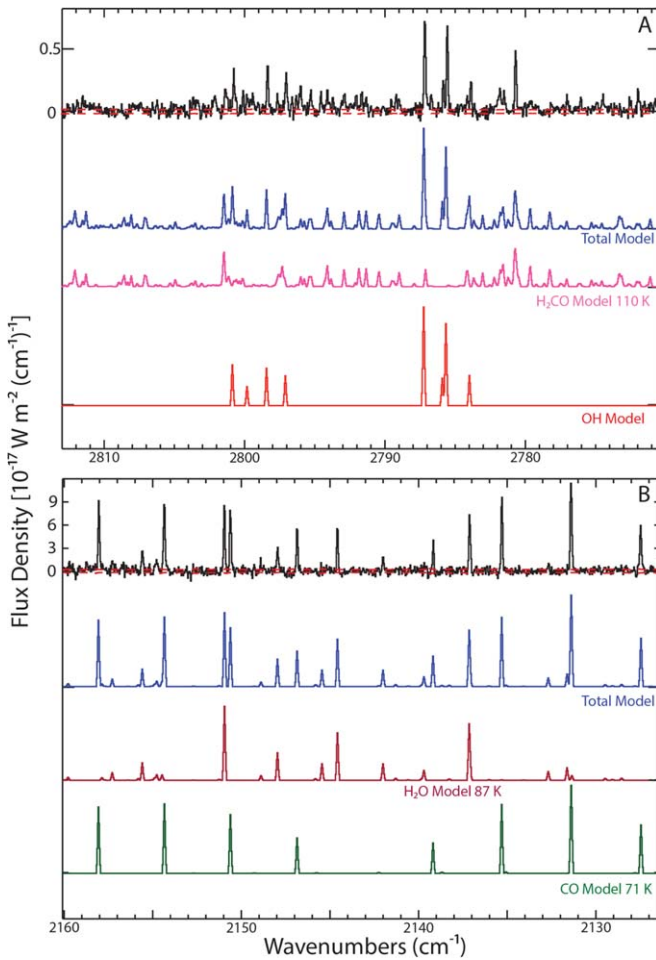
Figure 4. Similar to Figure 2, but for (a) February 2, setting KL3 order 21, and (b) February 2, setting M1 order 16.

$T_{rot} = 100$ K (Villanueva et al. 2018). Production rates and g-factors for each individually measured emission line are given in Tables A1–A7.

Rotational temperatures (Section 3.1), H_2O OPRs (Section 3.2), and production rates (Section 3.3) for each species are determined via a line-by-line excitation analysis, which is detailed in the literature (e.g., Dello Russo et al. 2004; Bonev 2005; Villanueva et al. 2011a; DiSanti et al. 2016 and references therein). Once the continuum and atmospheric model fits are optimized, fluxes are determined from the residual (i.e., continuum-subtracted) spectrum for each emission line used in this analysis. The ratio F_{line}/g_{line} between measured line flux (F_{line}) and the temperature-dependent emission efficiency (g-factor, g_{line}) is proportional to the gas column density. Rotational temperatures depend on the relative intensities of spectral lines and are obtained via zero slope excitation analysis, for which F_{line}/g_{line} is independent of rotational excitation energy (Section 3.1), while the variance around the line-by-line F_{line}/g_{line} measurements is minimized (Bonev et al. 2014). With rotational temperature constrained, the production rate of a given species can be determined independently from each individual line. The mean of these independent retrievals is the best measure of the final production rate, also accounting for slit losses and the morphologies of the spatial profiles (Section 3.4). Importantly, line-by-line analysis includes evaluation of both stochastic and systematic uncertainties, discussed in Sections 3.1–3.3. Tables A1–A7 show the parameters and measured quantities for each line used in the analysis.

A complementary technique used to obtain production rates and rotational temperatures in high-resolution IR data is minimizing the spectral difference (measured minus modeled spectrum) within an entire order through a global fitting of fluorescence models to comet spectra. Bonev et al. (2014) demonstrated that in the absence of systematic uncertainties (e.g., uncertainty in the branching ratios in computing fluorescent g-factors, errors propagated from telluric modeling, etc.) the results of line-by-line and global fit methods should be highly consistent. For additional validation, we therefore applied a Levenberg–Marquardt χ^2 minimization fit (e.g., Villanueva et al. 2008) to independently derive rotational temperatures and production rates in the spectrally dense region of order 25 setting KL3. These results agreed within uncertainties to the values derived by line-by-line analysis used here. Note, however, that global fits are restricted to only stochastic uncertainties in retrieved parameters. An example of a spectral fit with minimized residuals (spectrum–model) is shown in Figure A5 in the Appendix.

More detailed discussion related to the determination of specific parameters is contained in the following subsections.

3.1. Rotational Temperatures

In cases where it is possible to measure multiple strong lines of a given molecule, a rotational temperature (T_{rot}) is determined from a Boltzmann analysis of the relative intensities of these individual lines (e.g., Dello Russo et al. 2004; Bonev 2005; Villanueva et al. 2011a; Bonev et al. 2014). Because the fluxes of individual rovibrational lines are temperature dependent, determinations of rotational temperatures are needed to constrain production rates of coma volatiles. Twenty-seven independent determinations of gas rotational temperatures were obtained within 3 spectral × 9 spatial pixel extracts ($0\rlap{.}''432 \times 1\rlap{.}''71$) centered on the peak of the gas emissions on both dates (the number of determinations per molecule is in parentheses): H_2O (7), C_2H_6 (5), CH_4 (3), CH_3OH (3), HCN (3), H_2CO (3), CO (2), and C_2H_2 (1) (Table 2). Derived rotational temperatures for a given molecule are determined independently for each grating setting and can include lines from multiple orders within a setting. For settings where a rotational temperature could not be derived for a particular molecule because an insufficient number of strong lines are detected, a value is assumed based either on measurements for that molecule in other settings or on values for simultaneously measured H_2O, CH_3OH, C_2H_6, or HCN (assumed T_{rot} values in Table 2 are those without listed uncertainties).

Uncertainties in T_{rot} are determined as follows. At the derived T_{rot} for a particular molecular species, the ratio F_{line}/g_{line} (where F_{line} is the line flux and g_{line} is the line g-factor; see Tables A1–A7) should be constant for all emissions spanning any range of upper-state rotational energy (E_u) (i.e., a graph of F_{line}/g_{line} vs. E_u for all emissions will have a slope of zero; see Dello Russo et al. 2004). For emission features made up of multiple lines, E_u is determined by the average of individual line energies weighted by the g-factor at that temperature. Uncertainties in F_{line} are determined by two factors: The first is the S/N for each emission feature within a 3 spectral × 9 spatial pixel spectral residual extract based on the photon noise (stochastic error) in the data. Uncertainties for F_{line} in Tables A1–A7 include only stochastic error in order to show the measured S/N for each emission feature. The second is an

Table 2
Rotational Temperatures, Production Rates, and Abundances in
C/2014 Q2 (Lovejoy)

Molecule	T_{rot} (K)[a]	Q (10^{27} s^{-1})	Q/Q(H_2O)%	Q/Q(C_2H_6)
	UT 2015 Feb 02 4:46−5:40 Setting KL3			
H_2O	95 ± 3	634 ± 52	100	123 ± 13
CH_4	91 ± 3	4.73 ± 0.37	0.75 ± 0.04	0.92 ± 0.09
C_2H_6	90 ± 10	5.15 ± 0.61	0.81 ± 0.09	1
C_2H_4	100	1.20 ± 0.36	0.19 ± 0.06	0.23 ± 0.07
C_2H_2	90	1.06 ± 0.11	0.17 ± 0.02	0.21 ± 0.03
H_2CO	110 ± 6	2.12 ± 0.18	0.33 ± 0.02	0.41 ± 0.04
NH_3	90	4.77 ± 1.30	0.75 ± 0.20	0.93 ± 0.26
HCN	83 ± 2	1.20 ± 0.09	0.19 ± 0.01	0.23 ± 0.02
HC_3N	83	$<0.027\ (3\sigma)$	$<0.0043\ (3\sigma)$	$<0.0052\ (3\sigma)$
	UT 2015 Feb 02 5:53−6:15 Setting KL1			
H_2O	90 ± 2	588 ± 26	100	137 ± 9
CH_3OH	82 ± 5	11.0 ± 0.7	1.87 ± 0.12	2.57 ± 0.20
H_2CO	110	1.71 ± 0.47	0.29 ± 0.08	0.40 ± 0.11
CH_4	94 ± 4	4.52 ± 0.22	0.77 ± 0.04	1.06 ± 0.07
C_2H_6	$92\ ^{+8}/_{-7}$	4.28 ± 0.26	0.73 ± 0.05	1
C_2H_4	100	1.47 ± 0.35	0.25 ± 0.06	0.34 ± 0.08
NH_3	90	3.09 ± 0.50	0.53 ± 0.09	0.72 ± 0.13
	UT 2015 Feb 02 6:17−6:57 Setting KL2			
H_2O	88 ± 3	516 ± 31	100	146 ± 13
CH_3OH	$70\ ^{+15}/_{-10}$	8.22 ± 1.20	1.59 ± 0.24	2.33 ± 0.37
H_2CO	$103\ ^{+5}/_{-4}$	1.50 ± 0.08	0.29 ± 0.02	0.42 ± 0.03
CH_4	91	4.49 ± 0.72	0.87 ± 0.14	1.27 ± 0.22
C_2H_6	95 ± 7	3.53 ± 0.27	0.69 ± 0.06	1
C_2H_2	$90\ ^{+11}/_{-9}$	0.67 ± 0.06	0.13 ± 0.01	0.19 ± 0.02
NH_3	90	4.08 ± 0.59	0.79 ± 0.12	1.16 ± 0.18
HCN	$92\ ^{+5}/_{-4}$	0.98 ± 0.05	0.19 ± 0.01	0.28 ± 0.02
	UT 2015 Feb 02 7:15−7:37 Setting M1			
H_2O	87 ± 8	730 ± 74	100	
CO	71 ± 10	14.2 ± 1.9	1.94 ± 0.28	
	UT 2015 Feb 03 5:27−6:24 setting KL4			
H_2O	101 ± 5	824 ± 133	100	137 ± 23
CH_3OH	100	11.2 ± 2.3	1.35 ± 0.23	1.85 ± 0.39
H_2CO	$122\ ^{+8}/_{-7}$	2.44 ± 0.40	0.30 ± 0.03	0.41 ± 0.07
CH_4	110 ± 20	6.17 ± 1.55	0.75 ± 0.16	1.03 ± 0.26
C_2H_6	113 ± 17	6.01 ± 1.30	0.73 ± 0.12	1
C_2H_4	100	2.01 ± 0.88[b]	0.24 ± 0.10	0.33 ± 0.15
C_2H_2	110	0.66 ± 0.12	0.080 ± 0.010	0.11 ± 0.02
NH_3	110	5.60 ± 1.72	0.68 ± 0.19	0.93 ± 0.29
HCN	97 ± 12	1.23 ± 0.21	0.15 ± 0.02	0.20 ± 0.04
	UT 2015 Feb 03 6:39−7:13 Setting KL5			
H_2O	$82\ ^{+5}/_{-4}$	571 ± 90	100	168 ± 12
CH_3OH	69 ± 4	10.3 ± 1.6	1.80 ± 0.11	3.04 ± 0.21
H_2CO	100	0.90 ± 0.22	0.16 ± 0.03	0.27 ± 0.05
CH_4	85	3.88 ± 0.66	0.68 ± 0.07	1.14 ± 0.12
C_2H_6	$85\ ^{+10}/_{-11}$	3.39 ± 0.54	0.59 ± 0.05	1
NH_3	85	3.55 ± 0.82	0.62 ± 0.11	1.05 ± 0.19
	UT 2015 Feb 03 7:18−7:28 Setting M2			
H_2O	88 ± 5	807 ± 103	100	
CO	58 ± 8	19.3 ± 2.6	2.39 ± 0.29	

Notes.
[a] Derived (values with uncertainties) or assumed rotational temperatures.
[b] Reported formal value. It should be considered a 3σ upper limit ($Q_{C2H4} < 4.6 \times 10^{27}$ molecules s^{-1}).

additional 5% uncertainty in F_{line}, which is applied to each emission feature to account for uncertainties in the continuum baseline fit and line g-factors. This 5% uncertainty is somewhat arbitrary because these additional uncertainties are difficult to quantify, but it prevents excessive weighting of the strongest emission lines where these uncertainties dominate stochastic uncertainties. Both of these factors propagate into the uncertainties for F_{line}/g_{line} when determining rotational temperatures. The weighted variance of point-by-point F_{line}/g_{line} values from the mean of all emissions (standard uncertainty) is usually (but not always) more important than the stochastic uncertainty represented by the size of the individual F_{line}/g_{line} error bars when determining the uncertainty of T_{rot}. The larger of the standard and stochastic uncertainty is used to define the T_{rot} uncertainty (1σ). For all assumed rotational temperatures in Table 2, ± 10 K uncertainties are assigned.

3.2. Water Ortho-to-para Ratios

Multiple lines from both nuclear spin species (ortho and para) of H_2O were detected within each of the grating settings, allowing seven independent determinations of the OPR. Tables A1–A7 show the assignments (ortho, para, or blend) for each H_2O line. H_2O emissions that were characterized as blends (unblended species are defined as >90% pure ortho or para) were not used for OPR determinations. OPRs were determined from a weighted average of line-by-line production rates determined independently for pure ortho and pure para emissions. As with rotational temperatures, the larger value of stochastic uncertainty versus standard uncertainty of the weighted mean of individual lines was used to determine uncertainties in OPRs (e.g., Dello Russo et al. 2005).

3.3. Production Rates and Relative Abundances

Absolute and relative production rates in C/2014 Q2 (Lovejoy) on both dates are given in Table 2. Global absolute production rates listed for each species are corrected for slit losses and determined from a weighted average of those derived independently for all detected and unblended lines (Tables A1–A7), with the number of lines used in each case given in Table 1. Many more emissions appear in the spectra that are blends of multiple species. The degree of blending is determined by fluorescence models, with the g-factors for each line contributing to an emission feature weighted by the abundance of the contributing species. Blended emissions were not used in the analysis unless a single molecule dominated the blend at ∼>90%. In cases where minor blends were used, a correction was applied for the small contributions from other species. To get the most complete picture of relative abundances in C/2014 Q2 (Lovejoy), we present abundance ratios relative to both a polar (H_2O) and a nonpolar (C_2H_6) molecule (e.g., Bonev et al. 2021). The relative abundances given by a weighted average for all independent measurements are given in Table 3.

Uncertainties in derived absolute production rates, as is the case with rotational temperatures and OPRs, are most often dominated by line-by-line deviations between the best-fit fluorescence model and the data. Thus, reported uncertainties in absolute production rates reflect not only photon noise (including an assumed 5% continuum baseline uncertainty) but also the standard uncertainty from the weighted mean of individual line measurements and the effects of small number

Table 3
C/2014 Q2 (Lovejoy) Abundances Compared with the Comet Population

Molecule	X/H$_2$O (%)[a]	Typical Comet Mixing Ratios (%)[b]	X/C$_2$H$_6$[a]
H$_2$O			143 ± 7
CO	2.16 ± 0.20	1.4–8.8	
CH$_4$	0.75 ± 0.03	0.52–1.04	1.04 ± 0.05
C$_2$H$_6$	0.68 ± 0.03	0.34–0.76	
C$_2$H$_2$	0.11 ± 0.02	0.07–0.20	0.16 ± 0.03
H$_2$CO	0.29 ± 0.03	0.13–0.49	0.39 ± 0.03
NH$_3$	0.64 ± 0.06	0.22–1.38	0.92 ± 0.08
HCN	0.18 ± 0.01	0.15–0.27	0.25 ± 0.02
CH$_3$OH	1.76 ± 0.08	1.50–2.62	2.64 ± 0.19
C$_2$H$_4$	0.22 ± 0.04		0.32 ± 0.06
HC$_3$N	<0.0043		<0.0052
Hydrocarbon[c]	1.54 ± 0.10	1.01–2.02	
HCO[d]	2.04 ± 0.12	1.93–2.89	
N[e]	0.92 ± 0.05	0.39–1.61	
Other Mixing Ratios[a]			
CH$_3$OH/H$_2$CO	5.40 ± 0.74	7–23	
NH$_3$/HCN	4.17 ± 0.49	1.1–7.5	
HC$_3$N/HCN	<0.023		

Notes.
[a] Abundances (weighted averages of all measurements in Table 2) with respect to H$_2$O are in %, whereas abundances with respect to C$_2$H$_6$ and "other mixing ratios" are the actual ratio. HC$_3$N upper limits are 3σ based on the standard uncertainty of the mean.
[b] Typical mixing ratios with respect to H$_2$O are from Dello Russo et al. (2016).
[c] Hydrocarbon mixing ratios are (CH$_4$ + C$_2$H$_6$ + C$_2$H$_2$)/H$_2$O.
[d] HCO mixing ratios are (CH$_3$OH + H$_2$CO)/H$_2$O.
[e] N mixing ratios are (NH$_3$ + HCN)/H$_2$O.

statistics. In addition, we estimate other uncertainty contributions to absolute production rates. On February 2 and for the M2 setting on February 3, the standard uncertainty of the mean from independent flux calibration measurements determines the uncertainty. In this case we took two ABBA sets on the star in each setting, resulting in up to eight viable independent flux calibration measurements. Uncertainties in stellar flux calibrations for these settings were 7%, 3%, 3%, 6%, and 10% for KL3, KL1, KL2, M1, and M2, respectively. Star calibrations for settings KL4 and KL5 occurred when weather conditions worsened significantly and never improved on February 3. Therefore, for settings KL4 and KL5 we adopt, respectively, the flux calibrations from almost identical settings KL3 and KL1 on February 2 with an assumed uncertainty of 15% in these settings. The reasonable agreement of values obtained for flux calibrations in order 16 for settings M1 and M2 suggests that the estimated 15% uncertainties are reasonable. Uncertainties in flux calibration apply only to derived absolute (global) production rates and not to rotational temperatures, OPRs, and relative abundances, as they are determined from lines within the same grating setting. Uncertainties in multiplicative growth factors are determined from the Q-curve produced by the sum of all lines of a given species within each order of each setting and ranged from ∼2% to 7% for these data. Uncertainties in rotational temperature are also included by determining the range in derived production rates encompassed by uncertainties in T_{rot}; these ranged from ∼1% to 20% depending on the molecule and setting.

3.4. Spatial Distributions of Volatiles and Dust in the Coma of C/2014 Q2 (Lovejoy)

The spatial distribution of the flux of volatile emissions along the slit (spatial profiles) can give clues as to how different molecular ices may have been associated or segregated in the nucleus prior to their release into the coma. The high S/Ns of emission lines, even in slit positions offset from the nucleus, enabled the spatial profiles to be evaluated for nine parent volatiles: H$_2$O, CO, CH$_3$OH, C$_2$H$_6$, CH$_4$, C$_2$H$_2$, HCN, H$_2$CO, and NH$_3$ (Figures 5–7), as well as product species NH$_2$ and OH (Figure A6). Spatial profiles for each species (shown in Figures 5, 6, 7, A6) are a sum of all measured lines for that species within a given order of a grating setting. Four parameters are evaluated for the spatial distributions of volatile species: (1) the multiplicative growth factor, (2) the difference in the width of the volatile spatial profile (as measured from the half-width at half-maximum of the best-fit Gaussian to the spatial profile) with respect to the width of the spatial profile of the co-measured dust continuum, (3) the difference in the peak position of the volatile spatial profile (as represented by the peak in the Gaussian fit) with respect to the peak position of the spatial profile of the co-measured dust continuum, and (4) the degree of symmetry of the spatial profile as measured by the ratio of sunward to antisunward flux along the slit (between a projected distance ∼300–2400 km from the peak of the profile on both sides of the slit). Co-adding all lines of a particular molecule within an order of a setting gives a spatial profile from which these measured parameters are determined (Table A8). Values of these parameters by date are determined by a weighted average of values for each combined profile in a given setting and order on that date (Table 4). Uncertainties in these spatial profile parameters by date for each species are determined by the standard uncertainty from the mean of values from each measured co-added profile within a setting (Tables 4, A8).

4. Results

As an illustration of how molecular emission features are assigned and blends are identified, residual spectra are shown side by side with the total model and models for individual molecular components convolved to the spectral resolution of the data (Figures 2, 3, 4, A1, A2, A3, A4). These comparisons show the relative strengths and number of emissions for each species and how each spectral region is subject to blends of two or more molecular species. In this section the results for rotational temperatures, production rates, OPRs, and spatial profile properties obtained for individual molecules are presented for the two dates and seven time-blocks (represented by the individual NIRSPEC settings) where measurements were obtained (Table 1). Interpretation of these results and discussion of the implications are given in Section 5.

4.1. Dust

Analysis for both dates show that in general dust spatial profiles are narrower and more asymmetric (enhanced in the antisunward direction) compared to spatial profiles of co-measured volatiles (Figures 5–8, 10, A7; Table A8). Peak positions and widths of volatile spatial profiles are reported with respect to co-measured dust profiles within each setting (Table A8) and averaged for each date (Table 4).
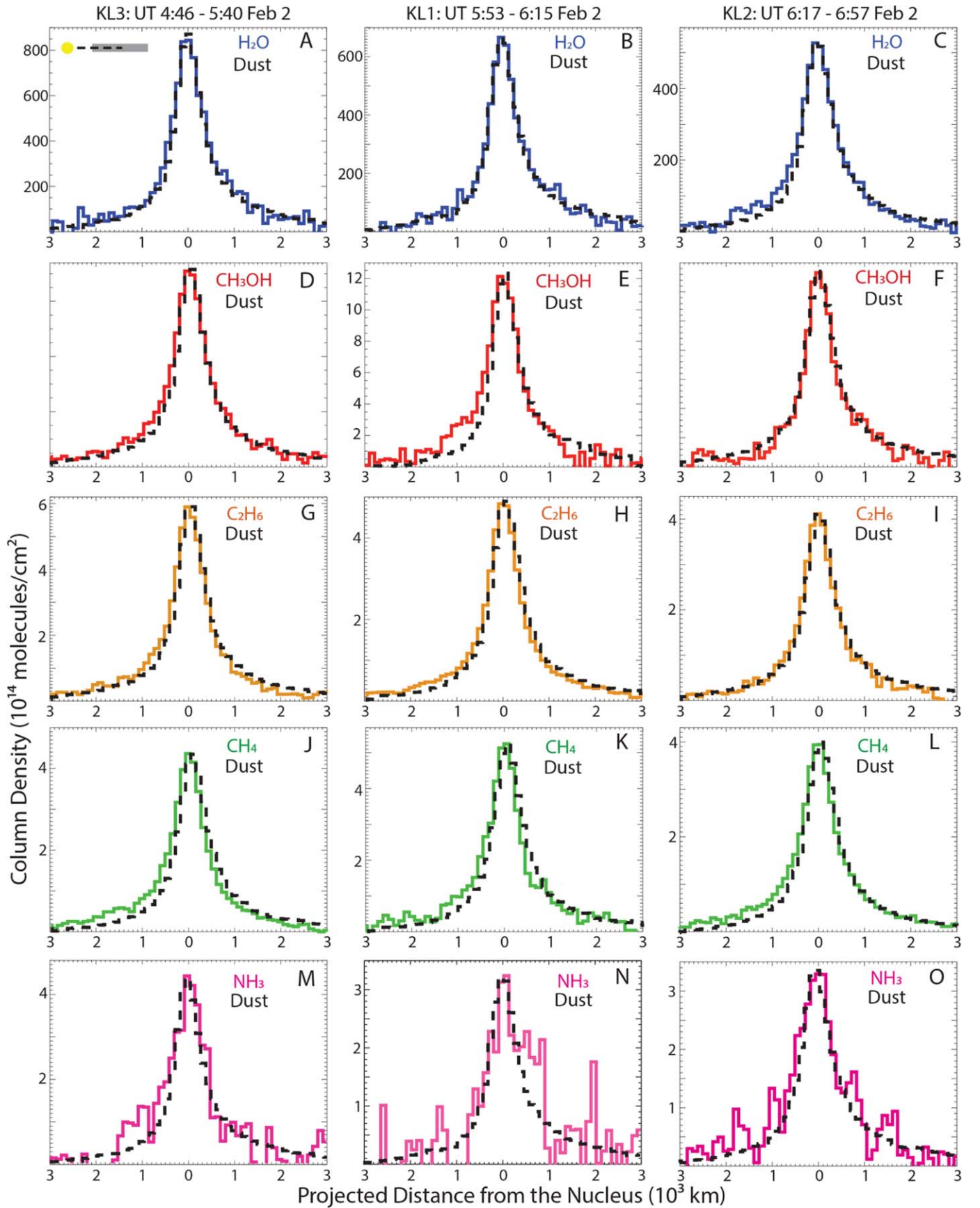
Figure 5. Spatial profiles for volatiles (a–c) H_2O, (d–f) CH_3OH, (g–i) C_2H_6, (j–l) CH_4, (m–o) NH_3, and co-measured dust along the slit at different times (settings, as indicated atop each column) on February 2 in C/2014 Q2 (Lovejoy). Volatile gas column densities (solid colored traces) are compared with simultaneously obtained dust column densities (dashed black traces) scaled to the peak of the gas. The position of the slit with respect to the Sun is given in panel (a). For all panels in Figures 5–7, the sunward-facing hemisphere is to the left.
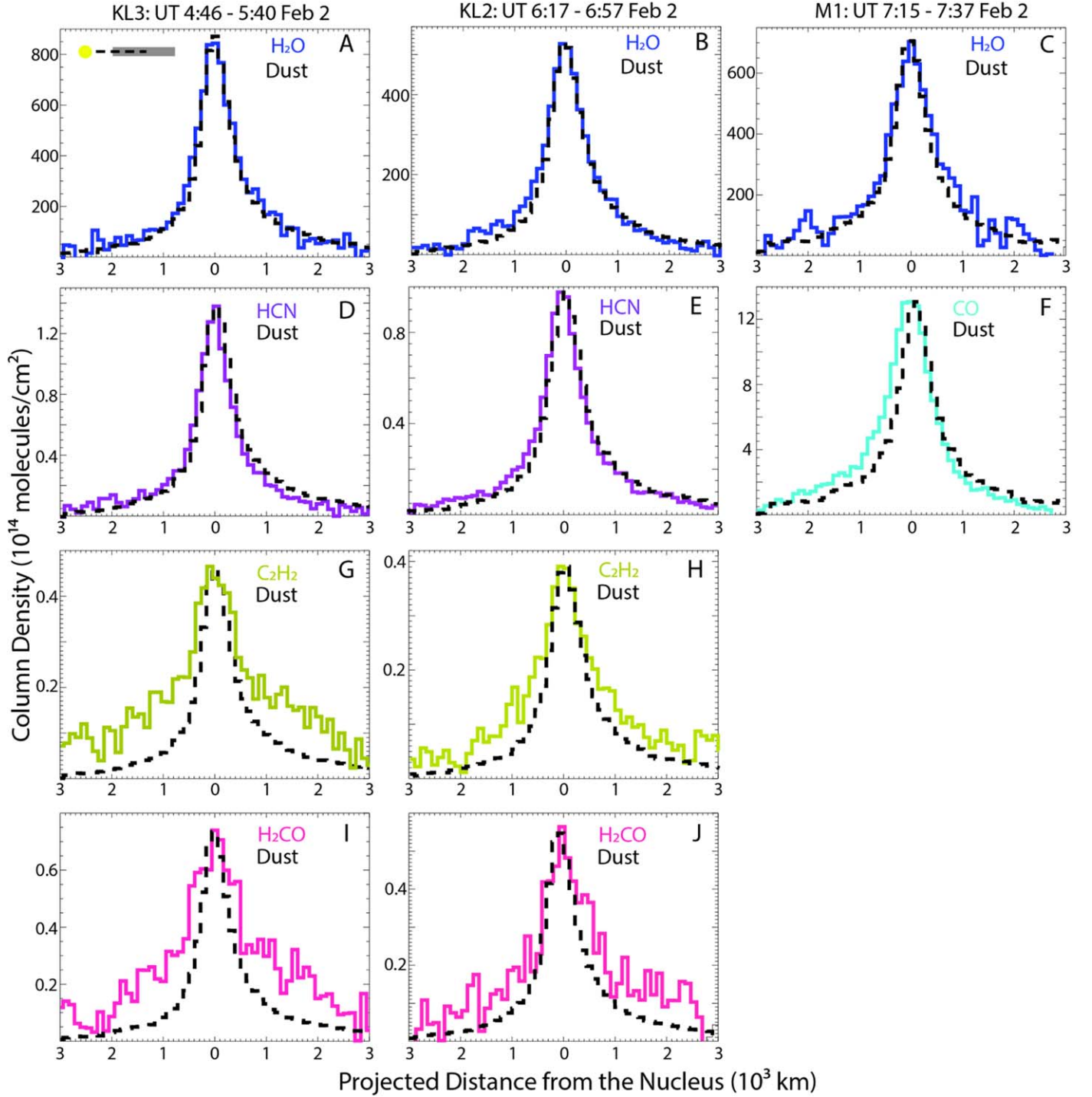
Figure 6. Similar to Figure 5, but for volatiles (a–c) H_2O, (d–e) HCN, (f) CO, (g–h) C_2H_2, (i–j) H_2CO, and co-measured dust along the slit at different times (settings) on February 2.

4.2. Water (H_2O)

H_2O is the most abundant cometary volatile and was the only molecule that was detected in all seven settings, providing a basis to which abundances of other volatiles can be compared without concern for temporal variability. The large number of H_2O emissions detected within each setting (Tables 1, A1–A7; Figures 2(b), 4(b), A1(a), A2) allowed seven independent measures of T_{rot} over the two dates (Table 2). Derived values are in the range of $T_{rot} \sim 80$–100 K, with some small but significant differences between settings (Table 2). The derived

H_2O rotational temperatures are consistent with values obtained close in time and within a similar aperture size by the GIANO TNG using both slope and correlation analyses ($T_{rot} = 90 \pm 20$ K and 71 ± 20 K, respectively; Faggi et al. 2016) and values derived from NIRSPEC observations on February 4 ($T_{rot} = 78 \pm 1$ K; Paganini et al. 2017).

H_2O production rates show evidence for modest variability between settings, within a time frame that is short compared with the ~ 18 hr rotation period of the comet (Serra-Ricart & Licandro 2015). Short-term variability in H_2O production rates
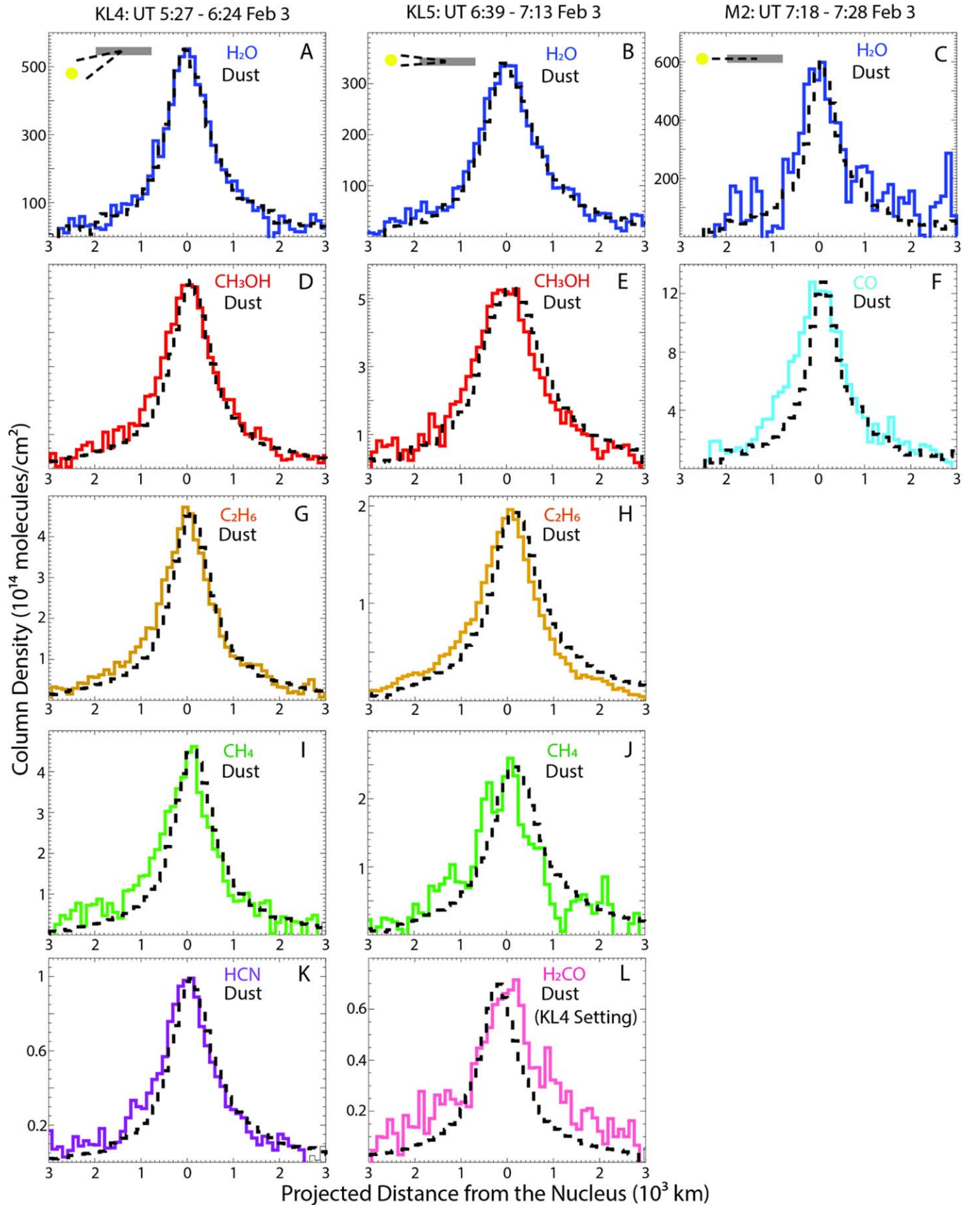
Figure 7. Similar to Figure 5, but for volatiles (a–c) H_2O, (d–e) CH_3OH, (f) CO, (g–h) C_2H_6, (i–j) CH_4, (k) HCN, (l) H_2CO, and co-measured dust along the slit at different times (settings) on February 3 in C/2014 Q2 (Lovejoy). In the left two columns, the slit was in rotator mode, so the position angle with respect to the Sun varied in the clockwise direction with time. In the right column, the slit was in stationary mode and the Sun position remained fixed relative to the slit.

Table 4
Characteristics of Volatile Spatial Profiles Averaged by Date

Molecule	Date	Multiplicative Growth Factor[a]	Differences (Volatile − Dust)		Sunward/Antisunward[d]
			HWHM (pixels)[b]	Peak Position (pixels)[c]	
H_2O	FEB 2	1.58 ± 0.02	0.33 ± 0.07	0.10 ± 0.06	0.91 ± 0.03
	FEB 3	2.19 ± 0.09	0.19 ± 0.11	-0.02 ± 0.16	0.97 ± 0.02
CO	FEB 2	1.65 ± 0.04	0.51 ± 0.13	1.10 ± 0.11	1.22 ± 0.03
	FEB 3	2.17 ± 0.06	1.39 ± 0.26	1.06 ± 0.22	0.96 ± 0.07
CH_3OH	FEB 2	1.54 ± 0.02	0.05 ± 0.15	0.45 ± 0.06	0.94 ± 0.05
	FEB 3	2.54 ± 0.10	0.43 ± 0.21	0.70 ± 0.29	1.03 ± 0.02
C_2H_6	FEB 2	1.56 ± 0.02	0.09 ± 0.07	0.47 ± 0.06	0.99 ± 0.04
	FEB 3	2.25 ± 0.10	0.18 ± 0.13	1.02 ± 0.25	1.10 ± 0.03
CH_4	FEB 2	1.55 ± 0.05	0.04 ± 0.07	0.65 ± 0.06	1.04 ± 0.03
	FEB 3	2.22 ± 0.10	0.40 ± 0.20	1.20 ± 0.16	1.22 ± 0.04
HCN	FEB 2	1.54 ± 0.02	-0.02 ± 0.08	0.56 ± 0.08	0.96 ± 0.03
	FEB 3	2.17 ± 0.06	0.34 ± 0.22	1.12 ± 0.18	1.05 ± 0.05
C_2H_2	FEB 2	3.01 ± 0.27	0.81 ± 0.19	0.33 ± 0.16	0.89 ± 0.04
NH_3	FEB 2	1.93 ± 0.14	0.53 ± 0.28	-0.15 ± 0.21	1.00 ± 0.08
H_2CO	FEB 2	4.06 ± 0.07	1.26 ± 0.26	-0.19 ± 0.20	0.84 ± 0.05
	FEB 3	4.61 ± 0.14	0.49 ± 0.37	-1.41 ± 0.31	1.04 ± 0.07
OH 1→0	FEB 2		1.26 ± 0.06	-0.66 ± 0.05	0.91 ± 0.01
	FEB 3		1.32 ± 0.13	-0.60 ± 0.10	0.91 ± 0.03
OH 2→1	FEB 2		1.10 ± 0.16	-0.59 ± 0.10	0.96 ± 0.02
	FEB 3		1.14 ± 0.36	-0.43 ± 0.18	0.91 ± 0.10
OH 3→2	FEB 2		2.09 ± 0.60	-0.57 ± 0.49	0.76 ± 0.19
NH_2	FEB 2		1.78 ± 0.65	-0.44 ± 0.17	0.95 ± 0.04
	FEB 3		2.28 ± 0.60	-0.43 ± 0.46	1.01 ± 0.12

Notes.
[a] Average multiplicative growth factors calculated independently for each parent molecule from all measurements obtained on that date (see Table A8 for individual measurements within a date).
[b] The average difference in the spatial profile half-width at half-maximum between the volatile emission and co-measured dust in pixels (1 pixel represents a projected distance at the comet of $\sim$110 km in the spatial direction) from all measurements obtained on that date (see Table A8 for individual measurements within a date). Positive values represent a broader volatile profile compared with the dust, whereas negative values indicate a narrower profile.
[c] The average difference between the spatial profile peak position between the volatile emission and the co-measured dust from all measurements obtained on that date (see Table A8 for individual measurements within a date). Positive values represent a sunward volatile shift, negative values an antisunward volatile shift.
[d] The average symmetry of the spatial profile as measured by the ratio of sunward to antisunward flux along the slit, excluding the central 5 pixels around the peak flux position from all measurements obtained on that date (see Table A8 for individual measurements within a date).

for C/2014 Q2 (Lovejoy) was also reported in observations by the Odin submillimeter space observatory (Biver et al. 2016). Values derived here are in the range of $\sim(5–8) \times 10^{29}$ molecules s^{-1} (Table 2), which are in good agreement, accounting for uncertainties and variability, with production rates determined around this time period by multiple techniques (Biver et al. 2015, 2016; Faggi et al. 2016; Paganini et al. 2017; Combi et al. 2018; Feldman et al. 2018). At these large production rates, some H_2O lines in the M-band setting could be subject to optical depth effects within $\sim$100 km of the nucleus (Dello Russo et al. 2000); however, there is no evidence of this when comparing the multiplicative growth factors and spatial profiles of measured H_2O lines in the M-band and KL settings.

A sufficient number of H_2O emissions from each nuclear spin species were detected to enable the independent determination of OPRs within each of the seven grating settings with the following values: KL3 (3.17 ± 0.26), KL1 (2.79 ± 0.19), KL2 (3.17 ± 0.29), M1 (3.08 ± 0.66), KL4 (3.36 ± 0.89), KL5 (2.81 ± 0.27), and M2 (3.10 ± 0.74). These values are in agreement with each other, and their weighted average gives OPR $= 2.96 \pm 0.12$, consistent with the high-temperature statistical equilibrium value (OPR $= 3$) and a nuclear spin temperature $T_{spin} \geqslant 39$ K. An OPR was determined for H_2O close in time to these observations by the

GIANO TNG and is in agreement, but poorly constrained (Faggi et al. 2016). An OPR for H_2O^+ was also derived for observations obtained about 3 weeks earlier and is also in agreement (OPR $= 2.77 \pm 0.24$, $T_{spin} > 24$ K; Shinnaka & Kawakita 2016).

Analyses for both dates show that the peak positions of the H_2O spatial profiles correspond closely to the peaks of the co-measured dust continuum profiles, and on average the H_2O profiles are slightly broader than the dust profiles (Figures 5(a)–(c), 6(a)–(c), 7(a)–(c), 8; Tables 4, A8). H_2O spatial profiles are generally slightly asymmetric with an antisunward enhancement, especially on February 2, that is similar to but less pronounced than the co-measured dust (Figures 5(a)–(c), 6(a)–(c), 7(a)–(c), A7; Tables 4, A8).

4.3. Carbon Monoxide (CO)

CO is the most volatile species detected in comets at IR wavelengths. CO lines were detected on both dates in settings M1 and M2 (Tables 1, A4, A7; Figures 4(b), A2(b)). Derived CO rotational temperatures are in the range of $T_{rot} \sim$ 60–70 K and agree within uncertainties on both dates (Table 2). A T_{rot} of 75 K was determined from Hubble Space Telescope Cosmic Origins Spectrograph (HST/COS) observations of the CO Fourth Positive system on 2015 February 2

(Feldman et al. 2018), in good agreement with the February 2 value derived here ($T_{rot} = 71 \pm 10$ K).

A slight increase in CO production rates from February 2 to February 3 is suggested, but abundances with respect to H_2O agree within uncertainties on both dates, with the weighted average abundance of $CO/H_2O = (2.16 \pm 0.20)\%$ (Tables 2 and 3). The CO production rate derived here on February 2 ($Q_{CO} = (1.42 \pm 0.19) \times 10^{28}$ molecules s^{-1}) is slightly lower than the production rate derived on the same date using HST/COS ($Q_{CO} = (2.23 \pm 0.27) \times 10^{28}$ molecules s^{-1}; Feldman et al. 2018). CO production rates and abundances relative to H_2O derived here are in good agreement with values determined from radio studies obtained a couple of weeks earlier (Biver et al. 2015; de Val-Borro et al. 2018).

At these CO production rates it is possible that optical depth effects could be important for the sampled lines within a few tens of kilometers from the nucleus (e.g., DiSanti et al. 2001; Bockelée-Morvan et al. 2010). Because the predicted affected region is smaller than the projected size of a NIRSPEC spatial pixel at the comet (~110 km), we do not expect derived rotational temperatures or production rates to be significantly affected by optical depth.

Analyses for both dates show that the peak positions of the CO spatial profiles are substantially broader and have large sunward offsets compared to the co-measured dust profiles (Figures 6(f), 7(f), 8; Tables 4, A8). The CO spatial profile on February 2 shows significant sunward asymmetry, much more pronounced than any other volatile; however, the CO profile on February 3 was symmetric in shape within uncertainties (Figures 6(f), 7(f), A7; Tables 4, A8).

4.4. Methanol (CH₃OH)

CH_3OH is the least volatile species after H_2O that is routinely detected in comets at IR wavelengths. Emission lines are ubiquitous between about 3.3 and 3.55 μm in the C/2014 Q2 (Lovejoy) spectra (Tables 1, A1, A2, A3, A5, A6; Figure 3). Rotational temperatures were derived in three settings (KL1, KL2, and KL5) with $T_{rot} \sim$ 70–80 K on these dates, with some small but significant differences between settings (Table 2). CH_3OH rotational temperatures derived here are in agreement with those determined for CH_3OH at radio wavelengths in mid- to late January (Biver et al. 2015).

Measurements are consistent with a marginally lower value of the CH_3OH production rate derived in setting KL2 on February 2 compared with values in other settings (Table 2). Abundances with respect to H_2O are a little more variable with a range of ~1.3%–1.9% (Table 2) and a weighted average abundance of $CH_3OH/H_2O = (1.76 \pm 0.08)\%$ (Table 3). CH_3OH production rates and abundances relative to H_2O determined here are slightly lower than values reported at radio wavelengths from measurements in mid- to late January (CH_3OH/H_2O = 2.2%–2.4%; Biver et al. 2015, 2016; de Val-Borro et al. 2018).

Analyses for both dates show that the peaks of the CH_3OH spatial profiles are slightly broader and offset toward the sunward direction compared with co-measured dust (Figures 5(d)–(f), 7(d)–(e), 8; Tables 4, A8). The CH_3OH spatial profile shapes are relatively symmetric on both dates (Figures 5(d)–(f), 7(d)–(e), A7; Tables 4, A8).

4.5. Formaldehyde (H₂CO)

H_2CO is commonly sampled in comets; however, its low abundance and only moderately strong emissions make it difficult to routinely detect at IR wavelengths. Many emission lines of H_2CO were detected in C/2014 Q2 (Lovejoy) (Tables 1, A1, A2, A3, A5, A6; Figure 4(a)). Rotational temperatures were determined in three settings (KL3, KL2, and KL4) for H_2CO, resulting in $T_{rot} \sim$ 100–120 K on these dates, with some small but significant differences between settings (Table 2).

H_2CO production rates are variable, with differences of more than a factor of two between settings measured close in time (Table 2). Abundances with respect to H_2O and C_2H_6 are in good agreement in four settings, with values significantly lower in setting KL5; however, abundances in KL5 are based on only three measured lines for H_2CO (Table 2). Based on measurements in five settings, the weighted average abundance of $H_2CO/H_2O = (0.29 \pm 0.03)\%$ (Table 3). H_2CO production rates and abundances relative to H_2O determined here are in good agreement with values reported at radio wavelengths from measurements in mid- to late January (Biver et al. 2015; de Val-Borro et al. 2018), although the relevance of this comparison is uncertain owing to different assumptions for parent versus product contributions when determining production rates.

Analyses of H_2CO spatial profiles show differences between February 2 and 3. The peak of the H_2CO spatial profile on February 2 corresponds closely *in position* to the peak of the co-measured dust continuum profile but is notably broader, especially in the profile wings (Figures 6(i)–(j), 8(a); Tables 4, A8). On February 3, the H_2CO spatial profile peak is only marginally broader than the co-measured dust but has a peak position offset in the antisunward direction compared to the dust (Figures 7(l), 8(b); Table 4). The H_2CO profile shape on February 2 shows a significant asymmetric enhancement in the antisunward direction; however, its shape on February 3 is symmetric within uncertainty (Figures 7(l), A7; Tables 4, A8). The broader and more asymmetric spatial profile and larger multiplicative growth factor compared with other species is evidence of an extended coma source for H_2CO.

4.6. Methane (CH₄)

CH_4 is the second most volatile species detected in the coma of comets at IR wavelengths after CO, and the most volatile hydrocarbon. Only a few CH_4 lines were detected on each date, but they are generally strong (Tables 1, A1, A2, A3, A5, A6; Figures 3, A1(b)). Rotational temperatures determined in three settings (KL3, KL1, and KL4) are in agreement within uncertainties with $T_{rot} \sim$ 90–110 K (Table 2).

CH_4 production rate measurements in three settings on February 2 are consistent; however, the production rate on February 3 in setting KL4 is marginally higher than that derived in setting KL5 (Table 2). Abundances with respect to H_2O are consistent in all settings, with a weighted average abundance $CH_4/H_2O = (0.75 \pm 0.03)\%$ (Table 3).

Analyses for both dates show that the peaks of the CH_4 spatial profiles are offset toward the sunward direction and are similarly broad to marginally broader compared to the co-measured dust spatial profiles (Figures 5(j)–(l), 7(i)–(j), 8; Tables 4, A8). CH_4 spatial profile shapes are relatively symmetric on February 2 but have a pronounced asymmetric
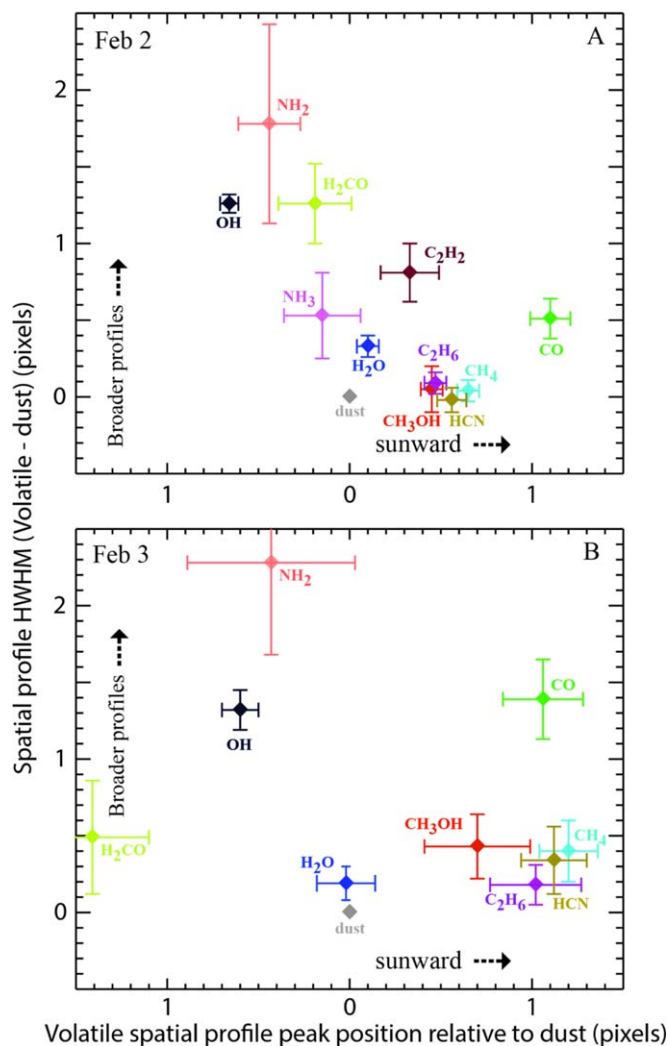
Figure 8. Peak position and width (half-width at half-maximum) of volatile spatial profiles compared with the co-measured dust for (a) February 2 and (b) February 3. Differences are measured in spatial pixels with 1 pixel ~ 110 km projected distance at the comet.

sunward enhancement on February 3 (Figures 5(j)–(l), 7(i)–(j), A7; Tables 4, A8).

4.7. Ethane (C_2H_6)

The strengths of the C_2H_6 emissions make it one of the easiest molecules to detect in comets at IR wavelengths, and multiple strong lines were detected in five settings in C/2014 Q2 (Lovejoy) (Tables 1, A1, A2, A3, A5, A6; Figure 3(a)). C_2H_6 rotational temperatures were determined on both dates in five settings (Table 2). On February 2, all three measurements were consistent with $T_{rot} \sim 90$ K within uncertainties. The two measurements on February 3 suggest that T_{rot} may be marginally higher in setting KL4 (113 ± 17 K) than the value obtained shortly after in setting KL5 (85^{+10}_{-11} K) (Table 2).

Measured C_2H_6 production rates show variability on short timescales by about a factor of two ($Q_{C2H6} \sim (3–6) \times 10^{27}$ molecules s^{-1}; Table 2). Abundances relative to H_2O are more consistent but still show some variability outside the range of uncertainties, with values between $\sim 0.6\%$ and 0.8% (Table 2), and a weighted average abundance $C_2H_6/H_2O = (0.68 \pm 0.03)\%$ (Table 3). Because C_2H_6 is detected in all the L-band

settings and is a nonpolar molecule that is generally not associated with H_2O in comets, it is useful to compare abundances of volatiles to both H_2O and C_2H_6. For each time-block, mixing ratios with respect to C_2H_6 are shown for all co-measured species in Table 2, with a weighted average for all settings given in Table 3.

Analyses for both dates show that the peaks of the C_2H_6 spatial profiles are offset toward the sunward direction and are similarly broad to marginally broader compared with the co-measured dust profiles (Figures 5(g)–(i), 7(g)–(h), 8; Tables 4, A8). C_2H_6 spatial profile shapes are symmetric on February 2 but have an asymmetric sunward enhancement on February 3, similar to CH_4 but not as pronounced (Figures 5(g)–(i), 7(g)–(h), A7; Tables 4, A8).

4.8. Acetylene (C_2H_2)

C_2H_2 is important for constraining hydrocarbon chemistry in comets, but its emissions are only moderately strong and blends with other species are an issue for some of the stronger lines. Because of this, C_2H_2 rotational temperatures and spatial profiles are rarely measured in comets; however, a sufficient number of lines were detected to perform a detailed analysis in C/2014 Q2 Lovejoy (Tables 1, A1, A3, A5; Figures 2, A2(a), A4(a)). $T_{rot} = 90^{+11}_{-9}$ K was determined in the KL2 setting (Table 2). In other settings, C_2H_2 rotational temperatures were assumed to be the same as co-measured CH_4 or C_2H_6 (Table 2). Based on the lines measured, the uncertainty from the assumed and measured T_{rot} does not significantly contribute (only $\sim 1\%$–4%) to the uncertainties in C_2H_2 production rates.

C_2H_2 production rates were determined in three settings (KL3, KL2, and KL4) and are significantly higher in the KL3 setting compared with the others (Table 2). C_2H_2 abundances relative to H_2O are variable, highest in KL3 and decreasing in subsequent settings, with a weighted average abundance $C_2H_2/H_2O = (0.11 \pm 0.02)\%$ (Table 3). C_2H_2/C_2H_6 is notably higher on February 2 compared with February 3 (Table 2), with the weighted average abundance $C_2H_2/C_2H_6 = 0.16 \pm 0.03$.

C_2H_2 spatial profiles could only be obtained on February 2 and show that the peak positions are slightly offset toward the sunward direction and are significantly broader compared with the co-measured dust continuum profiles, especially in the profile wings (Figures 6(g)–(h), 8; Tables 4, A8). The C_2H_2 spatial profile shape shows a significant asymmetric enhancement in the antisunward direction (Figures 6(g)–(h), A7; Tables 4, A8). The broader and more asymmetric spatial profile and larger multiplicative growth factors compared with other species are strong evidence of a substantial extended coma source.

4.9. Ethylene (C_2H_4)

Although C_2H_4 emissions are numerous in the ~ 3.2–$3.35\,\mu$m region, they are relatively weak, are located in many areas of generally low atmospheric transmittance, occur in some regions where weak unidentified emissions are present, and are subject to blends from stronger and more abundant species (Figure 9). For these reasons C_2H_4 has not been definitively detected in a comet from ground-based studies. C_2H_4 was detected in the coma of comet 67P/Churyumov-Gerasimenko from spectra obtained by the ROSINA (DMFS) instrument aboard the Rosetta spacecraft (Luspay-Kuti et al. 2015; Rubin et al. 2015; Altwegg et al. 2017); however,
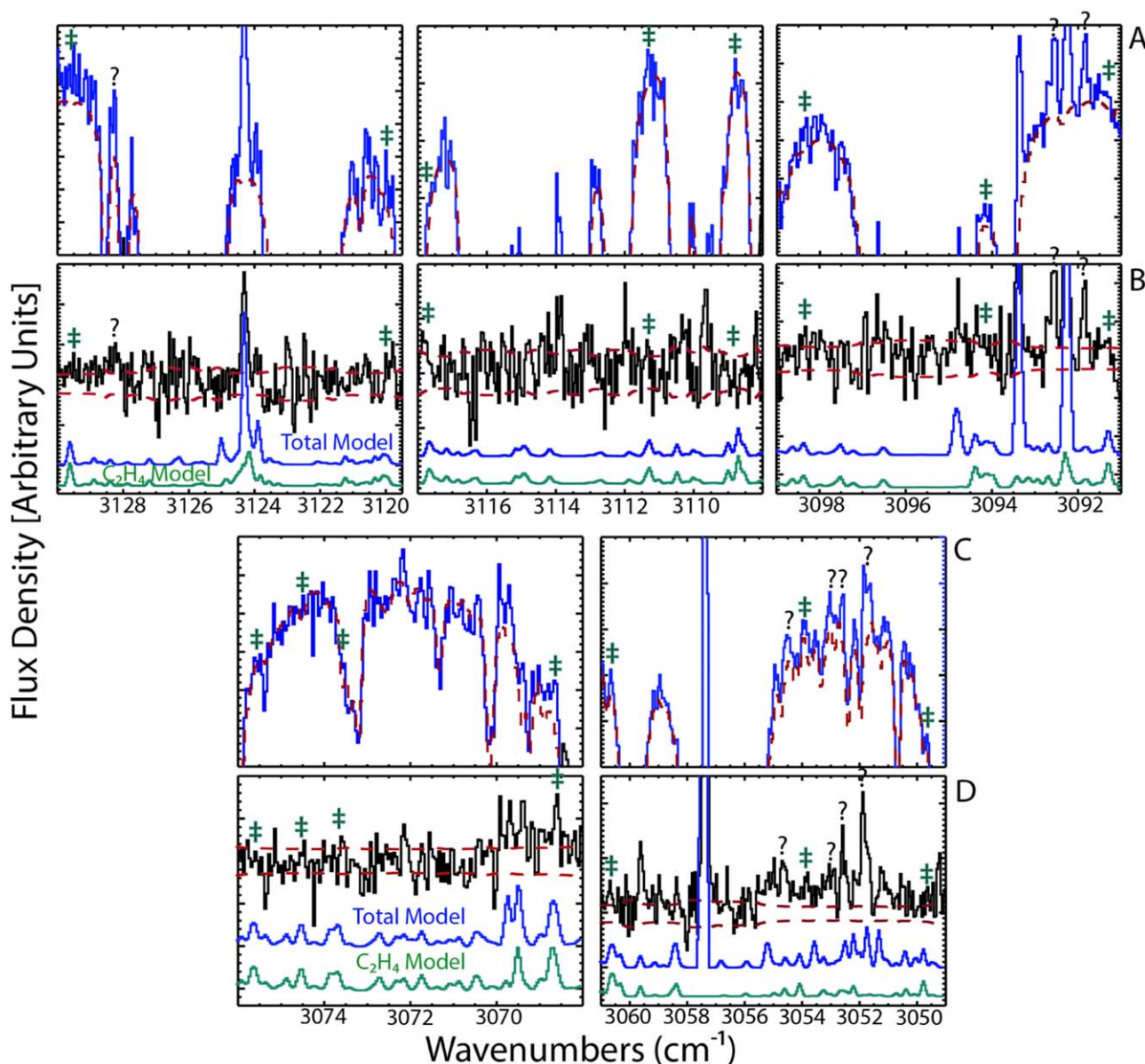
Figure 9. Flux-calibrated, high-resolution ($\lambda/\Delta\lambda \sim 25{,}000$) 3 spectral × 9 spatial pixel spectral extracts, residuals, and best-fit fluorescence models for C/2014 Q2 (Lovejoy) on February 2. (a) Spectral extracts zoomed in three regions within setting KL1 order 24 showing the eight C_2H_4 emissions used for the analysis (‡). Solid blue traces are the comet spectral extracts with best-fit synthetic atmospheric models superimposed (dashed red traces). Unidentified emissions (?) and regions of low atmospheric transmittance (areas of low flux density) are shown. (b) Spectral residuals (solid black traces on top of the panel) with the estimated $\pm 1\sigma$ channel-by-channel photon noise envelope superimposed (dashed red traces) covering the same spectral regions as panel (a) and showing the C_2H_4 emissions used in the analysis (‡), as well as unidentified emissions. Best-fit fluorescence models (total model with all contributing species in blue and the C_2H_4 model below that in turquoise) are also shown. (c) Spectral extracts zoomed in two regions within setting KL3 order 23 showing the seven C_2H_4 emissions used for the analysis (‡). All other information is the same as for panel (a). (d) Same as panel (b), but covering the same spectral regions as shown in panel (c). The 15 lines used in the February 2 analysis were chosen because they are in regions of relatively high atmospheric transmittance and are not blended with other known species. Line fluxes for the C_2H_4 emissions are given in Tables A1 and A2.

to date there is no well-constrained C_2H_4 production rate or mixing ratio relative to H_2O reported in 67P. C_2H_4 was also targeted in 1P/Halley by the Neutral Mass Spectrometer aboard the Giotto spacecraft (e.g., Eberhardt 1999); however, difficulties in separating a potential C_2H_4 contribution from other mass/charge = 28 species such as CO and N_2 make determining the presence and abundance of C_2H_4 in 1P/Halley uncertain (Geiss et al. 1991).

Here we report strong evidence for first ground-based detection of C_2H_4 in a comet based on line-by-line analysis of C_2H_4 emissions (Tables 1, A1, A2, A5; Figures 3, 9, A1(b)). Line fluxes at the frequencies of seven out of the nine strongest

predicted individual unblended C_2H_4 emissions (generally made up of multiple unresolved C_2H_4 lines) on February 2 have S/Ns >3, with fluxes consistent with the globally determined production rate (Tables 1, A1, A2; Figures 3, 9, A1(b)). On February 3, only four emissions of C_2H_4 were sampled (Tables 1, A5), so detection on that date is at best marginal, and although reported as a formal value in Table 2, it is more appropriately considered a 3σ upper limit (Q_{C2H4} $< 4.6 \times 10^{27}$ molecules s^{-1}).

Although S/Ns of individual emissions on February 2 are suggestive (Tables A1, A2), there is additional evidence for the detection of C_2H_4. Figure 9 shows the spectra, residuals, and
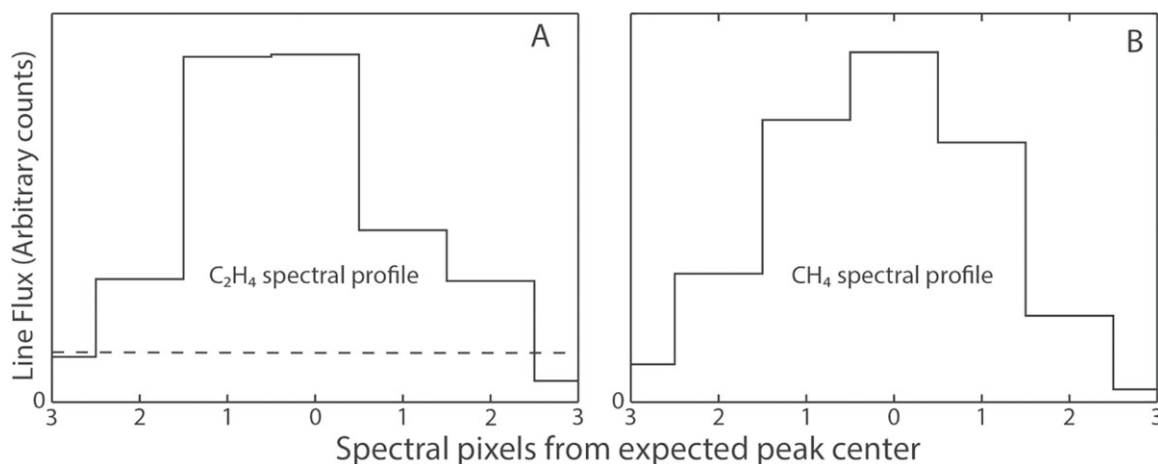
Figure 10. Spectral profiles of (a) C_2H_4 and (b) CH_4 showing the spectral line shapes for the strongest unblended lines within a setting. C_2H_4 is compared with CH_4 to show that the spectral line shape of C_2H_4 is consistent with the expected line shape of a clearly detected volatile species obtained within the same order and setting. The estimated 1σ uncertainty level (dashed line) is shown for the C_2H_4 profile.

associated fluorescence models where C_2H_4 emissions are present on February 2. While individual emissions of C_2H_4 in the spectra are only marginally visible at best (Figure 9), co-adding lines within individual settings (KL3 - 7 lines, KL1 – 8 lines, and KL4 – 4 lines) are consistent with detections at the 7.7σ, 6.8σ, and 4.0σ level, respectively (Table 1). However, this overestimates our confidence in the measurement, as in each case the uncertainty is dominated by the standard uncertainty of the mean between individual measurements and not the stochastic uncertainty based on the S/Ns of individual emissions. This is a reflection of the difficulty in quantifying weak emissions, which are more affected by blends (with known and possibly unknown species) and uncertainties in the local continuum baseline levels (Figure 9). Taking the standard uncertainty of the mean into account suggests detections at the confidence level of 3.5σ, 4.3σ, and 2.5σ for settings KL3, KL1, and KL4, respectively. Determining the standard uncertainty of the mean for emissions combining both the KL3 and KL1 settings gives a confidence level of 5.4σ, providing compelling evidence for a C_2H_4 detection on February 2. The 2.5σ confidence level from setting KL4 is consistent with a marginal detection at best on February 3.

A spectral profile of C_2H_4 was generated by summing the spectral residuals within 7 pixels (centered on the pixel at the expected frequency and ± 3 pixels on either side) of the strongest unblended lines (from setting KL1 order 24) based on fluorescence models. The resultant spectral profile of C_2H_4 lines from the KL1 setting shows the expected line shape of a real emission feature as illustrated by a comparison with a spectral profile of CH_4 obtained within the same order and setting (Figure 10). This provides further support for the detection of C_2H_4 on February 2.

Coincident blends with unknown species at multiple C_2H_4 line positions could also mimic a real molecular spectral profile, although this seems unlikely because the blends would have to dominate the profile and closely overlap C_2H_4 at multiple wavelengths. However, it is possible that emissions from unidentified species could add flux at measured C_2H_4 line positions based on the presence of a few such emissions in these spectral regions (Figure 9). Even if this is the case, blends from unidentified species would need to contribute significantly over multiple emissions to change the conclusions on C_2H_4

presented here. For example, removing the two highest-S/N C_2H_4 lines from this analysis (e.g., assuming that they were due to unknown species and not C_2H_4) would change the confidence level for the detection on February 2 from 5.4σ to 4.3σ and lower the derived production rate by 18%. Although multiple coincident blends of C_2H_4 lines from unidentified species cannot be completely ruled out, we conclude that a C_2H_4 detection on February 2 is compelling based on the totality of the evidence.

Rotational temperatures could not be determined for C_2H_4, so an assumed $T_{rot} = 100 \pm 10$ K was used in each setting, based on the available C_2H_4 fluorescence model. For the C_2H_4 lines measured in each setting, the uncertainty in the assumed T_{rot} is estimated to only affect measured production rates by $\sim 3\%$–7% and so is of minor importance compared with other sources of uncertainty. Derived production rates and abundances relative to H_2O agree within uncertainties for all three settings (Table 2), with a weighted average abundance C_2H_4/ $H_2O = (0.22 \pm 0.04)\%$ (Table 3). The low S/N of the lines did not allow a determination of a spatial profile for C_2H_4, so it is unclear whether the spatial distribution of C_2H_4 in the coma of 2014 Q2 (Lovejoy) is more similar to C_2H_6 (consistent with direct release from nucleus ice) or C_2H_2 (suggesting a significant contribution from an extended source). The relative abundances of C_2H_6, C_2H_4, and C_2H_2 may indicate the importance of hydrogen addition reactions in pre-cometary ices (e.g., Kobayashi et al. 2017). The weighted average abundance is $C_2H_4/C_2H_6 = 0.32 \pm 0.06$ (Table 3).

4.10. Ammonia (NH_3)

NH_3 is difficult to quantify at IR wavelengths because of its few unblended and relatively weak emission lines. This is also true in this case, as the few measured lines of NH_3 (Tables 1, A1, A2, A3, A5, A6; Figures 2, A1(a), A2(a), A3(b), A4(b)) do not allow an independent determination of T_{rot}. In the five settings in which NH_3 was detected, T_{rot} was assumed based on values derived for co-measured species (Table 2). Because few lines are detected, uncertainties in the assumed T_{rot} contribute significantly to uncertainties in derived production rates (7%–20% depending on the setting).

NH_3 production rates derived in five settings on both dates are formally consistent, though possible variability could be

masked within the large uncertainties (Table 2). The abundance of NH_3 relative to H_2O also shows apparent consistency within large uncertainties, with a weighted average abundance $NH_3/H_2O = (0.64 \pm 0.06)\%$ (Table 3). We assume a photodissociation rate at 1 au for $NH_3 = 1.8 \times 10^{-4}$ s^{-1} (Huebner et al. 1992; Huebner & Mukherjee 2015); however, if NH_3 has a significantly shorter lifetime corresponding to a photodissociation rate of 4.8×10^{-4} s^{-1} (Jackson 1976), that would increase our derived NH_3 production rates and relative abundances by ~9%.

NH_3 spatial profiles could only be obtained on February 2, and the peak position of the NH_3 spatial profile corresponds closely to the peak of co-measured dust continuum profile but is significantly broader (Figures 5(m)–(o), 8; Tables 4, A8). The NH_3 spatial profile shape is symmetric within uncertainties (Figures 5(m)–(o), A7; Tables 4, A8). We note that unlike C_2H_2 and H_2CO, the NH_3 profiles are broader closer to the profile peak but are not extended in the profile wings (e.g., compare Figure 5(n) with Figures 6(g)–(j) and 7(l)).

4.11. Hydrogen Cyanide (HCN)

HCN is routinely detected in comets at IR wavelengths through rovibrational lines within its strong ν_3 band at 3.02 μm. Strong emission lines were detected in C/2014 Q2 (Lovejoy) (Tables 1, A1, A3, A4; Figures 2, A1(a), A2(a), A4). Rotational temperatures were determined in three settings (KL3, KL2, and KL4), resulting in $T_{rot} \sim 80$–100 K, with some small but significant differences between settings (Table 2).

Measured HCN production rates are consistent with a slightly lower value in setting KL2 than in the other two settings (Table 2). Abundances with respect to H_2O are relatively consistent with values ranging from ~0.15% to 0.19% (Table 2) and a weighted average abundance of $HCN/H_2O = (0.18 \pm 0.01)\%$ (Table 3). HCN production rates and abundances relative to H_2O derived here are higher by about a factor of two compared with values obtained at radio wavelengths from measurements in mid- to late January (Biver et al. 2015; Wirström et al. 2016; de Val-Borro et al. 2018). This discrepancy of a factor of two between derived IR and radio abundances of HCN has been consistently seen in comets for unknown reasons.

Analyses for both dates show that the peaks of the HCN spatial profiles are offset toward the sunward direction and are similarly broad compared with the co-measured dust (Figures 6(d)–(e), 7(k), 8; Tables 4, A8). The HCN spatial profile shapes are relatively symmetric on both dates (Figures 6(d)–(e), 7(k), A7; Tables 4, A8).

4.12. Cyanoacetylene (HC₃N)

HC_3N has not been detected at IR wavelengths in comets. Although HC_3N has intrinsically strong emissions near 3.0 μm, its abundance in comets is low and many of its IR emissions are blended with much higher intensity emissions of other molecular species (Figures 2(b), A3(a), A4(b)). Based on the brightness of C/2014 Q2 (Lovejoy), we can significantly constrain the abundance of HC_3N in setting KL3 by targeting five unblended lines (Table 1, Figure A3(a)). A line-by-line analysis for the positions of these five unblended HC_3N emissions is consistent with $Q_{HC3N} < 2.7 \times 10^{25}$ molecules s^{-1} (3σ). This gives an abundance $HC_3N/H_2O \leqslant 0.0043\%$ and $HC_3N/HCN \leqslant 2.3\%$ (3σ). This upper limit is in agreement with a detection of HC_3N obtained from radio observations in mid- to late January ($HC_3N/H_2O = 0.002\%$; Biver et al. 2015). We also note that this upper limit suggests that HC_3N is depleted in C/2014 Q2 (Lovejoy), as it is at the low end of the range of values derived in the few comets where HC_3N has been detected at radio wavelengths (Bockelée-Morvan & Biver 2017).

4.13. Hydroxyl Radical (OH)

Many OH lines are present throughout the sampled L-band region of the comet spectra, almost all of which are dominated by prompt emission, which is a well-known tracer of H_2O production (e.g., Bonev et al. 2006). Analyses for both dates show that the peaks of the OH spatial profiles are offset toward the antisunward direction and are broader compared with the corresponding dust continuum profiles (Figures A6, 8; Tables 4, A8). The OH spatial profile shapes are asymmetric, with enhancement in the antisunward direction on both dates (Figures A6, A7; Tables 4, A8). The properties of OH spatial profiles are consistent for all measured OH lines, independent of rotational energy state (higher-J OH $1 \rightarrow 0$ rovibrational lines are in orders 21–24, lower-J lines are in orders 25–27; see Table 4), and for lines within the three measured vibrational bands $1 \rightarrow 0$, $2 \rightarrow 1$, and $3 \rightarrow 2$ (Tables 4, A1, A2, A3, A5, A6, A8). A more detailed study on the spatial distribution of OH lines and their relationship to H_2O is planned for a future publication.

4.14. Amino Radical (NH₂)

NH_2 is a photodissociation product of the parent volatile NH_3 and is routinely detected at IR wavelengths. Based on the relative intensities and the energy levels of detected NH_2 lines at IR wavelengths, they likely have a sizable contribution from fluorescence emission with possibly little contribution from prompt emission (unlike what is seen for OH). NH_2 production rates are not derived for this work, but the spatial distributions of NH_2 along the slit were analyzed (Figure A6). Analyses for both dates show that the peaks of the NH_2 spatial profiles are slightly offset toward the antisunward direction and are much broader compared with the corresponding dust continuum profiles (Figures A6, 8; Tables 4, A8). The NH_2 spatial profile shapes are symmetric on both dates within uncertainties (Figures A6, A7; Tables 4, A8). The broad and flat NH_2 spatial profiles are the signature of a species released primarily in the coma as an extended source. A more detailed analysis of the relationship between the spatial distributions of NH_2 and its volatile parent NH_3 in C/2014 Q2 Lovejoy using the methodology of Kawakita & Mumma (2011) is planned for a future publication.

4.15. Unidentified Emissions

There are a number of detected emissions in C/2014 Q2 Lovejoy that are unidentified, which is typical for bright comets studied to date at IR wavelengths (e.g., Dello Russo et al. 2006, 2013). Although many of these unidentified emissions are coincident in position with lines from identified species, the measured line fluxes are many times stronger than predicted, or other lines from that particular species should also be detected but are not seen. For the 16 strongest unidentified emissions, spatial profile properties were determined on February 2 (Table A9; Figure A7). The peaks of most of these unidentified spatial profiles are offset in the

antisunward direction and are notably broader compared with the co-measured dust continuum profiles (Figure A7).

5. Discussion and Interpretation

5.1. Rotational Temperatures

Measured rotational temperatures are generally consistent with each other with a few exceptions: (1) C_2H_6, CH_4, HCN, and C_2H_2 values are consistent with each other and co-measured H_2O with the exception of HCN during the first time-block (setting KL3) on February 2 (Table 2). (2) CH_3OH and CO values are slightly lower than those derived for co-measured H_2O (Table 2). (3) H_2CO values are slightly higher than those derived for co-measured H_2O (Table 2). (4) Rotational temperatures for all species during the first time-block on February 3 (setting KL4) are systematically higher than values derived for these species at other times (Table 2). (5) Measurements show that the second time-block on February 3 (setting KL5) has on average the lowest values, suggesting a decrease in gas T_{rot} of $\sim$20 K within a time span of approximately 1 hr (Table 2). This apparent change in gas T_{rot} is also accompanied by a significant decrease in gas production over this time, suggesting variability in both gas production and coma dynamics on a timescale significantly shorter than the rotation period of the comet (Serra-Ricart & Licandro 2015; Biver et al. 2016). Because neutral−neutral and possibly neutral−electron collisions in the coma tend to control and warm the local gas temperature, it is not surprising that a significant decrease in gas production rate (and the rate of these collisions) is accompanied by a decrease in measured gas rotational temperature. The reason for small differences in T_{rot} between species is less clear but could be related to how they are released into the coma.

5.2. H_2O OPRs

H_2O is organized into two distinct nuclear spin species, when the nuclear spin vectors of the hydrogen atoms are parallel (ortho) or antiparallel (para). The ratio of ortho-to-para species (OPR) achieves a statistical equilibrium value of 3 for temperatures above $\sim$50 K, whereas the para species is increasingly favored as the temperature decreases below 50 K. The significance of cometary OPRs is unclear (e.g., Bonev et al. 2007, 2013; Faure et al. 2019). There is some evidence that once OPRs are locked into H_2O ice upon its formation, conversion is difficult (e.g., Miani & Tennyson 2004), so it is possible that OPRs have remained stable since ices were incorporated into the nucleus and represent the chemical formation temperature of cometary H_2O (e.g., Kawakita et al. 2005). Other laboratory results suggest that OPRs are not ancient but instead are reset to their high-temperature equilibrium value after sublimation, independent of formation processes (Hama et al. 2018).

The OPR for H_2O derived here for C/2014 Q2 (Lovejoy) is consistent with the high-temperature limit (OPR = 2.96±0.12) and $T_{spin} \geqslant 39$ K. OPRs have been determined in many comets and show variability. Some values in comets are consistent with the high-temperature limit (OPR = 3), and others with OPR values significantly less than 3 (e.g., Faure et al. 2019), suggesting that sublimation does not immediately reset values to the high-temperature limit. To what extent the range in measured OPRs in comets relates to differences in the formation temperatures of ices in the solar nebula or sublimation and coma processes remains an open question.

5.3. Production Rates and Relative Abundances

As with the rotational temperature measurements, derived production rates and relative abundances show no dramatic changes over these two dates, yet there is small but significant short-term variability. There is evidence of differences in absolute gas production rates of $\sim$40% between settings obtained consecutively ($\sim$1 hr apart on average) on both dates (Table 2). Some statistically significant differences are seen in the relative abundances of species measured throughout these two dates, though these variations are small compared with the compositional diversity between comets seen within the population (Table 2; e.g., Dello Russo et al. 2016a; Lippi et al. 2021). Abundances relative to H_2O for all measured species are within the typical range measured in the comet population (Table 3). The only measured mixing ratio that was outside of what is considered typical in the comet population was CH_3OH/H_2CO, which is below its "typical" range (Table 3). C/2014 Q2 (Lovejoy) is most chemically similar to comets C/2007 N3 (Lulin) and C/2004 Q2 (Machholz) among the studied comet population, which classifies it into Group B5 (generally typical composition) within the IR comet taxonomy of Dello Russo et al. (2016).

Owing to the detection of C_2H_4, we have a more complete view of the hydrocarbon chemistry in this comet than in others, with $CH_4:C_2H_6:C_2H_4:C_2H_2 \sim$ 1:1:0.3:0.15. $CH_4/C_2H_6 \sim 1$ is typical for many comets within the population where these species are sampled (e.g., Dello Russo et al. 2016a; Lippi et al. 2021). Because C_2H_2 and C_2H_4 can be hydrogenated on the surfaces of grains at low temperatures (e.g., Kobayashi et al. 2017), the ratios of $C_2H_6:C_2H_4:C_2H_2$ may provide a measure of the efficiency of this process. In the case of C/2014 Q2 (Lovejoy), mixing ratios ($C_2H_6:C_2H_4:C_2H_2 \sim$ 70%:20%:10%) are consistent with efficient hydrogen atom addition reactions in pre-cometary ices. However, laboratory studies by Hiraoka et al. (2000) reported that the ratio of hydrogenation rate constants for C_2H_4/C_2H_2 is $\sim$6 × 10^3 in very low temperature ices, suggesting that there should be no detectable C_2H_4 in comets if this is the dominant process for setting hydrocarbon abundances. More recent laboratory studies by Kobayshi et al. (2017) report a much smaller ratio of hydrogenation rate constants ($C_2H_4/C_2H_2 \sim 3$), which is more favorable for preservation of C_2H_4 but still suggests C_2H_4 abundances significantly less than C_2H_2 and C_2H_6 in comets. This may indicate that ice abundances in C/2014 Q2 (Lovejoy) were not predominantly determined by hydrogen atom addition reactions, or if so, they occurred at higher temperatures where hydrogenation reaction rates are slower. Based on measurements of just C_2H_6 and C_2H_2 in other comets, this high value of C_2H_6/C_2H_2 is typical of the majority of the population (Dello Russo et al. 2016a; Lippi et al. 2021).

5.3.1. Parent−Product Relationships

Production rates derived for C_2 (7.8$^{+3.2}/_{-2.3}$ × 10^{26} molecules s^{-1}) and CN (7.4$^{+3.6}/_{-2.4}$ × 10^{26} molecules s^{-1}) in late January of 2015 (Venkataramani et al. 2016) are similar to production rates determined here about 1 week later for C_2H_2 and HCN. This suggests that the primary sources of C_2 and CN in C/2014 Q2 (Lovejoy) during this time were C_2H_2 and HCN, respectively.

5.4. Spatial Distributions of Volatiles in the Coma

C/2014 Q2 (Lovejoy) was sufficiently bright on these dates to perform an unusually detailed analysis of the spatial distributions of volatiles in the coma. The spatial profiles of parent volatiles obtained in all settings and on both dates are shown in Figures 5–7. The high S/Ns of these spatial profiles generated from multiple emissions, and in most cases multiple measurements within a given date, allow the accurate evaluation and comparison of the multiplicative growth factors, peak positions, widths (half-width at half-maximum), and sunward/antisunward asymmetry of these volatile spatial profiles and the co-measured dust continuum (Tables 4, A8). For comparison of volatiles within the same setting (or on the same date if conditions are stable, as is the case on February 2, but not February 3), larger multiplicative growth factors and broader spatial profile widths may indicate the presence of extended coma sources (Tables 4, A8). Additionally, volatiles released predominantly by direct ice sublimation due to surface illumination may tend to show sunward enhancements in spatial profiles, whereas the dust continuum and spatial profiles influenced by extended grain sources may show antisunward enhancements due to the effects of solar radiation pressure. By measuring spatial profiles for many species simultaneously, the importance of these factors can be estimated and compared with potential systematic effects on volatile spatial profiles such as asymmetries in sunward/antisunward outflow velocities. A graphical illustration of these results on both dates suggests possible release mechanisms, associations, and distinctions between these measured volatiles that may provide clues as to how these ices are stored and whether some molecules have sources in addition to direct ice sublimation in the nucleus of C/2014 Q2 (Lovejoy) (Figures 8, A7). The properties of spatial profiles for individual molecules are compared and contrasted below.

1. CH_3OH, HCN, C_2H_6, and CH_4 show similar spatial profile properties: (i) profiles peaked in the sunward direction relative to the dust profiles, (ii) similarly broad to marginally broader profiles than the co-measured dust profiles (Figures 5(d)–(l), 6(d)–(e), 7(d)–(e), 7(g)–(k), 8), and (iii) relatively symmetric or slightly sunward-enhanced profile shapes (Figure A7). Additionally, all these species have similar multiplicative growth factors within a setting (Table A8). All of this is consistent with direct sublimation of these volatiles from ices that are associated with each other in the nucleus as the dominant coma source of these species, with no evidence of extended source contributions.

2. H_2O spatial profiles are peaked in about the same position as the dust (Figures 5(a)–(c), 6(a)–(c), 7(a)–(c), 8) and have profile shapes that tend to be slightly asymmetric with enhancement in the antisunward direction (Figure A7). H_2O spatial profiles are shifted in peak position on both dates and moderately broader on February 2 compared with CH_3OH, HCN, C_2H_6, and CH_4—species likely released from associated nucleus ices (Figure 8). Two possible explanations are consistent with the shapes of the H_2O profiles: (i) the dominant source of H_2O is direct sublimation from nucleus ices that are not associated with the ices of other measured volatiles, or (ii) H_2O is associated with other volatiles predominantly released directly from ices in the nucleus (CH_3OH, HCN,

C_2H_6, and CH_4), but H_2O profile shapes and antisunward asymmetry are influenced by an additional source of icy grain sublimation in the coma that shifts the H_2O profile peak in the antisunward direction. The shapes of spatial profiles due to OH prompt emission (see #7 below) suggest that explanation (ii) is more likely.

3. The spatial distributions of C_2H_2 and H_2CO show notably broader profiles and multiplicative growth factors compared to other volatiles and co-measured dust (Figure 8; Tables 4, A8). In addition, C_2H_2 and H_2CO profiles show enhanced flux in both directions compared to co-measured dust, especially in the far wings of the profiles (Figures 6(g)–(j), 7(l)). This suggests substantial contributions from extended coma sources for both species. Although C_2H_2 and H_2CO both show clear evidence for extended coma sources, they have distinct spatial properties. C_2H_2 shows a sunward peak position compared with the dust, similar to C_2H_6, CH_4, CH_3OH, and HCN, whereas the H_2CO peak position is similar to the dust peak on February 2, but with a notable antisunward peak position on February 3 (Figure 8). Also, multiplicative growth factors for H_2CO are significantly larger than for C_2H_2. Production rates reported here for C_2H_2 and H_2CO should be considered upper limits for their nucleus sources and lower limits on their total (nucleus + coma) source contributions.

4. The source of NH_3 is more ambiguous, as its profile is broader closer to the profile peak but is not extended in the wings farther from the nucleus, as indicated by its smaller multiplicative growth factor compared with C_2H_2 and H_2CO. This is consistent with the primary source of NH_3 being direct sublimation from nucleus ice, but with an additional contribution due to an extended coma source from a short-lived parent.

5. The spatial distribution of CO is distinct compared with other volatiles. The CO profile peak position has a large shift toward the sunward direction and is also notably broader than the dust (Figures 6(f), 7(f), 8). Although the broad CO profiles are consistent with contributions from an extended source, there is no extension of the profile in the antisunward direction or in the profile wings, unlike the profiles of C_2H_2 and H_2CO, where there is clear evidence of extended sources (Figures 6(f)–(j), 7(f), (l)). Alternatively, the CO spatial profile could be explained by a nucleus ice source that is not associated with other measured volatiles (consistent with its multiplicative growth factor), with the broad sunward extended profile consistent with CO-rich jets. The clear sunward asymmetry of the CO spatial profile on February 2 compared with its symmetric CO profile shape on February 3 could be explained by the projection of CO-rich jets rotating in and out of the slit on these dates (Figures 6(f)–(j), 7(f), (l), 8, A7). Although expected to be minor at these production rates, we do not rule out optical depth effects within the central pixel causing slight broadening of the CO profiles.

6. As a product species, it is not surprising that the NH_2 profiles are significantly broader than co-measured dust and parent volatile profiles. On both dates the peaks of NH_2 profiles are also offset in the antisunward direction compared with co-measured dust (Figure 8). NH_3 is expected to be the main volatile source of NH_2; however,

no obvious association between NH_3 and NH_2 is revealed by this analysis.

7. The OH lines detected in these spectra are predominantly due to prompt emission, and as such their spatial profiles should directly trace that of H_2O, its primary parent. The shapes of both H_2O and OH spatial profiles show a slight asymmetry in the antisunward direction, which is consistent with this expectation (Figure A7); however, the OH spatial profiles are significantly broader with peaks shifted more antisunward compared to H_2O (Figure 8). Given the high production rate of H_2O, the broader OH spatial profiles are expected, as OH lines are subject to optical depth effects in the solar ultraviolet (Bonev 2005). The reason for the differences in peak positions between H_2O and OH spatial profiles could be an indication that icy grains are a major source of H_2O in the coma and the OH spatial profiles more closely track this extended source component.

8. The are many unidentified emissions within the C/2014 Q2 (Lovejoy) spectra. One method for revealing information about the source species of the strongest unidentified emissions is to compare their spatial profile properties to those of known species (Dello Russo et al. 2013). Spatial profiles for the 16 strongest unidentified emissions were determined (Table A9; Figure A7). Thirteen out of these 16 spatial profiles have a peak position that is in the antisunward direction compared with the co-measured dust profile. Twelve out of these 16 spatial profiles are also significantly broader than both the dust and parent volatiles (H_2O, CH_3OH, HCN, C_2H_6, and CH_4). For most unidentified profiles there is a closer association in spatial distributions to parents with likely extended source contributions (e.g., H_2CO) or product species (e.g., NH_2), and no associations with the parent volatiles dominated by direct sublimation of nucleus ices (e.g., H_2O, CH_3OH, HCN, C_2H_6, CH_4, and CO). This suggests that the molecular sources of most of the strongest unidentified emissions are product species released in the coma. We note that many of these unidentified emissions have also been seen in other comets (Table A9).

This study of volatile spatial distributions reveals notable differences in potential sources and/or nucleus associations for C_2H_2, H_2CO, and NH_3 compared with other measured species. Testing whether these spatial properties are more universal in comets is difficult because detecting emission lines of sufficient strength and number to get spatial profiles of adequate quality is rare; however, there are a few relevant examples. In C/2012 S1 (ISON), NH_3 and C_2H_2 showed some enhancement of spatial profiles in the antisunward direction relative to other measured volatiles that were consistent with contributions from extended sources (DiSanti et al. 2016; Dello Russo et al. 2016b). Spatial profiles of C_2H_2 in JFCs 103P/Hartley 2 and 46P/Wirtanen showed no evidence of an extended source contribution, but S/Ns were marginal especially in the profile wings (Dello Russo et al. 2011; Kawakita et al. 2013; Bonev et al. 2021). IR spatial profiles of H_2CO in C/2002 T7 (LINEAR) and C/2012 S1 (ISON) showed no evidence for extended sources (DiSanti et al. 2006, 2016; Dello Russo et al. 2016b); however, there is extensive evidence of H_2CO extended sources in comets from Giotto measurements of 1P/

Halley and studies at radio wavelengths (e.g., Cottin & Fray 2008; Cordiner et al. 2014).

There is also evidence from global molecular associations within the comet population and examples of elevated production rates relative to other volatile species at closer heliocentric distances that indicate that extended sources of C_2H_2, H_2CO, and NH_3 in comets may be common (Dello Russo et al. 2016a). What are candidate precursor species for C_2H_2, H_2CO, and NH_3 in comets? Polymers have long been discussed as potential sources of spatially extended H_2CO emission in comets (e.g., Meier et al. 1993; Fray et al. 2006). C_2H_2 has not been previously considered as a product species in comets; however, it is possible that larger organic molecules such as polyynes or polyacetylene could be an additional source of C_2H_2 in the comae of comets (e.g., Dudley & Hu 2009). Recent results from Rosetta suggest that ammonium salts could be a possible additional source of NH_3 in cometary comae (e.g., Altwegg et al. 2020). Based on NH_3 spatial profiles in C/2014 Q2 Lovejoy and other comets such as C/2012 S1 ISON (DiSanti et al. 2016; Dello Russo et al. 2016b), the parent of NH_3 would have a short lifetime in the coma. Ammonium salts are more volatile than most refractory material (Poch et al. 2020), but additional work beyond the scope of this paper needs to be done to see whether lifetimes for ammonium salts are consistent with NH_3 spatial distributions in comets. We note that ammonium salts have also been invoked as possible parents for HCN (Poch et al. 2020); however, there is no evidence for an extended source of HCN in C/2014 Q2 Lovejoy even though HCN is four times less abundant than NH_3. This suggests that for ammonium salts to be primarily responsible for the extended source of NH_3, their breakdown must be considerably more efficient in producing NH_3 than HCN.

It is also worth considering whether the high affinity of H_2CO, NH_3, and C_2H_2 with H_2O could form either hydrogen bonds or clusters in ices that would decrease the volatility of these complexes compared with pure molecular ices (e.g., Tzeli et al. 2000; Duvernay et al. 2014; Escamilla-Roa & Sainz-Diaz 2014). The identities and importance of potential additional sources of C_2H_2, H_2CO, and NH_3 in comets need further study, and observational opportunities on comets that can address this should be prioritized, as well as comet sample return missions that can preserve these potential semivolatile sources.

The quantitative study of volatile spatial distributions presented here can be applied to other bright comets observed at IR wavelengths and thus reveal how volatiles may be associated and released from the nucleus. For example, spatial results obtained here for C/2014 Q2 (Lovejoy) can be compared with the outgassing behavior observed in 103P/Hartley 2. Ground-based IR data revealed molecular associations of two general types in 103P: (1) H_2O and CH_3OH showed extended emission in the antisunward direction relative to dust, suggesting significant release from icy grains mixed with little or no micron-sized dust (Dello Russo et al. 2011, 2013; Mumma et al. 2011; Bonev et al. 2013; Kawakita et al. 2013), and (2) C_2H_6 and C_2H_2 showed no extended emission in the antisunward direction relative to the dust and were uncorrelated to H_2O-type spatial profiles in 103P (Dello Russo et al. 2011, 2013; Mumma et al. 2011; Kawakita et al. 2013), suggesting direct release from the nucleus, possibly associated with the prominent CO_2 outgassing

observed by EPOXI (e.g., A'Hearn et al. 2011). Although outgassing behaviors in C/2014 Q2 (Lovejoy) and 103P/Hartley 2 appear dissimilar, these observations were obtained over significantly different spatial scales (projected distances at the comets of ∼110 km pixel^{-1} vs. ∼16 km pixel^{-1}, respectively), so a more rigorous analysis of 103P/Hartley 2 must be done for a proper comparison. A global comparison between a large subset of appropriately bright comets at different spatial scales within the IR database is a logical next step to ascertain which spatial properties are general and which are comet-specific.

6. Conclusions

The apparition of C/2014 Q2 (Lovejoy) allowed a detailed study of the chemical abundances and the spatial distributions in the coma of a suite of simple molecules over two dates. In particular, strong evidence for the first ground-based detection of C_2H_4 in a comet is reported along with C_2H_4 production rates and mixing ratios relative to H_2O and other hydrocarbons. Identification and quantification of C_2H_4 in C/2014 Q2 (Lovejoy) provides a more complete picture of the hydrocarbon chemistry in this comet compared with others. In addition, a sensitive upper limit for HC_3N is reported, suggesting that it is depleted in C/2014 Q2 (Lovejoy) relative to the few other comets where it has been measured at radio wavelengths. For species that are traditionally detected in comets at IR wavelengths, abundances are determined to be in the typical range of what has been measured in comets to date. This study revealed small but significant variability in both gas production rates and rotational temperatures on timescales that are small compared with the comet rotation period of ∼18 hr, illustrating the dynamic behavior of this highly active comet shortly after perihelion. Minor differences are also measured in the relative abundances of volatiles during this time, but variations are small compared with the chemical diversity seen between individual comets within the overall population.

Twenty-seven independent determinations of gas rotational temperatures are obtained from eight different volatiles. Rotational temperatures of C_2H_6, CH_4, HCN, and C_2H_2 are generally consistent with co-measured H_2O, whereas T_{rot} values for CH_3OH and CO are slightly lower, and T_{rot} for H_2CO is slightly higher. As with production rates and relative abundances, T_{rot} measurements also show some short-term variability. Seven independent measurements of the H_2O OPR are in agreement, consistent with the high-temperature statistical equilibrium OPR = 2.96±0.12 and $T_{spin} \geqslant 39$ K.

The high activity of the comet allowed a detailed study of volatile spatial distributions in the coma. Here we introduce a technique for a quantitative study of volatile spatial distributions that can be applied to bright comets observed at IR wavelengths revealing how volatiles may be associated and released from the nucleus. CH_3OH, HCN, C_2H_6, and CH_4 have similar spatial profiles, consistent with the association of these ices in the nucleus and their release into the coma predominantly from the direct sublimation of these ices. H_2O spatial profile properties are most consistent with an H_2O nucleus ice source associated with CH_3OH, HCN, C_2H_6, and CH_4 ices, with a substantial additional source of H_2O from icy grain sublimation predominantly in the antisunward coma. The CO spatial profiles suggest that CO nucleus ices are distinct from the other measured volatiles, with the additional extension in the sunward direction possibly due to CO-rich jets, though a

contribution from an extended source in the sunward coma cannot be ruled out.

C_2H_2 and H_2CO spatial profiles provide strong evidence for significant contributions from extended sources in the coma for these species. The source of NH_3 is more ambiguous, as its profile is broader closer to the profile peak but is not extended in the wings farther from the nucleus as is the case for C_2H_2 and H_2CO. This is consistent with the primary source of NH_3 being direct release from nucleus ice, but with a contribution due to an extended source from a short-lived parent. Additional work beyond the scope of this paper needs to be done to see if lifetimes and product yields for ammonium salts are consistent with NH_3 spatial distributions in comets. This spatial study of C/2014 Q2 (Lovejoy), along with a global study of comets at IR wavelengths, provides strong evidence for different sources and associations for C_2H_2, H_2CO, and NH_3 in comets compared with other measured volatile species.

Spatial profiles from most of the strongest unidentified lines in the spectra are broader and shifted antisunward compared with the co-measured dust continuum and the primary parent volatile profiles, suggesting that most of these strong unidentified emissions have substantial or dominant extended coma sources. Spatial studies such as presented here could be extended to the global population, helping to reveal which spatial properties are specific to individual comets and which are general properties observed in most or all comets.

Appendix

Nine tables are included. Tables A1–A7 show all unblended emissions from every setting used in the analysis on both dates. The tables contain the following information (where available): molecule, band and line identification, line or emission position (cm^{-1}), line or emission g-factor ($\times 10^{-7}$ photons molecules^{-1} s^{-1}), line flux ($\times 10^{-19}$ W m^{-2}), and calculated production rate ($\times 10^{27}$ molecules s^{-1}) from each detected emission. Table A8 gives setting-by-setting information on the characteristics of volatile spatial profiles. Table A9 gives information on the
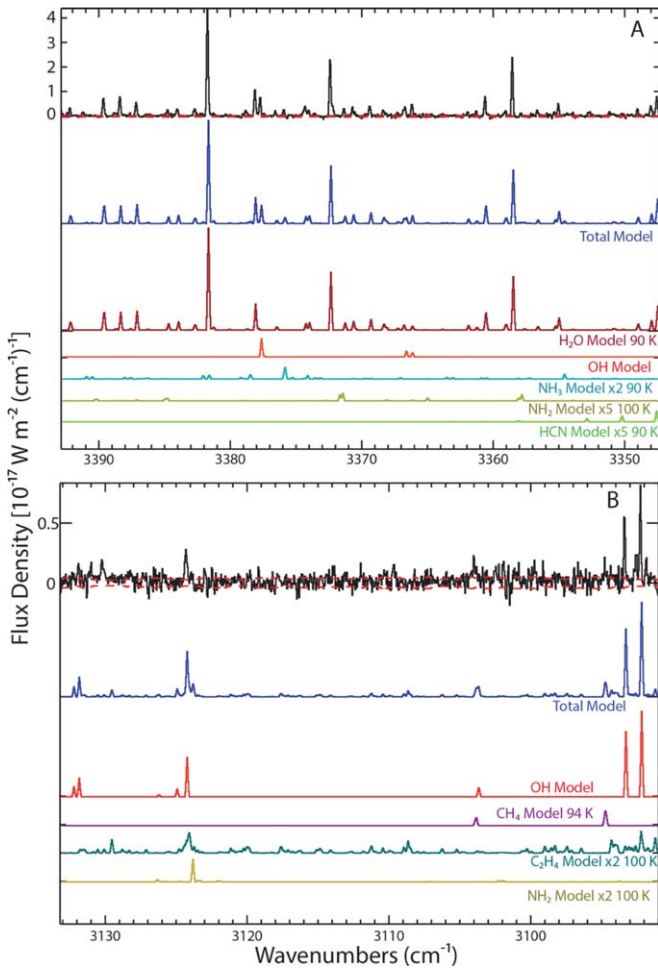
Figure A1. Flux-calibrated high-resolution ($\lambda/\Delta\lambda \sim 25{,}000$) spectral residuals and best-fit fluorescence models for C/2014 Q2 (Lovejoy) on (a) February 2, setting KL1 order 26, and (b) February 2, setting KL1 order 24. On the top of each frame are spectral residuals co-added over 3 spectral $\times$ 9 spatial pixel extracts ($0\rlap{.}''432 \times 1\rlap{.}''71$) centered on the peak of the gas emission. The dashed red curves superimposed on the comet residuals are the estimated $\pm 1\sigma$ channel-by-channel photon noise. The solid blue curves directly below the spectral residuals are the total best-fit fluorescence models convolved to the resolution of the comet spectra that include all molecules. Subsequent color traces below this are the best-fit fluorescence models at the derived or assumed rotational temperatures for each individual molecule.

Figure A2. Similar to Figure A1, but for (a) February 3, setting KL4 order 25, and (b) February 3, setting M2 order 16.

spatial properties of the 16 strongest unidentified emissions in the C/2014 Q2 (Lovejoy) spectra on February 2.

Eight figures are also included. Figures A1–A2 show flux-calibrated high-resolution spectral residuals and best-fit fluorescence models in several additional settings in C/2014 Q2 (Lovejoy) on both dates. Figure A3 shows flux-calibrated high-resolution spectral residuals and best-fit fluorescence models in C/2014 Q2 (Lovejoy), illustrating the unblended emissions used for the HC$_3$N analysis and some emissions used for the NH$_3$ analysis. Figure A4 shows flux-calibrated high-resolution spectral residuals and best-fit

fluorescence models for zoomed-in spectral regions of interest from Figure 2. For additional validation, we did iterative fitting based on Levenberg–Marquardt χ^2 minimization of the comet residuals (e.g., Villanueva et al. 2008; DiSanti et al. 2016) to independently derive production rates and rotational temperatures in order 25 setting KL3, which agreed within uncertainties with the values derived by line-by-line analysis. Figure A5 shows the minimized residuals after subtracting fluorescence models from the spectral extract in order 25 setting KL3. Figure A6 shows the spatial profiles for NH$_2$ and OH on UT 2015 February 2 in each of the L-band settings. Figure A7 shows the spatial profile properties of volatiles and dust on both dates (sunward/antisunward flux vs. spatial profile half-widths at half-maximum). Figure A8 shows the spatial profile properties of the 16 strongest unidentified emissions on February 2, based on the data in Table A8 (spatial profile peak position vs. spatial profile half-widths at half-maximum).
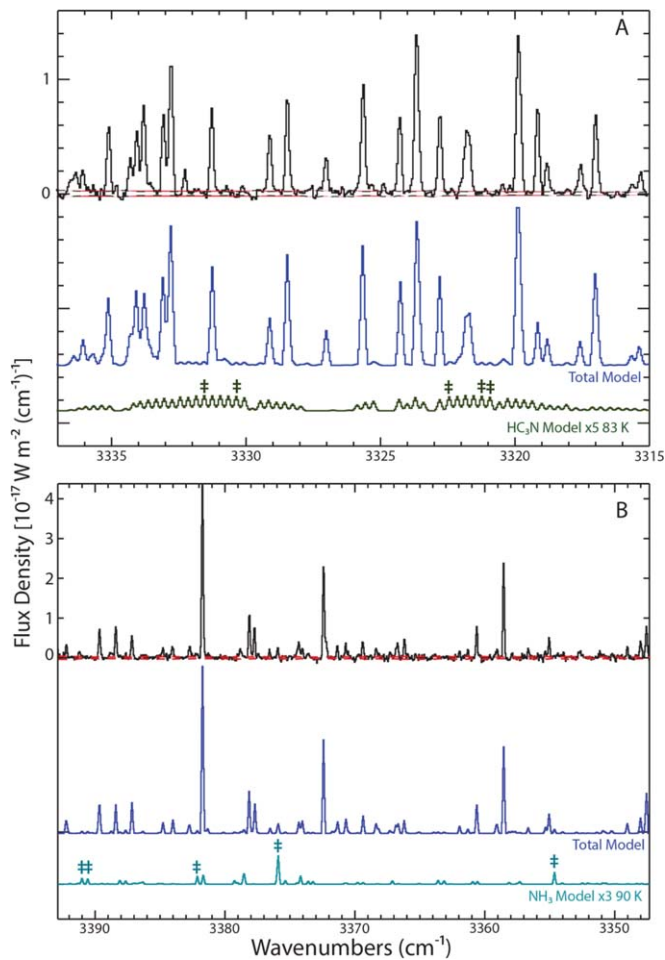
Figure A3. Flux-calibrated high-resolution ($\lambda/\Delta\lambda \sim 25{,}000$) spectral residuals and best-fit fluorescence models for C/2014 Q2 (Lovejoy) on (a) February 2, setting KL3 order 25, and (b) February 2, setting KL1 order 26, illustrating the emissions used for the HC_3N and NH_3 analyses. On the top of each frame are spectral residuals co-added over 3 spectral $\times$ 9 spatial pixel extracts ($0\rlap{.}''432 \times 1\rlap{.}''71$) centered on the peak of the gas emission. The dashed red curves superimposed on the comet residuals are the estimated $\pm 1\sigma$ channel-by-channel photon noise. The solid blue curves directly below the spectral residuals are the total best-fit fluorescence models convolved to the resolution of the comet spectra that include all molecules. Below the total models are the best-fit C_2H_4 and NH_3 models. The unblended emissions that are used in the analysis are labeled (‡).
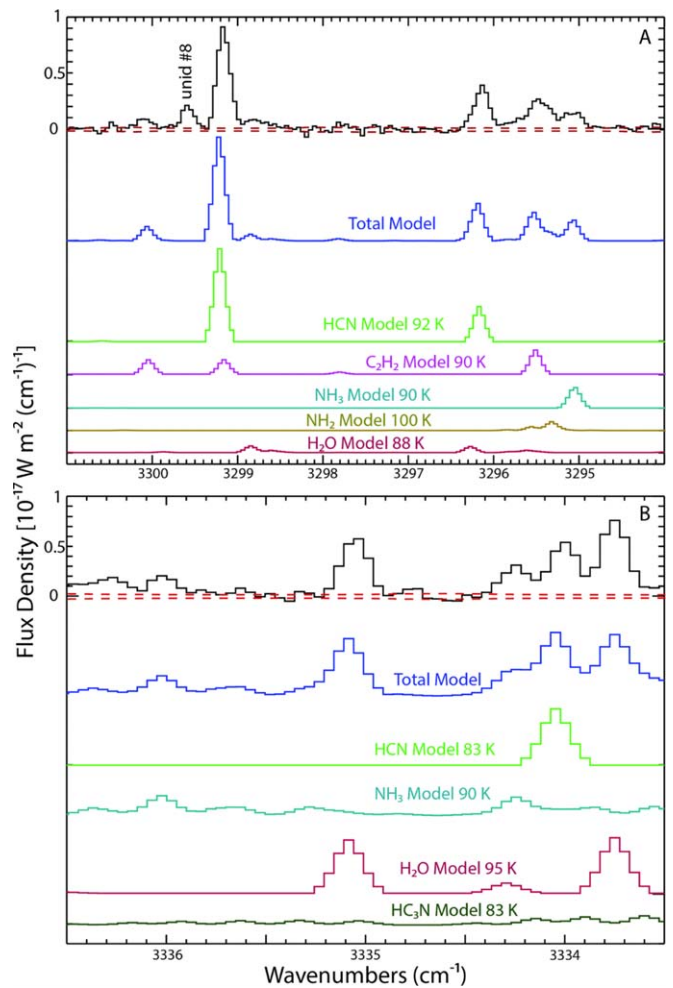
Figure A4. Flux-calibrated high-resolution ($\lambda/\Delta\lambda \sim 25{,}000$) spectral residuals and best-fit fluorescence models for C/2014 Q2 (Lovejoy) zoomed in on regions of interest in Figure 2, primarily highlighting C_2H_2 and NH_3 emissions, as well as emissions from other species and a strong unidentified line (line #8 in Table A9). (a) February 2, setting KL2 order 25. (b) February 2, setting KL3 order 25. On the top of each frame are spectral residuals co-added over 3 spectral $\times$ 9 spatial pixel extracts ($0\rlap{.}''432 \times 1\rlap{.}''71$) centered on the peak of the gas emission. Dashed red curves superimposed on the comet residuals are the estimated $\pm 1\sigma$ channel-by-channel photon noise. Solid blue curves directly below the spectral residuals are the total best-fit fluorescence models convolved to the resolution of the comet spectra including all molecules. Below the total models are the best-fit models for individual species.
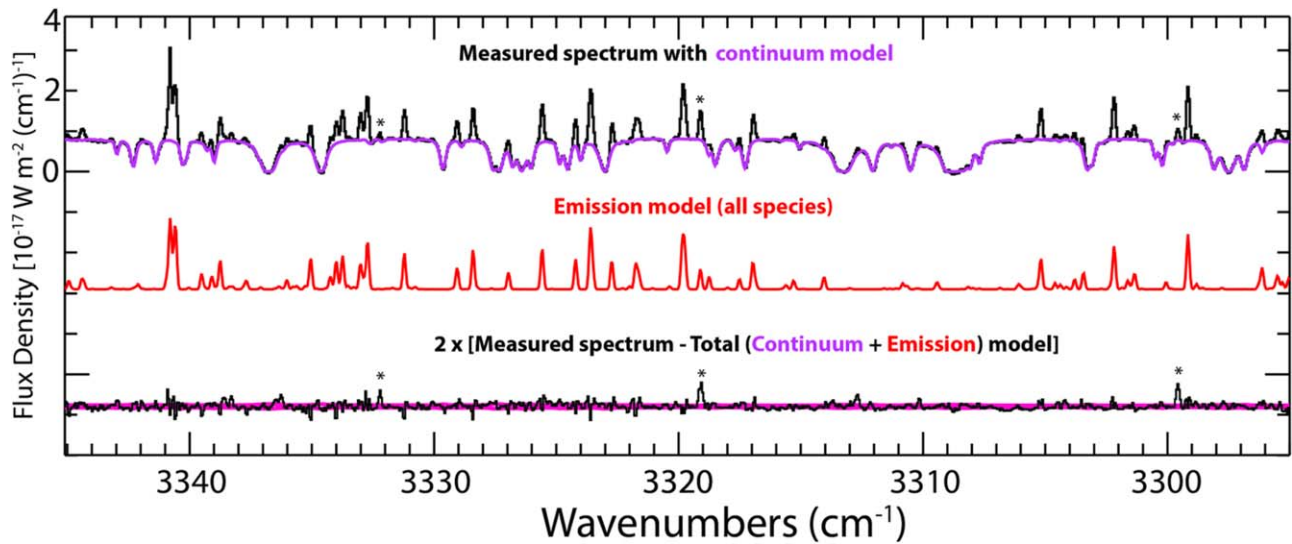
Figure A5. An iterative fitting based on Levenberg–Marquardt χ^2 minimization of the comet residuals in setting KL3 order 25. The top traces are the flux-calibrated spectrum (black trace) with best-fit continuum model (violet trace). The middle red trace is the best-fit fluorescence emission model. The bottom black trace is the measured spectrum minus the continuum and emission models (multiplied by 2), outlined in red by the $\pm 1\sigma$ channel-by-channel photon noise. Unidentified features are marked with an asterisk.
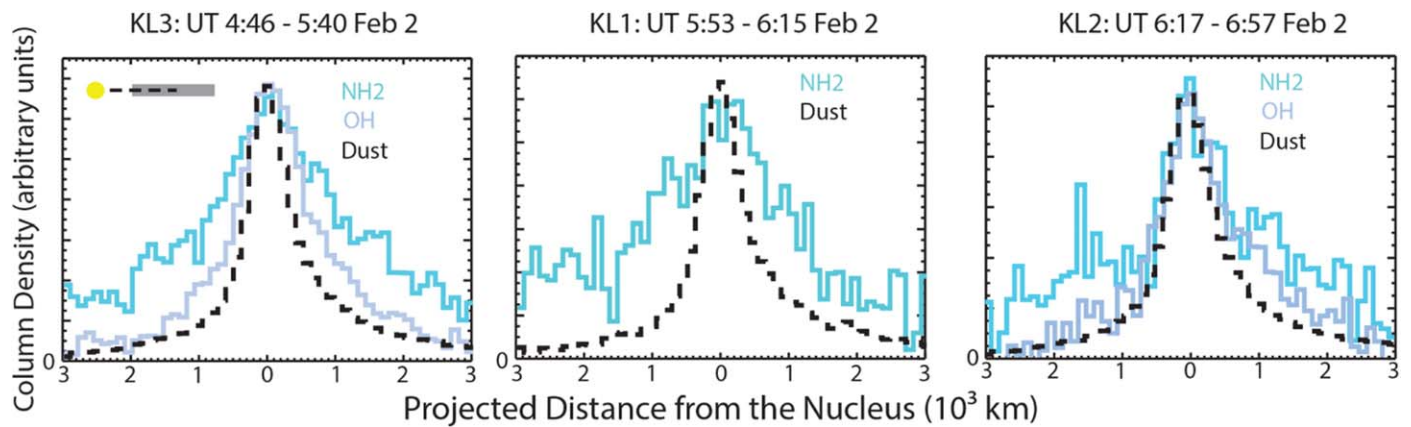
Figure A6. Spatial profiles of product volatiles (NH_2 and OH) and co-measured dust along the slit at different times (settings) on February 2 in the coma of C/2014 Q2 (Lovejoy). Volatile gas column densities (solid colored traces) are compared with simultaneously obtained dust column densities (dashed black traces) scaled to the peak of the gas. The position of the slit with respect to the Sun is given in panel (a).
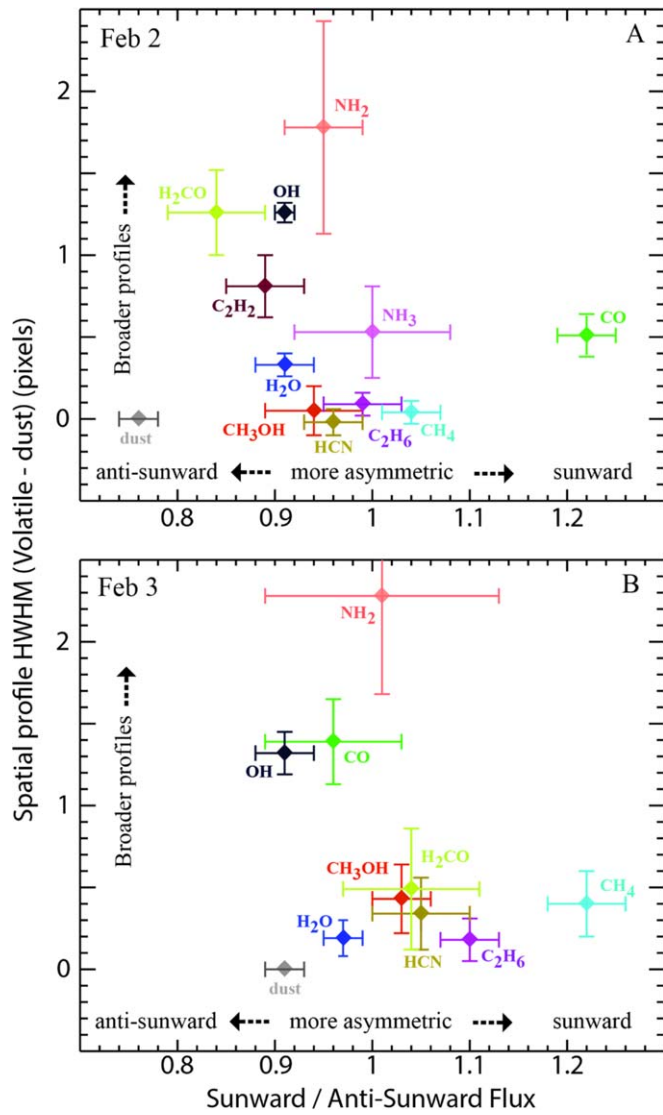
Figure A7. Comparison of the symmetry of spatial profiles as measured by the ratio of the sunward to antisunward flux (for a projected distance in the range of ~300–2400 km from the peak of the profile on both sides of the slit) and width (half-width at half-maximum) of volatile spatial profiles relative to the co-measured dust continuum in pixels (1 spatial pixel ~ 110 km projected distance at the comet). X-axis values = 1 indicate symmetric profiles, whereas values >1 indicate increasing sunward asymmetry, and values <1 indicate increasing antisunward asymmetry. (a) February 2; (b) February 3.
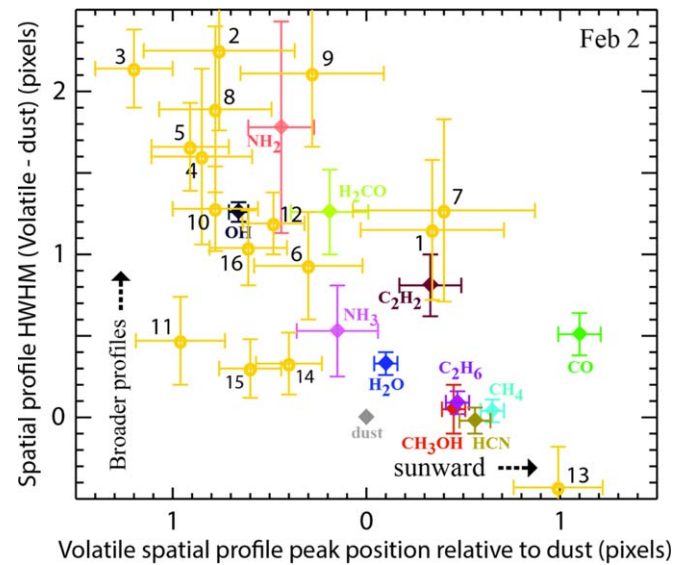
Figure A8. Peak position and width (half-width at half-maximum) of the 16 strongest unidentified emissions (gold numbered points) compared with spatial profiles of identified volatiles and the co-measured dust continuum on February 2. Differences are measured in spatial pixels with 1 pixel ~ 110 km projected distance at the comet.

Table A1
Line Positions, Fluxes, and Production Rates in C/2014 Q2 (Lovejoy) on UT 2015 February 2 Setting KL3

Molecule	Band ID	Line ID[a]	Line Pos. (cm^{-1})[b]	g-factor (10^{-7} s^{-1})[c]	Line Flux (10^{-19} W m^{-2})[d]	Q (10^{27} s^{-1})[e]
H_2O (95 ± 3 K)	$\nu_2 + \nu_3 - \nu_2$	4_{13}–5_{32}(o)	3 477.79	0.10	6.61 ± 0.88	861 ± 122
	ν_1	3_{22}–4_{31} (p)	3 475.03	2.29	152 ± 15	884 ± 97
	blend	2 lines (p)	3 474.7	0.11	7.34 ± 0.52	868 ± 76
	$2\nu_1 + \nu_3 - 2\nu_1$	3_{03}–2_{02} (p)	3 474.31	0.04	2.14 ± 0.32	652 ± 103
	blend	3 lines (b)	3473.35	0.26	9.83 ± 0.54	507 ± 38
	blend	3 lines (b)	3472.8	0.28	10.4 ± 0.2	489 ± 26
	blend	3 lines (b)	3472.36	0.26	9.03 ± 0.68	457 ± 41
	$\nu_1 + \nu_3 - \nu_1$	4_{23}–5_{24} (p)	3471.43	0.46	17.3 ± 0.6	500 ± 30
	$\nu_1 + \nu_2 - \nu_2$	2_{21}–3_{30} (o)	3471.13	0.19	7.15 ± 0.31	501 ± 33
	blend	2 lines (o)	3469.89	0.03	1.66 ± 0.29	679 ± 124
	$2\nu_1 + \nu_3 - 2\nu_1$	3_{13}–2_{12} (o)	3469.57	0.10	4.87 ± 0.26	630 ± 46
	blend	7 lines (b)	3468.7	3.82	172 ± 1	603 ± 30
	$\nu_1 + \nu_3 - \nu_1$	4_{13}–5_{14} (o)	3467.68	2.77	115 ± 1	555 ± 28
	ν_1	8_{18}–9_{09} (o)	3466.89	0.05	6.22 ± 0.40	1566 ± 128
		4_{22}–5_{33} (p)	3462.59	1.38	56.3 ± 1.7	545 ± 32
	$2\nu_1 + \nu_3 - 2\nu_1$	2_{11}–1_{10} (o)	3461.09	0.12	3.78 ± 0.26	420 ± 36
	blend	3 lines (b)	3459.53	0.68	29.4 ± 0.2	577 ± 29
	$\nu_1 + \nu_3 - \nu_3$	0_{00}–1_{11} (o)	3458.12	0.61	27.1 ± 0.4	591 ± 31
	$\nu_1 + \nu_3 - \nu_1$	4_{22}–5_{23} (o)	3456.45	1.30	53.7 ± 0.4	553 ± 28
	blend	4 lines (o)	3455.9	0.89	36.8 ± 0.7	555 ± 30
	$\nu_1 + \nu_3 - \nu_3$	3_{03}–3_{12} (p)	3455.40	0.09	2.80 ± 0.15	431 ± 32
		3_{12}–3_{21} (p)	3455.14	0.10	3.49 ± 0.15	484 ± 31
		2_{11}–2_{20} (o)	3454.69	0.52	25.3 ± 0.2	649 ± 33
	blend	2 lines (o)	3453.22	1.56	81.8 ± 0.2	703 ± 35
	blend	3 lines (b)	3450.9	0.21	9.96 ± 0.18	628 ± 33
	$2\nu_1 - \nu_3$	1_{10}–1_{11} (o)	3450.29	1.20	72.8 ± 0.2	813 ± 41
	blend	3 lines (b)	3449.72	0.18	8.87 ± 0.21	667 ± 37
	blend	2 lines (o)	3449.37	0.45	20.8 ± 0.3	622 ± 32
	$2\nu_1 - \nu_3$	2_{20}–2_{21} (p)	3445.89	0.36	14.5 ± 0.2	539 ± 28
		2_{21}–2_{20} (o)	3442.31	1.45	96.5 ± 1.3	900 ± 47
	blend	2 lines (o)	3341.6	0.30	16.3 ± 0.3	734 ± 39
	blend	3 lines (b)	3440.7	0.12	9.06 ± 0.48	1038 ± 75
	blend	3 lines (p)	3439.85	0.49	34.1 ± 0.2	941 ± 47
	$\nu_1 + \nu_3 - \nu_3$	1_{01}–2_{12} (p)	3439.42	0.25	14.2 ± 0.2	773 ± 40
	blend	2 lines (o)	3436.64	0.18	6.67 ± 0.23	488 ± 30
	$2\nu_1 + \nu_3 - 2\nu_1$	1_{01}–0_{00} (p)	3434.96	0.04	2.50 ± 0.11	799 ± 53
	blend	3 lines (p)	3434.36	0.40	24.2 ± 0.2	808 ± 41
	ν_1	6_{24}–7_{35} (p)	3432.83	0.05	4.20 ± 0.29	1168 ± 99
	ν_1	4_{14}–5_{23} (o)	3431.06	1.36	82.5 ± 0.7	819 ± 42
	$\nu_1 + \nu_3 - \nu_1$	7_{17}–8_{18} (o)	3428.60	0.10	6.49 ± 0.36	920 ± 68
	blend	3 lines (b)	3427.9	0.45	19.5 ± 0.3	584 ± 31
	$2\nu_1 - \nu_3$	2 lines (o)	3341.05	0.98	59.3 ± 0.3	858 ± 43
		4_{04}–5_{05} (p)	3339.46	0.14	8.53 ± 0.41	873 ± 60
		3_{21}–4_{22} (o)	3339.12	0.22	11.2 ± 0.2	720 ± 39
	blend	2 lines (b)	3338.7	0.04	3.56 ± 0.22	1312 ± 104
	$2\nu_1 - \nu_1$	2 lines (b)	3338.1	0.08	2.97 ± 0.25	509 ± 50
		4_{23}–5_{32} (o)	3335.42	0.30	13.7 ± 0.3	660 ± 37
	$2\nu_1 + \nu_3 - 2\nu_1$	2_{11}–3_{12} (o)	3334.11	0.24	14.5 ± 0.2	875 ± 46
	blend	2 lines (o)	3329.42	0.17	10.1 ± 0.3	851 ± 48
	ν_1	5_{05}–6_{34} (o)	3327.33	0.19	9.08 ± 0.43	678 ± 46
	$2\nu_1 - \nu_3$	4_{31}–5_{32} (p)	3320.74	0.02	1.54 ± 0.19	943 ± 123
		5_{05}–6_{06} (o)	3319.47	0.15	13.4 ± 0.2	1285 ± 66
	$\nu_1 + \nu_3 - \nu_1$	3_{22}–4_{31} (o)	3319.12	0.29	15.2 ± 0.6	756 ± 48
	blend	2 lines (b)	3316.0	0.04	1.63 ± 0.15	666 ± 68
	blend	3 lines (p)	3309.8	0.10	5.83 ± 0.37	829 ± 67
	$2\nu_1 - \nu_3$	6_{16}–7_{17} (o)	3299.18	0.04	2.87 ± 0.15	1045 ± 77
		6_{06}–7_{07} (p)	3298.93	0.01	1.30 ± 0.17	1126 ± 196
CH_3OH (88 K)	ν_2	3 lines	3055.4	1.26	1.63 ± 0.19	21.7 ± 2.7
		6 lines	3039.47	2.80	1.42 ± 0.16	8.17 ± 1.03
		20 lines	3037.8	5.33	1.69 ± 0.16	5.24 ± 0.56
	unassigned		2942.45		4.32 ± 0.19	
			2941.66		6.06 ± 0.17	
			2939.88		2.67 ± 0.18	
			2935.23		7.04 ± 0.23	

Table A1
(Continued)

Molecule	Band ID	Line ID[a]	Line Pos. (cm^{-1})[b]	g-factor (10^{-7} s^{-1})[c]	Line Flux (10^{-19} W m^{-2})[d]	Q (10^{27} s^{-1})[e]
			2934.90		3.01 ± 0.19	
			2934.48		12.4 ± 0.3	
			2933.21		4.96 ± 0.22	
			2932.86		8.27 ± 0.24	
			2932.34		5.36 ± 0.32	
			2931.97		13.0 ± 0.3	
			2931.13		3.32 ± 0.18	
			2930.84		8.84 ± 0.26	
			2929.99		7.81 ± 0.18	
			2929.57		5.58 ± 0.24	
			2929.05		15.5 ± 0.3	
			2928.66		5.85 ± 0.23	
			2925.76		4.43 ± 0.21	
			2924.39		10.7 ± 0.2	
			2923.33		11.3 ± 0.2	
			2922.89		4.42 ± 0.17	
			2921.51		12.4 ± 0.2	
			2920.99		14.2 ± 0.2	
			2920.11		15.5 ± 0.2	
			2919.78		25.2 ± 0.2	
			2919.37		16.0 ± 0.3	
			2918.50		3.55 ± 0.16	
			2916.93		4.99 ± 0.29	
			2914.84		6.01 ± 0.18	
			2913.49		10.4 ± 0.2	
			2910.09		12.6 ± 0.3	
			2909.47		3.16 ± 0.16	
			2908.03		6.18 ± 0.17	
			2906.68		4.91 ± 0.27	
			2905.31		2.76 ± 0.17	
			2903.82		1.50 ± 0.17	
			2902.41		5.23 ± 0.16	
			2902.14		5.07 ± 0.32	
C$_2$H$_6$ (90 $\pm$ 10 K)	blend	8 lines	2942.15	15.3	4.28 ± 0.20	4.52 ± 0.31
	blend	7 lines	2939.6	11.3	3.05 ± 0.18	4.34 ± 0.34
	ν_5	10 lines	2915.5	29.1	10.9 ± 0.2	6.08 ± 0.33
		2 lines	2912.77	6.75	3.02 ± 0.17	7.27 ± 0.56
		14 lines	2910.6	55.3	16.9 ± 0.2	4.97 ± 0.25
		14 lines	2909.1	57.0	26.9 ± 0.2	7.68 ± 0.39
		12 lines	2907.35	57.5	17.7 ± 0.2	5.03 ± 0.26
		18 lines	2905.8	59.6	15.5 ± 0.2	4.24 ± 0.22
		16 lines	2904.3	60.8	24.9 ± 0.3	6.69 ± 0.34
		12 lines	2902.75	43.4	12.4 ± 0.2	4.65 ± 0.24
CH$_4$ (91 $\pm$ 3 K)	ν_3	R5	3076.6	144	43.6 ± 0.7	4.65 ± 0.25
		R3	3057.7	435	137 ± 1	4.87 ± 0.25
		R2	3048.16	249	81.3 ± 0.4	5.05 ± 0.25
		R1	3038.50	147	42.0 ± 0.2	4.43 ± 0.22
NH$_3$ (90 K)	blend	2 lines	3444.48	2.79	1.22 ± 0.27	6.35 ± 1.45
	ν_3	srQ(3,0)	3437.37	4.76	2.50 ± 0.12	7.65 ± 0.52
	blend	3 lines	3434.0	3.28	1.42 ± 0.17	6.30 ± 0.80
	ν_3	2 lines	3336.4	17.2	4.36 ± 0.28	4.33 ± 0.35
		4 lines	3336.05	10.3	1.49 ± 0.28	2.48 ± 0.48
HCN (83 $\pm$ 2 K)	ν_1	R11	3345.31	22.6	2.14 ± 0.18	1.30 ± 0.13
		R9	3339.88	58.0	4.76 ± 0.23	1.13 ± 0.08
		R7	3334.37	117	11.0 ± 0.2	1.30 ± 0.07
		R6	3331.58	151	12.3 ± 0.2	1.12 ± 0.06
		R5	3328.76	183	15.6 ± 0.2	1.18 ± 0.06
		R4	3325.94	204	18.0 ± 0.2	1.22 ± 0.06
		R3	3323.09	208	19.3 ± 0.4	1.28 ± 0.07
		R1	3317.33	146	13.2 ± 0.2	1.26 ± 0.07
		R0	3314.41	80.5	7.02 ± 0.24	1.21 ± 0.07
		P1	3308.52	84.5	8.10 ± 1.66	1.34 ± 0.28
		P2	3305.54	161	13.7 ± 0.2	1.18 ± 0.06
		P3	3302.55	219	17.3 ± 0.1	1.10 ± 0.06

Table A1
(Continued)

Molecule	Band ID	Line ID[a]	Line Pos. (cm^{-1})[b]	g-factor $(10^{-7}\,s^{-1})$[c]	Line Flux $(10^{-19}\,W\,m^{-2})$[d]	Q $(10^{27}\,s^{-1})$[e]
		P4	3299.53	252	22.3 ± 0.2	1.23 ± 0.06
		P5	3296.49	260	23.5 ± 0.4	1.27 ± 0.07
C_2H_2 (90 K)	$\nu_2 + \nu_4 - \nu_5$	R9	3304.97	74.5	2.80 ± 0.15	1.19 ± 0.09
	ν_3	R3	3304.17	138	3.67 ± 0.17	0.84 ± 0.06
	$\nu_2 + \nu_4 - \nu_5$	R7	3300.42	118	4.00 ± 0.23	1.08 ± 0.08
		R5	3295.84	152	6.05 ± 0.15	1.27 ± 0.07
H_2CO (110 $\pm$ 6 K)	ν_1	2 lines	2807.6	16.3	0.87 ± 0.23	2.51 ± 0.50
	ν_5	$13_{013}-14_{114}$	2806.87	10.5	0.61 ± 0.15	2.74 ± 0.69
	blend	3 lines	2805.17	27.7	1.13 ± 0.18	1.93 ± 0.33
	blend	3 lines	2802.4	58.0	3.35 ± 0.24	2.73 ± 0.24
	blend	14 lines	2801.65	150	5.14 ± 0.29	1.62 ± 0.12
	blend	4 lines	2801.38	24.1	0.63 ± 0.16	1.24 ± 0.31
	ν_1	2 lines	2800.37	27.1	1.90 ± 0.16	3.32 ± 0.32
	blend	2 lines	2799.9	40.3	1.74 ± 0.18	2.04 ± 0.24
	blend	6 lines	2799.35	31.4	1.39 ± 0.22	2.09 ± 0.34
	blend	5 lines	2797.95	31.0	1.75 ± 0.19	2.66 ± 0.32
	ν_1	3 lines	2796.9	18.9	1.42 ± 0.18	3.57 ± 0.49
	blend	5 lines	2796.4	62.8	4.92 ± 0.26	3.71 ± 0.27
	blend	5 lines	2795.55	32.0	2.71 ± 0.20	4.01 ± 0.35
	ν_5	$5_{14}-4_{13}$	2794.86	38.8	1.90 ± 0.16	2.32 ± 0.23
	blend	7 lines	2794.43	75.0	3.14 ± 0.21	1.98 ± 0.16
	ν_1	$4_{13}-3_{12}$	2792.35	35.6	1.96 ± 0.17	2.60 ± 0.26
	ν_5	2 lines	2791.96	51.0	2.42 ± 0.19	2.25 ± 0.21
	ν_1	3 lines	2791.6	49.2	1.83 ± 0.17	1.76 ± 0.18
	blend	7 lines	2789.4	88.8	3.68 ± 0.25	1.97 ± 0.17
	blend	3 lines	2787.05	61.7	2.42 ± 0.18	1.86 ± 0.17
	blend	4 lines	2784.75	28.4	1.48 ± 0.21	2.48 ± 0.37
	ν_5	12 lines	2784.4	47.9	2.01 ± 0.17	2.00 ± 0.20
	blend	16 lines	2782	133	7.30 ± 0.28	2.61 ± 0.17
	ν_1	17 lines	2780.95	143	6.95 ± 0.17	2.31 ± 0.13
	ν_1	15 lines	2779.9	47.2	2.11 ± 0.18	2.13 ± 0.21
	ν_5	$8_{27}-9_{36}$	2779.46	13.9	0.68 ± 0.14	2.32 ± 0.50
	ν_1	12 lines	2778.45	33.0	1.07 ± 0.15	1.55 ± 0.22
		$1_{10}-2_{11}$	2777.28	19.1	1.67 ± 0.15	4.17 ± 0.42
		2 lines	2775.2	45.7	1.30 ± 0.15	1.36 ± 0.17
	blend	4 lines	2774.77	47.8	2.00 ± 0.16	2.00 ± 0.18
	ν_1	2 lines	2774.53	9.68	0.61 ± 0.14	3.01 ± 0.72
	blend	3 lines	2772.8	60.0	1.73 ± 0.21	1.38 ± 0.18
	blend	3 lines	2772.3	54.1	2.57 ± 0.16	2.27 ± 0.18
	blend	5 lines	2771.35	29.0	1.48 ± 0.19	2.43 ± 0.34
C_2H_4 (100 K)	ν_9	6 lines	3076	6.32	0.00 ± 0.17	0.00 ± 0.42
		5 lines	3074.8	4.96	0.14 ± 0.15	0.43 ± 0.46
		7 lines	3074	7.75	0.30 ± 0.23	0.61 ± 0.47
		17 lines	3069	11.3	1.49 ± 0.22	2.06 ± 0.32
		29 lines	3060.8	21.8	1.37 ± 0.43	0.98 ± 0.31
		3 lines	3054	3.85	0.78 ± 0.15	3.14 ± 0.61
		2 lines	3050	5.53	0.72 ± 0.21	2.02 ± 0.59
HC_3N (83 K)	ν_1	5 lines	3321.2–3332.2	1019	0.50 ± 0.50	0.005 ± 0.009
NH_2 (100 K)	ν_1	$2_{20}-1_{11}$	3302.1	50.7	3.32 ± 0.18	
		$2_{20}-1_{11}$	3301.71	82.1	6.08 ± 0.14	
		$1_{01}-1_{10}$	3203.62	55.8	3.70 ± 0.15	
		$2_{02}-2_{11}$	3196.86	139	7.60 ± 0.54	
		$0_{00}-1_{11}$	3187.60	121	7.79 ± 0.11	
		$0_{00}-1_{11}$	3187.37	60.2	4.26 ± 0.11	
		4 lines	3184.8	79.7	4.04 ± 0.26	
		$2_{11}-2_{20}$	3184.46	36.0	2.50 ± 0.18	
		$4_{13}-4_{22}$	3181.5	81.2	5.84 ± 0.14	
		$1_{01}-2_{12}$	3170.8	79.2	4.62 ± 0.14	
		$4_{04}-4_{13}$	3168.0	39.9	1.70 ± 0.17	
		$2_{12}-3_{03}$	3166.54	54.7	2.77 ± 0.18	
		$3_{21}-4_{32}$	3069.99	14.8	1.00 ± 0.17	
		$3_{22}-4_{31}$	3062.67	37.2	1.93 ± 0.20	
		$3_{22}-4_{31}$	3062.40	28.5	1.50 ± 0.17	
		$4_{22}-5_{33}$	3052.48	15.1	1.24 ± 0.17	

Table A1
(Continued)

Molecule	Band ID	Line ID[a]	Line Pos. (cm^{-1})[b]	g-factor (10^{-7} s^{-1})[c]	Line Flux (10^{-19} W m^{-2})[d]	Q (10^{27} s^{-1})[e]
		$3_{31}-4_{40}$	3040.04	32.2	1.65 ± 0.13	
OH	$1 \rightarrow 0$	P2.5 2+/2−	3465.26		55.8 ± 0.2	
		P5.5 2+	3333.38		12.3 ± 0.2	
		P6.51+	3324.58		13.8 ± 0.3	
		P8.5 2−	3194.28		12.9 ± 0.1	
		P8.5 2+	3193.68		11.7 ± 0.1	
		P9.5 1−	3189.40		15.0 ± 0.1	
		P11.5 2+	3047.46		15.8 ± 0.2	
		P11.5 2−	3046.55		9.83 ± 0.15	
		P12.5 1+	3044.43		17.0 ± 0.2	
		P12.5 1−	3043.21		11.4 ± 0.1	
		P14.5 1−	2941.86		9.41 ± 0.18	
		P16.5 2−	2787.47		11.4 ± 0.2	
		P16.5 2+	2786.15		3.11 ± 0.15	
		P17.5 1−	2785.87		9.78 ± 0.16	
		P17.5 1+	2784.19		3.46 ± 0.16	
	$2 \rightarrow 1$	P1.5 2+/2−	3344.7		6.19 ± 0.22	
		P2.5 2+/2−	3303.8		11.7 ± 0.4	
		P5.5 1+	3208.17		7.40 ± 0.15	
		P5.5 2+	3176.59		4.11 ± 0.12	
		P5.5 2−	3176.32		5.24 ± 0.12	
		P6.5 1+	3167.67		4.00 ± 0.15	
		P6.5 1−	3167.07		10.7 ± 0.3	
		P8.5 2−	3042.07		3.76 ± 0.14	
		P8.5 2+	3041.51		4.79 ± 0.13	
		P9.5 1−	3037.05		4.19 ± 0.17	
	$3 \rightarrow 2$	P1.5 2+/2−	3183.5		0.95 ± 0.12	

Notes.
[a] H_2O line identifications indicate emissions that are ortho (o), para (p), or a blend of both (b).
[b] Rest positions for single lines or average rest positions for multiple lines.
[c] The g-factors at $R_h = 1$ au for the derived or assumed rotational temperature given below the molecular assignment in parentheses.
[d] Line fluxes within a 3 spectral $\times$ 9 spatial pixel extract ($0{.}''432 \times 1{.}''71$) centered on the peak intensity of the gas spatial profile.
[e] Derived production rates for individual lines corrected for slit losses. Uncertainties include photon noise (reflected in the S/N of individual lines) and an assumed 5% uncertainty per emission in the continuum baseline fit. Calibration and growth factor uncertainties are not included.

Table A2
Line Positions, Fluxes, and Production Rates in C/2014 Q2 (Lovejoy) on UT 2015 February 2 setting KL1

Molecule	Band ID	Line ID[a]	Line Pos. (cm^{-1})[b]	g-factor (10^{-7} s^{-1})[c]	Line Flux (10^{-19} W m^{-2})[d]	Q (10^{27} s^{-1})[e]
H$_2$O (90 ± 2 K)	$\nu_2 + \nu_3 - \nu_2$	2_{11}–3_{30} (o)	3520.56	0.14	6.07 ± 1.47	635 ± 157
	blend	2 lines (b)	3518.9	1.39	66.8 ± 8.5	680 ± 93
	blend	3 lines (b)	3518.15	0.38	21.3 ± 1.2	795 ± 59
	$\nu_1 + \nu_3 - \nu_1$	2_{21}–3_{22} (p)	3517.70	1.02	41.9 ± 5.6	579 ± 83
	$\nu_1 + \nu_3 - \nu_3$	2_{11}–2_{20} (o)	3516.59	0.27	15.4 ± 1.0	792 ± 64
	$\nu_1 + \nu_3 - \nu_1$	2_{11}–3_{12} (o)	3514.41	12.2	591 ± 83	686 ± 102
	blend	3 lines (o)	3513.15	4.55	189 ± 6	588 ± 35
	$\nu_1 + \nu_3 - \nu_1$	3_{13}–4_{14} (o)	3508.67	9.35	392 ± 1	593 ± 30
	blend	3 lines (b)	3508.35	1.01	50.4 ± 1.4	706 ± 41
	$\nu_1 + \nu_3 - \nu_1$	3_{03}–4_{04} (p)	3507.24	3.86	230 ± 2	842 ± 43
	$\nu_1 + \nu_2 - \nu_3 - \nu_1 - \nu_2$	2_{02}–3_{03} (o)	3505.62	0.97	40.3 ± 5.9	590 ± 91
	blend	2 lines (b)	3496.2	0.32	8.28 ± 1.33	367 ± 62
	$\nu_1 + \nu_3 - \nu_1$	3_{22}–4_{23} (o)	3494.26	2.63	102 ± 1	554 ± 28
	$\nu_1 + \nu_2 - \nu_3 - \nu_1 - \nu_2$	2_{11}–3_{12} (o)	3493.95	0.33	15.1 ± 1.0	654 ± 55
	blend	3 lines (b)	3490.25	2.51	96.7 ± 0.5	548 ± 28
	blend	2 lines (b)	3489.7	1.14	47.4 ± 0.9	593 ± 32
	blend	2 lines (o)	3488.1	4.99	171 ± 11	487 ± 40
	blend	3 lines (b)	3486.35	0.81	29.0 ± 1.2	510 ± 33
	blend	2 lines (b)	3485.95	0.94	36.4 ± 3.5	552 ± 59
	$\nu_1 + \nu_3 - \nu_1$	3_{21}–4_{22} (p)	3485.31	0.91	31.3 ± 4.0	493 ± 68
	blend	2 lines (b)	3392.55	1.50	51.6 ± 3.9	470 ± 43
	blend	3 lines (b)	3390.05	0.34	13.3 ± 0.3	531 ± 29
	$2\nu_1 + \nu_3 - 2\nu_1$	0_{00}–1_{01} (o)	3388.77	0.26	13.1 ± 0.2	680 ± 36
	$\nu_1 + \nu_3 - \nu_3$	4_{04}–5_{15} (o)	3387.54	0.30	9.61 ± 0.27	438 ± 25
	$\nu_1 + \nu_3 - \nu_3$	2_{11}–3_{22} (o)	3385.14	0.24	9.56 ± 0.86	554 ± 57
	ν_1	4_{31}–5_{50} (o)	3384.39	0.29	11.6 ± 0.8	548 ± 47
	blend	2 lines (b)	3383.1	0.13	7.13 ± 0.38	728 ± 53
	$2\nu_1 - \nu_3$	2_{12}–3_{13} (o)	3382.10	1.55	69.9 ± 0.3	619 ± 31
	$\nu_2 + \nu_3 - \nu_2$	4_{23}–5_{42} (p)	3381.70	0.04	1.77 ± 0.24	574 ± 81
	$2\nu_1 - \nu_3$	2_{02}–3_{03} (p)	3378.48	0.47	21.7 ± 0.3	638 ± 33
	$2\nu_1 - \nu_3$	3_{03}–3_{22} (o)	3376.89	0.05	2.85 ± 0.27	822 ± 88
	ν_1	5_{15}–6_{24} (p)	3374.68	0.11	7.91 ± 0.29	982 ± 61
	$2\nu_1 - \nu_1$	3_{21}–4_{23} (o)	3374.40	0.20	7.27 ± 0.49	490 ± 41
	$2\nu_1 - \nu_3$	2_{21}–3_{22} (o)	3372.75	0.85	36.5 ± 0.2	592 ± 30
	$2\nu_1 - \nu_1$	3_{13}–4_{22} (p)	3371.69	0.13	5.18 ± 0.32	566 ± 45
	ν_1	4_{04}–5_{33} (p)	3371.05	0.14	5.71 ± 0.27	574 ± 40
	$2\nu_1 - \nu_3 - 2\nu_1$	1_{11}–2_{12} (o)	3369.73	0.23	9.82 ± 0.41	599 ± 39
	blend	4 lines (b)	3368.7	0.19	8.48 ± 0.54	599 ± 49
	ν_1	5_{41}–6_{52} (o)	3367.64	0.07	6.10 ± 0.87	1271 ± 193
	blend	2 lines (p)	3362.3	0.28	9.52 ± 1.51	473 ± 79
	ν_1	6_{34}–7_{43} (o)	3361.67	0.07	5.71 ± 0.62	1085 ± 129
	blend	2 lines (b)	3361.0	0.36	16.0 ± 0.4	613 ± 34
	blend	2 lines (p)	3359.45	0.14	5.48 ± 0.40	535 ± 47
	$2\nu_1 - \nu_3$	3_{03}–4_{04} (o)	3358.92	0.85	37.9 ± 0.3	613 ± 31
	ν_1	6_{25}–7_{34} (o)	3357.03	0.09	6.00 ± 0.58	894 ± 97
	$\nu3$	5_{33}–6_{52} (o)	3355.71	0.11	5.32 ± 0.66	685 ± 92
	blend	2 lines (b)	3355.45	0.24	10.7 ± 0.4	611 ± 39
	blend	2 lines (o)	3351.3	0.02	2.19 ± 0.29	1277 ± 181
	blend	2 lines (b)	3349.4	0.10	4.49 ± 0.26	639 ± 48
	blend	2 lines (p)	3348.4	0.17	9.56 ± 0.34	763 ± 47
	blend	3 lines (b)	3347.9	0.40	14.1 ± 0.3	491 ± 26
CH$_3$OH (82 ± 5 K)	ν_2	13 lines	3001.1	20.9	23.6 ± 0.3	17.4 ± 0.9
		16 lines	2997.15	30.2	21.6 ± 0.3	11.1 ± 0.6
		8 lines	2996.4	12.2	15.8 ± 0.3	20.0 ± 1.1
		12 lines	2990.1	7.10	7.02 ± 0.26	15.3 ± 1.0
		7 lines	2989.8	3.21	4.02 ± 0.39	19.4 ± 2.1
		28 lines	2981.9	35.9	27.8 ± 0.3	12.0 ± 0.6
		6 lines	2974.5	6.17	3.84 ± 0.30	9.73 ± 0.89
		18 lines	2973.0	17.0	16.6 ± 0.4	15.3 ± 0.8
		18 lines	2972.55	12.9	11.5 ± 0.3	13.9 ± 0.8
	ν_3	4 lines	2863.9	3.81	2.59 ± 0.26	11.1 ± 1.3
		7 lines	2863.2	3.26	3.02 ± 0.25	15.1 ± 1.5
		6 lines	2862.3	5.55	4.75 ± 0.25	14.0 ± 1.0
		4 lines	2861.4	3.05	3.16 ± 0.27	17.0 ± 1.7

Table A2

(Continued)

Molecule	Band ID	Line ID[a]	Line Pos. (cm^{-1})[b]	g-factor (10^{-7} s^{-1})[c]	Line Flux (10^{-19} W m^{-2})[d]	Q (10^{27} s^{-1})[e]
		7 lines	2861.2	8.01	5.01 ± 0.30	10.3 ± 0.8
		10 lines	2860.7	14.8	6.49 ± 0.27	7.18 ± 0.47
		10 lines	2860.4	10.2	9.90 ± 0.30	15.9 ± 0.9
		9 lines	2859.7	10.9	11.8 ± 0.4	17.8 ± 1.0
		10 lines	2859.1	15.5	9.28 ± 0.31	9.78 ± 0.59
		5 lines	2858.2	7.78	7.31 ± 0.32	15.4 ± 1.0
		4 lines	2857.9	8.83	1.91 ± 0.24	3.55 ± 0.47
		14 lines	2857.4	25.4	15.8 ± 0.4	10.2 ± 0.6
		4 lines	2857.1	9.46	6.47 ± 0.25	11.2 ± 0.7
		9 lines	2856.7	19.1	12.3 ± 0.4	10.6 ± 0.6
		4 lines	2855.5	9.58	9.52 ± 0.29	16.3 ± 1.0
		10 lines	2855.2	24.4	16.8 ± 0.4	11.3 ± 0.6
		4 lines	2854.65	8.97	2.99 ± 0.32	5.48 ± 0.64
		6 lines	2852.7	13.1	10.1 ± 0.3	12.7 ± 0.8
		3 lines	2852.3	11.6	8.56 ± 0.28	12.1 ± 0.7
		2 lines	2851.11	9.48	8.79 ± 0.32	15.2 ± 0.9
		2 lines	2850.13	3.86	2.81 ± 0.25	12.0 ± 1.2
		2 lines	2849.51	7.77	7.45 ± 0.30	15.8 ± 1.0
		7 lines	2849.0	14.9	8.97 ± 0.42	9.87 ± 0.68
		2 lines	2847.5	3.95	2.45 ± 0.33	10.2 ± 1.5
		3 lines	2846.3	3.02	2.43 ± 0.27	13.3 ± 1.6
		many	2845.8	26.6	19.1 ± 0.5	11.8 ± 0.7
		many	2844.1	120	82.1 ± 0.6	11.3 ± 0.6
		17 lines	2843.4	3.05	2.69 ± 0.33	14.6 ± 1.9
		11 lines	2843.05	4.81	5.99 ± 0.31	20.5 ± 1.5
		14 lines	2842.0	23.0	15.8 ± 0.4	11.3 ± 0.6
		5 lines	2841.1	7.78	6.36 ± 0.31	13.5 ± 0.9
		2 lines	2839.84	8.55	6.75 ± 0.28	13.0 ± 0.8
		2 lines	2838.76	3.09	2.04 ± 0.31	10.9 ± 1.8
		2 lines	2838.22	10.2	8.19 ± 0.27	13.2 ± 0.8
		5 lines	2837.8	18.2	8.84 ± 0.34	8.01 ± 0.51
		6 lines	2836.5	14.8	9.62 ± 0.33	10.7 ± 0.6
		3 lines	2836.25	14.1	7.37 ± 0.32	8.67 ± 0.58
		7 lines	2835.8	22.6	12.6 ± 0.4	9.20 ± 0.55
		3 lines	2835.5	6.90	4.78 ± 0.49	11.5 ± 1.3
C_2H_6 (92^{+8}/$_{-7}$ K)	ν_7	$^RQ_4$	3000.29	116	38.4 ± 0.3	5.13 ± 0.26
		$^rR_2(2)$	2997.45	49.4	14.3 ± 0.3	4.51 ± 0.24
		$^RQ_2$	2993.47	238	71.8 ± 0.3	4.69 ± 0.24
		$^RQ_1$	2990.07	281	81.1 ± 0.4	4.50 ± 0.23
		$^RQ_0$	2986.72	358	112±1	4.87 ± 0.24
		$^PQ_1$	2983.38	284	76.6 ± 0.3	4.22 ± 0.21
		$^PQ_2$	2980.07	237	63.9 ± 0.3	4.22 ± 0.21
		$^PQ_3$	2976.78	215	51.4 ± 0.3	3.75 ± 0.19
		5 lines	2974.8	40.2	10.7 ± 0.4	4.16 ± 0.25
		6 lines	2972.78	38.8	11.3 ± 0.2	4.58 ± 0.25
		12 lines	2970.15	42.3	12.1 ± 0.2	4.48 ± 0.24
		6 lines	2968.2	40.8	12.4 ± 0.4	4.77 ± 0.28
		many	2966.8	71.3	16.3 ± 0.4	3.60 ± 0.20
		many	2964.25	53.3	12.4 ± 0.3	3.66 ± 0.20
CH_4 (94 ± 4 K)	ν_3	R7	3095.1	29.7	8.85 ± 1.93	4.39 ± 0.98
		P2	2999.03	95.6	28.8 ± 0.3	4.55 ± 0.23
		P3	2988.80	101	29.4 ± 0.9	4.43 ± 0.26
		P4	2978.65	43.7	13.4 ± 0.5	4.66 ± 0.30
		P5	2968.44	41.3	12.0 ± 0.6	4.46 ± 0.32
NH_3 (90 K)	blend	2 lines	3391.38	8.50	1.01 ± 0.27	1.99 ± 0.54
		apP(4,4)	3390.92	4.96	0.19 ± 0.25	0.65 ± 0.84
		3 lines	3382.4	6.02	1.53 ± 0.24	4.26 ± 0.71
		3 lines	3376.3	21.2	4.38 ± 0.29	3.46 ± 0.29
		2 lines	3355.0	10.5	1.35 ± 0.38	2.17 ± 0.62
	ν_3	2 lines	3256.7	8.70	2.50 ± 0.34	4.11 ± 0.60
H_2CO(110 K)	ν_5	4 lines	2873.0	13.5	2.03 ± 0.32	2.64 ± 0.43
		4 lines	2867.8	42.9	3.07 ± 0.36	1.26 ± 0.16
		3_{12}-3_{03}	2851.81	14.7	2.64 ± 0.26	3.19 ± 0.35
C_2H_2 (90 K)	$\nu_2 + \nu_4 - \nu_5$	P9	3260.43	95.8	2.23 ± 0.58	0.30 ± 0.08

Table A2
(Continued)

Molecule	Band ID	Line ID[a]	Line Pos. (cm^{-1})[b]	g-factor (10^{-7} s^{-1})[c]	Line Flux (10^{-19} W m^{-2})[d]	Q (10^{27} s^{-1})[e]
	$\nu_2 + \nu_4 - \nu_5$	P11	3255.56	58.9	3.46 ± 0.30	0.76 ± 0.08
C_2H_4 (100 K)	blend	5 lines	3130	9.52	1.35 ± 0.30	2.09 ± 0.48
		9 lines	3120.4	13.4	1.17 ± 0.61	1.30 ± 0.68
		9 lines	3118	11.2	1.19 ± 0.78	1.57 ± 1.03
		7 lines	3111.6	6.51	0.81 ± 0.48	1.85 ± 1.10
		3 lines	3109	11.3	-0.33 ± 0.39	-0.44 ± 0.51
		14 lines	3099	19.4	3.73 ± 0.99	2.87 ± 0.77
		17 lines	3094.5	43.7	5.86 ± 1.54	1.99 ± 0.54
		5 lines	3091.6	10.9	1.15 ± 0.35	1.57 ± 0.49
NH_2 (100 K)	blend	3 lines	3358.23	18.3	1.62 ± 0.26	
	ν_1	3 lines	3263.3	36.5	1.96 ± 0.29	
		3 lines	3250.4	157	9.56 ± 0.28	
		$2_{20}-2_{11}$	3249.95	79.7	3.34 ± 0.29	
		3 lines	3249.1	44.4	2.80 ± 0.26	
		2 lines	3248.6	63.6	2.39 ± 0.21	
		$2_{02}-1_{11}$	3248.42	31.1	1.78 ± 0.21	
		2 lines	3247.4	33.1	1.39 ± 0.25	
		4 lines	3239.5	226	11.2 ± 0.4	
		4 lines	3234.2	78.2	6.49 ± 0.52	
		2 lines	3124.22	83.2	1.79 ± 0.36	
OH	$1 \rightarrow 0$	P1.5 2$-$/2+	3507.8		48.3 ± 0.6	
		P2.5 1+	3484.74		39.1 ± 0.8	
		P4.5 2$-$	3378.07		13.7 ± 0.3	
		P7.5 2+	3241.52		10.6 ± 0.3	
		P7.5 2$-$	3241.02		13.1 ± 0.4	
		P8.5 1+	3235.65		12.6 ± 0.3	
		P8.5 1$-$	3234.84		14.4 ± 0.3	
		P11.5 1$-$	3093.71		13.3 ± 0.6	
		P11.5 1+	3092.60		11.0 ± 0.3	
		P13.5 1$-$	2994.26		11.9 ± 0.4	
		P15.5 2+	2840.82		10.8 ± 0.3	
	$2 \rightarrow 1$	P3.5 2+/2$-$	3262.1		9.46 ± 0.26	
		P4.5 1+	3248.13		5.10 ± 0.22	
		P6.5 2+	3132.23		3.70 ± 0.52	
		P7.5 1+	3124.66		5.99 ± 0.33	
		P12.5 2+	2849.87		3.01 ± 0.25	
		P13.5 1$-$	2848.10		3.95 ± 0.37	

Notes.
[a] H_2O line identifications indicate emissions that are ortho (o), para (p), or a blend of both (b).
[b] Rest positions for single lines or average rest positions for multiple lines.
[c] The g-factors at $R_h = 1$ au for the derived or assumed rotational temperature given below the molecular assignment in parentheses.
[d] Line fluxes within a 3 spectral $\times$ 9 spatial pixel extract ($0\rlap{.}''432 \times 1\rlap{.}''71$) centered on the peak intensity of the gas spatial profile.
[e] Derived production rates for individual lines corrected for slit losses. Uncertainties include photon noise (reflected in the S/N of individual lines) and an assumed 5% uncertainty per emission in the continuum baseline fit. Calibration and growth factor uncertainties are not included.

Table A3
Line Positions, Fluxes, and Production Rates in C/2014 Q2 (Lovejoy) on UT 2015 February 2 Setting KL2

Molecule	Band ID	Line ID[a]	Line Pos. (cm^{-1})[b]	g-factor (10^{-7} s^{-1})[c]	Line Flux (10^{-19} W m^{-2})[d]	Q (10^{27} s^{-1})[e]
H_2O (88 ± 3 K)	blend	3 lines (b)	3440.7	0.11	4.70 ± 0.69	589 ± 91
	blend	3 lines (p)	3439.85	0.52	22.3 ± 0.2	600 ± 31
	$\nu_1 + \nu_3 - \nu_3$	1_{01}–2_{12} (p)	3439.42	0.27	8.27 ± 0.18	435 ± 24
	blend	2 lines (p)	3438.17	0.11	4.04 ± 0.46	533 ± 66
	blend	2 lines (o)	3436.64	0.15	3.46 ± 0.28	317 ± 30
	blend	2 lines (b)	3435.4	0.18	12.2 ± 0.2	928 ± 48
	$\nu_1 + \nu_3 - 2\nu_1$	1_{01}–0_{00} (p)	3434.96	0.05	1.52 ± 0.13	470 ± 46
	blend	4 lines (p)	3434.36	0.41	16.6 ± 0.2	565 ± 29
	ν_1	6_{24}–7_{35} (p)	3432.83	0.04	1.77 ± 0.37	676 ± 144
	ν_1	4_{14}–5_{23} (o)	3431.06	1.30	49.6 ± 1.0	535 ± 29
	$\nu_1 + \nu_3 - \nu_1$	7_{17}–8_{18} (o)	3428.60	0.05	3.47 ± 0.44	1000 ± 136
	blend	3 lines (b)	3427.9	0.37	10.6 ± 0.4	399 ± 25
	blend	2 lines (b)	3426.57	0.15	6.14 ± 0.24	559 ± 35
	$2\nu_1 + \nu_2 - \nu_2 - \nu_3$	2_{21}–2_{20} (o)	3426.18	0.04	1.65 ± 0.13	553 ± 51
	$2\nu_1 + \nu_3 - 2\nu_1$	2_{11}–2_{12} (o)	3425.39	0.06	1.84 ± 0.15	409 ± 38
	blend	2 lines (p)	3421.74	0.73	25.7 ± 0.2	499 ± 35
	$2\nu_1 - \nu_1$	5_{05}–6_{16} (o)	3419.14	0.09	4.07 ± 0.36	637 ± 64
	blend	2 lines (o)	3417.7	0.32	13.5 ± 0.2	597 ± 31
	blend	2 lines (p)	3415.75	0.24	11.1 ± 0.2	655 ± 34
	blend	3 lines (o)	3413.0	0.66	26.5 ± 0.2	565 ± 29
	$\nu_1 + \nu_3 - \nu_3$	3_{13}–4_{04} (o)	3411.61	0.53	20.2 ± 0.1	539 ± 27
	$\nu_1 + \nu_2 - \nu_2$	4_{23}–5_{32} (o)	3411.17	0.04	1.86 ± 0.10	716 ± 52
	$\nu_1 + \nu_3 - \nu_1$	2 lines (o)	3410.65	0.05	2.93 ± 0.14	807 ± 55
	$\nu_1 + \nu_2 - \nu_2$	3_{31}–4_{40} (p)	3409.64	0.05	1.60 ± 0.14	438 ± 44
	blend	2 lines (o)	3408.9	0.59	24.1 ± 0.2	582 ± 30
	$\nu_1 + \nu_3 - \nu_1$	2 lines (b)	3406.42	0.05	1.97 ± 0.10	530 ± 38
	$2\nu_1 + \nu_3 - 2\nu_1$	2 lines (b)	3405.41	0.27	17.0 ± 0.2	903 ± 46
	$\nu_1 + \nu_3 - \nu_3$	3_{03}–4_{14} (p)	3405.00	0.13	3.93 ± 0.13	433 ± 26
	$\nu_1 + \nu_3 - \nu_3$	1_{10}–2_{21} (p)	3404.24	0.23	13.6 ± 0.2	834 ± 90
	ν_1	5_{24}–6_{33} (p)	3403.58	0.17	7.41 ± 0.26	611 ± 37
	$2\nu_1 - \nu_3$	1_{11}–2_{12} (p)	3403.23	0.50	21.6 ± 0.2	616 ± 31
	blend	2 lines (o)	3399.84	0.06	4.55 ± 0.13	1100 ± 64
	blend	2 lines (o)	3399.34	1.79	73.7 ± 0.2	586 ± 29
	ν_1	5_{32}–6_{43} (o)	3397.21	0.59	11.2 ± 0.1	269 ± 28
	$2\nu_1 - \nu_1$	2_{20}–3_{31} (p)	3396.41	0.18	3.58 ± 0.26	285 ± 25
	$2\nu_1 - \nu_1$	2_{21}–3_{30} (o)	3394.08	1.32	44.7 ± 0.2	482 ± 24
	blend	2 lines (b)	3392.55	1.51	32.8 ± 0.2	309 ± 26
	$2\nu_1 - \nu_3$	6_{16}–7_{17} (o)	3299.18	0.03	1.86 ± 0.15	910 ± 87
	$2\nu_1 - \nu_3$	6_{06}–7_{07} (p)	3298.93	0.01	0.89 ± 0.17	1327 ± 260
	$\nu_1 + \nu_3 - \nu_3$	4_{23}–5_{32} (p)	3288.41	0.04	2.21 ± 0.30	848 ± 121
	$2\nu_1 - \nu_3$	5_{23}–6_{24} (o)	3281.95	0.02	0.99 ± 0.13	966 ± 139
	blend	3 lines (b)	3278.63	0.03	2.10 ± 0.19	1168 ± 122
	blend	3 lines (b)	3267.35	0.06	3.03 ± 0.17	761 ± 58
CH_3OH ($70^{+15}/_{-10}$ K)	ν_2	13 lines	3037.8	4.24	1.49 ± 0.17	5.34 ± 0.66
		4 lines	3033.45	2.63	2.15 ± 0.26	12.5 ± 1.6
		3 lines	3032.85	5.42	3.39 ± 0.41	9.54 ± 1.25
		6 lines	3029.5	6.15	2.06 ± 0.27	5.12 ± 0.71
		7 lines	3027.35	3.96	2.89 ± 0.18	11.1 ± 0.9
		9 lines	3026.65	5.41	2.34 ± 0.28	6.62 ± 0.86
		14 lines	3024.2	7.80	5.13 ± 0.21	10.1 ± 0.7
		24 lines	3023.3	20.2	12.4 ± 0.3	9.41 ± 0.51
	unassigned		2913.50		8.94 ± 0.16	
			2912.48		3.72 ± 0.14	
			2910.07		11.7 ± 0.3	
			2909.51		3.32 ± 0.17	
			2908.14		9.33 ± 0.24	
			2906.64		5.68 ± 0.46	
			2905.33		2.94 ± 0.18	
			2903.81		1.20 ± 0.16	
			2902.46		6.31 ± 0.16	
			2902.13		7.70 ± 0.35	
			2901.85		4.46 ± 0.47	
			2900.84		7.07 ± 0.20	
			2899.23		1.08 ± 0.14	

Table A3

(Continued)

Molecule	Band ID	Line ID[a]	Line Pos. (cm^{-1})[b]	g-factor (10^{-7} s^{-1})[c]	Line Flux (10^{-19} W m^{-2})[d]	Q (10^{27} s^{-1})[e]
			2897.99		2.62 ± 0.16	
			2892.88		12.9 ± 0.2	
			2892.12		3.28 ± 0.15	
			2891.00		1.06 ± 0.13	
			2886.62		1.77 ± 0.14	
			2886.32		1.70 ± 0.18	
			2883.54		2.63 ± 0.10	
C$_2$H$_6$ (95 ± 7 K)	ν_5	14 lines	2910.6	53.8	15.7 ± 0.2	4.85 ± 0.25
		12 lines	2909.0	47.4	17.8 ± 0.2	6.25 ± 0.32
		20 lines	2907.3	70.2	17.1 ± 0.3	4.06 ± 0.22
		18 lines	2905.8	56.5	15.0 ± 0.2	4.43 ± 0.23
		16 lines	2904.3	57.1	20.9 ± 0.3	6.11 ± 0.32
		12 lines	2902.75	40.5	11.1 ± 0.2	4.58 ± 0.24
		10 lines	2901.2	34.8	6.23 ± 0.17	2.99 ± 0.17
		7 lines	2898.45	11.4	2.42 ± 0.16	3.54 ± 0.29
		19 lines	2896.5	15.5	5.32 ± 0.48	5.73 ± 0.59
		many lines	2896.0	96.6	22.8 ± 0.4	3.85 ± 0.21
		many lines	2895.1	73.1	10.5 ± 0.3	2.40 ± 0.14
		12 lines	2894.4	11.8	3.96 ± 0.17	5.63 ± 0.37
		4 lines	2891.78	16.5	4.77 ± 0.14	4.82 ± 0.28
		10 lines	2890.5	29.3	4.31 ± 0.19	2.46 ± 0.16
		10 lines	2889.3	43.5	8.86 ± 0.15	3.42 ± 0.18
		12 lines	2888.0	48.3	10.6 ± 0.2	3.69 ± 0.20
		12 lines	2886.95	58.6	13.9 ± 0.2	3.98 ± 0.21
		16 lines	2885.9	54.6	10.2 ± 0.2	3.14 ± 0.17
		6 lines	2884.79	38.3	9.11 ± 0.30	3.99 ± 0.24
		4 lines	2884.07	11.4	2.27 ± 0.13	3.36 ± 0.26
		10 lines	2883.8	41.5	7.62 ± 0.21	3.08 ± 0.18
		10 lines	2882.75	42.5	8.38 ± 0.17	3.31 ± 0.18
		8 lines	2881.95	12.6	3.51 ± 0.14	4.66 ± 0.30
		8 lines	2881.65	24.6	5.57 ± 0.13	3.81 ± 0.21
		6 lines	2880.88	12.6	2.17 ± 0.13	2.89 ± 0.23
		12 lines	2880.65	28.2	4.37 ± 0.15	2.60 ± 0.16
		8 lines	2879.65	17.8	3.59 ± 0.16	3.40 ± 0.23
		9 lines	2879.05	7.21	1.69 ± 0.16	3.94 ± 0.42
		8 lines	2877.7	13.6	3.43 ± 0.15	4.24 ± 0.28
		9 lines	2877.15	6.27	1.27 ± 0.13	3.41 ± 0.39
CH$_4$ (91 K)	ν_3	R1	3038.50	147	36.7 ± 0.2	4.61 ± 0.23
		R0	3028.75	170	40.2 ± 0.2	4.37 ± 0.22
NH$_3$ (90 K)	ν_3	srQ(3,0)	3437.37	4.76	0.83 ± 0.13	3.54 ± 0.59
	blend	5 lines	3415.1	15.4	3.64 ± 0.19	4.80 ± 0.34
	blend	2 lines	3400.7	3.52	1.51 ± 0.12	8.77 ± 0.84
	ν_1	2 lines	3395.65	8.69	1.10 ± 0.14	2.58 ± 0.36
		2 lines	3295.4	22.3	3.73 ± 0.17	3.96 ± 0.27
		2 lines	3275.3	11.0	2.30 ± 0.31	4.97 ± 0.71
HCN (92^{+5}/$_{-4}$ K)	ν_3	P2	3305.54	147	9.80 ± 0.14	0.97 ± 0.05
		P3	3302.55	202	13.1 ± 0.2	0.94 ± 0.05
		P4	3299.53	235	17.0 ± 0.2	1.05 ± 0.05
		P5	3296.49	247	20.5 ± 0.5	1.21 ± 0.07
		P7	3290.35	213	13.0 ± 0.2	0.89 ± 0.05
		P8	3287.25	178	11.5 ± 0.2	0.93 ± 0.05
		P11	3277.83	74.4	5.39 ± 0.20	1.06 ± 0.07
C$_2$H$_2$ (90 $^{+11}$/$_{-9}$ K)	$\nu_2 + \nu_4 - \nu_5$	R9	3304.97	74.8	2.21 ± 0.14	0.73 ± 0.06
	ν_3	R3	3304.17	139	2.80 ± 0.17	0.50 ± 0.04
	$\nu_2 + \nu_4 - \nu_5$	R7	3300.42	118	2.41 ± 0.25	0.50 ± 0.06
		R3	3291.23	150	3.54 ± 0.26	0.58 ± 0.05
	ν_3	P4	3285.38	54.7	1.54 ± 0.26	0.70 ± 0.12
		P5	3282.99	175	5.90 ± 0.21	0.83 ± 0.05
		P7	3278.19	166	5.45 ± 0.17	0.81 ± 0.05
		P8	3275.77	48.8	1.54 ± 0.28	0.78 ± 0.15
	$\nu_2 + \nu_4 - \nu_5$	P3	3274.81	146	3.68 ± 0.44	0.62 ± 0.08
	ν_3	P9	3273.35	123	2.89 ± 0.46	0.59 ± 0.10
	$\nu_2 + \nu_4 - \nu_5$	P5	3270.05	189	5.96 ± 0.14	0.78 ± 0.04
		P6	3267.66	63.7	2.03 ± 0.17	0.79 ± 0.08

Table A3
(Continued)

Molecule	Band ID	Line ID[a]	Line Pos. (cm^{-1})[b]	g-factor (10^{-7} s^{-1})[c]	Line Flux (10^{-19} W m^{-2})[d]	Q (10^{27} s^{-1})[e]
H_2CO (103 $^{+5}/_{-4}$ K)	blend	14 lines	2782.1	117	4.47 ± 0.28	1.84 ± 0.15
	ν_1	13 lines	2780.95	139	6.24 ± 0.18	2.17 ± 0.13
	blend	18 lines	2779.9	47.2	1.41 ± 0.19	1.44 ± 0.20
	ν_1	10 lines	2778.45	27.4	1.03 ± 0.16	1.82 ± 0.29
		$1_{10}-2_{11}$	2777.28	20.8	0.50 ± 0.16	1.15 ± 0.37
		2 lines	2775.2	49.5	1.32 ± 0.15	1.28 ± 0.16
	blend	4 lines	2774.75	49.9	1.46 ± 0.15	1.41 ± 0.16
	blend	5 lines	2772.8	65.4	1.77 ± 0.23	1.30 ± 0.18
	blend	5 lines	2772.2	73.3	1.97 ± 0.22	1.30 ± 0.16
	blend	4 lines	2771.35	22.2	0.68 ± 0.17	1.47 ± 0.38
	ν_1	$4_{14}-5_{15}$	2770.55	50.2	1.07 ± 0.16	1.03 ± 0.16
	blend	7 lines	2769.75	83.2	2.25 ± 0.19	1.31 ± 0.13
	ν_1	$5_{15}-6_{16}$	2768.20	51.8	1.27 ± 0.15	1.18 ± 0.15
		3 lines	2768.0	20.1	0.88 ± 0.16	2.12 ± 0.39
		4 lines	2767.3	72.3	2.81 ± 0.19	1.88 ± 0.16
	ν_5	12 lines	2766.8	33.7	1.02 ± 0.21	1.46 ± 0.31
	blend	10 lines	2766.4	38.7	0.96 ± 0.15	1.20 ± 0.20
	ν_1	4 lines	2765.7	70.8	2.82 ± 0.22	1.93 ± 0.18
		5 lines	2764.85	74.4	2.31 ± 0.27	1.51 ± 0.19
		2 lines	2763.5	50.0	1.82 ± 0.15	1.76 ± 0.17
		7 lines	2762.4	68.1	2.18 ± 0.21	1.55 ± 0.17
		4 lines	2761.49	34.0	0.81 ± 0.16	1.15 ± 0.23
		2 lines	2761.15	41.1	1.67 ± 0.16	1.97 ± 0.21
		4 lines	2759.84	46.7	1.60 ± 0.16	1.66 ± 0.18
		6 lines	2759.0	65.3	2.12 ± 0.24	1.58 ± 0.19
		4 lines	2757.38	38.6	0.67 ± 0.18	0.85 ± 0.23
		4 lines	2756.5	51.3	1.27 ± 0.19	1.20 ± 0.19
	blend	8 lines	2754.85	54.5	1.54 ± 0.20	1.37 ± 0.19
	ν_1	6 lines	2754.1	43.1	1.18 ± 0.19	1.33 ± 0.22
	blend	8 lines	2752.4	47.6	1.29 ± 0.20	1.32 ± 0.22
NH_2 (100 K)	ν_1	$2_{20}-1_{11}$	3301.99	42.1	2.50 ± 0.14	
		$2_{20}-1_{11}$	3301.71	81.9	4.80 ± 0.15	
		3 lines	3286.8	71.0	2.30 ± 0.15	
		6 lines	3279.75	140	5.21 ± 0.24	
		2 lines	3269.8	45.5	1.31 ± 0.14	
		3 lines	3268.7	36.8	1.12 ± 0.13	
		3 lines	3266.2	51.5	3.07 ± 0.20	
		3 lines	3263.2	70.1	1.96 ± 0.20	
		3 lines	3170.8	79.2	3.17 ± 0.14	
		3 lines	3168.0	40.4	1.64 ± 0.22	
		3 lines	3166.5	56.4	2.68 ± 0.24	
		3 lines	3163.95	33.7	1.77 ± 0.12	
		$3_{13}-3_{22}$	3162.63	19.9	1.10 ± 0.11	
		$4_{22}-4_{31}$	3159.24	15.9	0.49 ± 0.11	
		$4_{22}-4_{31}$	3158.90	16.0	0.56 ± 0.10	
		4 lines	3155.6	239	7.38 ± 0.14	
		4 lines	3151.15	54.3	1.18 ± 0.14	
		$3_{22}-3_{31}$	3150.29	14.8	0.76 ± 0.11	
		$1_{10}-2_{21}$	3139.76	34.5	2.09 ± 0.12	
		2 lines	3040.04	32.2	1.74 ± 0.14	
OH	$1 \rightarrow 0$	P4.5 1+	3407.99		25.0 ± 0.1	
		P4.5 1−	3407.61		31.4 ± 0.1	
		P6.5 2+	3287.47		13.3 ± 0.2	
		P7.5 1+	3280.04		16.3 ± 0.4	
		P9.5 2−	3145.49		9.85 ± 0.11	
		P10.5 1+	3142.06		13.8 ± 0.1	
		P10.5 1−	3141.04		11.4 ± 0.3	
		P12.5 1+	3044.43		16.7 ± 0.2	
		P12.5 1−	3043.21		10.7 ± 0.2	
		P14.5 2−	2893.53		10.5 ± 0.2	
		P14.5 2+	2892.38		4.52 ± 0.14	
		P15.5 1−	2891.51		13.1 ± 0.2	
		P15.5 1+	2890.00		6.38 ± 0.14	
	$2 \rightarrow 1$	P2.5 2+/2−	3303.81		6.26 ± 0.38	

Table A3
(Continued)

Molecule	Band ID	Line ID[a]	Line Pos. (cm^{-1})[b]	g-factor (10^{-7} s^{-1})[c]	Line Flux (10^{-19} W m^{-2})[d]	Q (10^{27} s^{-1})[e]
		P3.5 1+/1−	3285.9		14.5 ± 0.2	
		P3.5 2+/2−	3262.1		8.04 ± 0.15	
		P5.5 2+	3176.59		4.13 ± 0.15	
		P5.5 2−	3176.32		4.20 ± 0.15	
		P6.5 1+	3167.67		3.20 ± 0.19	
		P6.5 1−	3167.07		7.39 ± 0.35	
		P6.5 2−	3132.61		3.69 ± 0.35	
		P6.5 2+	3132.23		3.16 ± 0.28	
		P8.5 2−	3042.07		4.42 ± 0.14	
		P8.5 2+	3041.51		6.02 ± 0.15	
		P9.5 1−	3037.05		4.44 ± 0.17	
		P11.5 2−	2899.04		1.83 ± 0.19	
		P14.5 2−	2750.59		3.12 ± 0.16	
		P15.5 1−	2748.47		3.99 ± 0.17	
		P15.5 1+	2747.02		1.95 ± 0.16	
	$3 \rightarrow 2$	P2.5 1+/1−	3161.4		1.97 ± 0.13	
		P2.5 2+/2−	3144.22		2.09 ± 0.12	

Notes.
[a] H_2O line identifications indicate emissions that are ortho (o), para (p), or a blend of both (b).
[b] Rest positions for single lines or average rest positions for multiple lines.
[c] The g-factors at $R_h = 1$ au for the derived or assumed rotational temperature given below the molecular assignment in parentheses.
[d] Line fluxes within a 3 spectral × 9 spatial pixel extract ($0\farcs432 \times 1\farcs71$) centered on the peak intensity of the gas spatial profile.
[e] Derived production rates for individual lines corrected for slit losses. Uncertainties include photon noise (reflected in the S/N of individual lines) and an assumed 5% uncertainty per emission in the continuum baseline fit. Calibration and growth factor uncertainties are not included.

Table A4
Line Positions, Fluxes, and Production Rates in C/2014 Q2 (Lovejoy) on UT 2015 February 2 Setting M1

Molecule	Band ID	Line ID[a]	Line Pos. (cm^{-1})[b]	g-factor (10^{-7} s^{-1})[c]	Line Flux (10^{-19} W m^{-2})[d]	Q (10^{27} s^{-1})[e]
H_2O (87 ± 8 K)	$\nu_1 - \nu_2$	$5_{15}-4_{04}$ (p)	2160.01	0.13	10.3 ± 1.5	1907 ± 293
	$\nu_3 - \nu_2$	$4_{22}-4_{23}$ (o)	2158.11	0.11	10.5 ± 1.5	2185 ± 338
	$\nu_2 + \nu_3 - 2\nu_2$	$2_{20}-2_{21}$ (o)	2157.51	0.34	16.6 ± 1.5	1183 ± 120
		$0_{00}-1_{01}$ (o)	2155.82	0.77	34.2 ± 1.6	1064 ± 73
	blend	2 lines (p)	2155.05	0.41	28.1 ± 2.5	1633 ± 166
	$\nu_3 - \nu_2$	$1_{11}-1_{10}$ (o)	2151.20	4.32	125 ± 3	695 ± 38
		$3_{21}-3_{22}$ (p)	2149.13	0.20	11.8 ± 1.4	1430 ± 187
	$\nu_1 - \nu_2$	$2_{21}-1_{10}$ (o)	2148.19	1.21	34.1 ± 1.5	677 ± 45
	$\nu_3 - \nu_2$	$2_{20}-2_{21}$ (o)	2144.81	2.09	57.8 ± 1.5	664 ± 37
	blend	2 lines (p)	2142.25	0.72	19.1 ± 1.4	635 ± 57
	$\nu_3 - \nu_2$	$2_{12}-2_{11}$ (p)	2139.93	0.46	7.76 ± 1.72	404 ± 92
		2 lines (o)	2137.36	5.42	165 ± 4	735 ± 42
	$\nu_2 + \nu_3 - 2\nu_2$	$1_{01}-2_{02}$ (p)	2132.91	0.38	10.4 ± 1.5	662 ± 98
CO (71 ± 10 K)	$1 \rightarrow 0$	R3	2158.30	180	109 ± 2	14.1 ± 0.7
		R2	2154.60	180	110 ± 2	14.2 ± 0.7
		R1	2150.86	149	95.0 ± 1.6	14.9 ± 0.8
		R0	2147.08	86.1	58.1 ± 1.5	15.8 ± 0.9
		P1	2139.43	92.5	45.3 ± 2.5	11.5 ± 0.9
		P2	2135.55	172	110 ± 2	15.0 ± 0.8
		P3	2131.63	224	138 ± 2	14.6 ± 0.8
		P4	2127.68	241	138 ± 4	13.6 ± 0.8

Notes.
[a] H_2O line identifications indicate emissions that are ortho (o), para (p), or a blend of both (b).
[b] Rest positions for single lines or average rest positions for multiple lines.
[c] The g-factors at $R_h = 1$ au for the derived or assumed rotational temperature given below the molecular assignment in parentheses.
[d] Line fluxes within a 3 spectral × 9 spatial pixel extract ($0\farcs432 \times 1\farcs71$) centered on the peak intensity of the gas spatial profile.
[e] Derived production rates for individual lines corrected for slit losses. Uncertainties include photon noise (reflected in the S/N of individual lines) and an assumed 5% uncertainty per emission in the continuum baseline fit. Calibration and growth factor uncertainties are not included.

Table A5
Line Positions, Fluxes, and Production Rates in C/2014 Q2 (Lovejoy) on UT 2015 Feb 3 Setting KL4

Molecule	Band ID	Line ID[a]	Line Pos. (cm^{-1})[b]	g-factor (10^{-7} s^{-1})[c]	Line Flux (10^{-19} W m^{-2})[d]	Q (10^{27} s^{-1})[e]
H$_2$O (101 ± 5 K)	blend	3 lines (b)	3472.8	0.28	8.21 ± 0.47	551 ± 42
	$\nu_1 + \nu_3 - \nu_1$	4_{23}–5_{24} (p)	3471.43	0.52	11.9 ± 2.0	438 ± 76
	blend	6 lines (b)	3468.6	2.27	83.9 ± 2.3	698 ± 40
	blend	3 lines (b)	3459.53	0.70	23.5 ± 0.6	637 ± 35
	$\nu_1 + \nu_3 - \nu_3$	0_{00}–1_{11} (o)	3458.12	0.57	25.3 ± 2.5	837 ± 92
	$\nu_1 + \nu_3 - \nu_1$	4_{22}–5_{23} (o)	3456.45	1.44	55.3 ± 4.8	727 ± 73
	blend	2 lines (o)	3455.78	0.21	7.82 ± 1.12	704 ± 107
		3_{12}–3_{21} (p)	3455.14	0.10	2.13 ± 0.33	413 ± 67
		2_{11}–2_{20} (o)	3454.69	0.51	19.7 ± 0.3	733 ± 39
	blend	2 lines (o)	3453.22	1.49	60.5 ± 0.4	772 ± 39
	blend	3 lines (b)	3450.9	0.22	6.13 ± 0.57	534 ± 57
	$2\nu_1 - \nu_3$	1_{10}–1_{11} (o)	3450.29	1.14	55.3 ± 0.7	918 ± 47
	blend	3 lines (b)	3449.72	0.18	10.4 ± 1.2	1080 ± 140
	$2\nu_1 - \nu_3$	2_{20}–2_{21} (p)	3445.89	0.37	24.1 ± 3.0	1250 ± 169
	blend	2 lines (o)	3341.6	0.32	18.4 ± 1.0	1106 ± 83
	blend	3 lines (p)	3439.85	0.46	29.8 ± 0.6	1227 ± 66
	$\nu_1 + \nu_3 - \nu_3$	1_{01}–2_{12} (p)	3439.42	0.23	10.4 ± 0.3	857 ± 52
	blend	2 lines (b)	3435.4	0.20	15.2 ± 0.2	1432 ± 74
	$2\nu_1 + \nu_3 - 2\nu_1$	1_{01}–0_{00} (p)	3434.96	0.04	1.37 ± 0.17	657 ± 86
	blend	3 lines (p)	3434.36	0.40	19.8 ± 0.4	954 ± 52
	blend	3 lines (b)	3427.9	0.52	22.3 ± 1.4	823 ± 67
	blend	2 lines (b)	3426.58	0.23	10.1 ± 0.8	834 ± 77
	blend	2_{21}–2_{20} (o)	3426.18	0.04	2.03 ± 0.16	993 ± 93
	$2\nu_1 + \nu_3 - 2\nu_1$	2_{11}–2_{12} (o)	3425.39	0.06	3.07 ± 0.25	984 ± 93
	$2\nu_1 - \nu_3$	3_{21}–4_{22} (o)	3339.12	0.24	11.7 ± 0.3	997 ± 58
	$2\nu_1 - \nu_1$	2 lines (b)	3338.1	0.09	4.77 ± 0.46	1086 ± 118
		4_{23}–5_{32} (o)	3335.42	0.32	16.4 ± 1.0	1039 ± 84
	$2\nu_1 + \nu_3 - 2\nu_1$	2_{11}–3_{12} (o)	3334.11	0.23	15.7 ± 0.3	1383 ± 76
	blend	2 lines (o)	3329.42	0.17	9.42 ± 0.38	1122 ± 72
	$2\nu_1 - \nu_3$	5_{05}–6_{06} (o)	3319.47	0.17	12.0 ± 0.3	1463 ± 80
	blend	2 lines (b)	3316.0	0.04	1.94 ± 0.26	1073 ± 155
	$2\nu_1 - \nu_3$	6_{16}–7_{17} (o)	3299.18	0.05	1.83 ± 0.21	785 ± 99
CH$_3$OH (100 K)	ν_2	6 lines	3039.47	2.93	1.37 ± 0.26	10.2 ± 2.0
		4 lines	3029.5	5.12	2.83 ± 0.37	12.2 ± 2.1
	unassigned		2939.90		2.41 ± 0.24	
			2935.19		5.80 ± 0.43	
			2934.87		2.31 ± 0.28	
			2934.48		9.98 ± 0.46	
			2933.25		4.97 ± 0.36	
			2932.82		5.32 ± 0.26	
			2932.34		5.54 ± 0.51	
			2931.97		11.0 ± 0.4	
			2931.12		4.30 ± 0.30	
			2930.82		7.77 ± 0.40	
			2929.97		6.83 ± 0.24	
			2929.60		3.84 ± 0.32	
			2929.04		13.6 ± 0.4	
			2928.65		4.51 ± 0.28	
			2925.75		3.47 ± 0.27	
			2924.39		9.25 ± 0.32	
			2923.35		10.8 ± 0.3	
			2922.88		4.42 ± 0.26	
			2921.51		12.3 ± 0.3	
			2921.08		5.30 ± 0.26	
			2920.10		15.0 ± 0.3	
			2919.77		21.4 ± 0.3	
			2919.32		18.8 ± 0.6	
			2918.52		4.27 ± 0.25	
			2914.83		5.80 ± 0.25	
			2913.47		7.74 ± 0.20	
			2911.44		7.22 ± 0.29	
			2910.09		10.4 ± 0.3	
			2909.48		2.57 ± 0.22	
			2908.03		4.63 ± 0.21	

Table A5
(Continued)

Molecule	Band ID	Line ID[a]	Line Pos. (cm^{-1})[b]	g-factor (10^{-7} s^{-1})[c]	Line Flux (10^{-19} W m^{-2})[d]	Q (10^{27} s^{-1})[e]
			2905.30		2.81 ± 0.22	
			2902.46		6.60 ± 0.23	
			2902.11		7.80 ± 0.51	
			2900.82		7.92 ± 0.27	
			2899.23		1.80 ± 0.20	
			2897.96		2.50 ± 0.20	
C$_2$H$_6$ (113 ± 17 K)	blend	7 lines	2939.6	12.5	2.00 ± 0.24	3.63 ± 0.47
	ν_5	10 lines	2915.5	29.4	8.65 ± 0.30	6.72 ± 0.41
		14 lines	2910.6	50.7	13.8 ± 0.3	6.21 ± 0.33
		14 lines	2909.1	49.0	21.7 ± 0.3	10.1 ± 0.5
		12 lines	2907.35	47.0	13.2 ± 0.3	6.42 ± 0.35
		18 lines	2905.8	49.1	11.6 ± 0.3	5.42 ± 0.30
		16 lines	2904.3	48.0	17.5 ± 0.3	8.34 ± 0.44
		12 lines	2902.75	33.3	9.94 ± 0.28	6.84 ± 0.39
		10 lines	2901.2	27.9	5.05 ± 0.22	4.15 ± 0.28
		7 lines	2898.45	9.02	2.54 ± 0.20	6.47 ± 0.59
CH$_4$ (110 ± 20 K)	ν_3	R3	3057.7	396	102±4	5.58 ± 0.35
		R2	3048.16	209	67.6 ± 0.8	7.06 ± 0.36
		R1	3038.50	117	38.1 ± 0.3	7.13 ± 0.36
		R0	3028.75	128	31.8 ± 0.4	5.44 ± 0.28
NH$_3$ (110 K)	ν_1	2 lines	3336.4	16.7	6.45 ± 0.67	11.5 ± 1.3
		2 lines	3295.4	17.9	2.92 ± 0.22	4.92 ± 0.45
HCN (97 ± 12 K)	ν_3	R9	3339.88	71.9	7.00 ± 0.33	1.98 ± 0.14
		R7	3334.37	128	7.27 ± 0.45	1.15 ± 0.09
		R6	3331.58	156	9.51 ± 0.24	1.24 ± 0.07
		R5	3328.76	180	11.8 ± 0.3	1.34 ± 0.08
		R4	3325.94	193	14.4 ± 0.3	1.52 ± 0.09
		R1	3317.33	128	9.63 ± 0.40	1.53 ± 0.10
		R0	3314.41	69.8	5.71 ± 0.68	1.67 ± 0.22
		P2	3305.54	140	8.92 ± 0.19	1.31 ± 0.07
		P3	3302.55	193	11.1 ± 0.2	1.18 ± 0.06
		P4	3299.53	227	14.4 ± 0.2	1.30 ± 0.07
		P7	3290.35	211	8.62 ± 0.27	0.84 ± 0.05
C$_2$H$_2$ (110 K)	$\nu_2 + \nu_4 - \nu_5$	R9	3304.97	87.2	1.28 ± 0.18	0.59 ± 0.09
	ν_3	R3	3304.17	121	2.20 ± 0.22	0.73 ± 0.08
H$_2$CO (122 $^{+8}/_{-7}$ K)	ν_1	2 lines	2807.6	18.3	1.45 ± 0.24	4.34 ± 0.73
	blend	3 lines	2805.17	28.9	1.29 ± 0.28	2.43 ± 0.54
	blend	4 lines	2802.4	57.8	2.96 ± 0.37	2.80 ± 0.37
	blend	4 lines	2801.36	25.1	1.78 ± 0.24	3.88 ± 0.56
	ν_1	2 lines	2800.37	27.8	2.29 ± 0.24	4.51 ± 0.52
	blend	2 lines	2796.3	41.4	2.49 ± 0.27	3.29 ± 0.39
	blend	3 lines	2795.55	28.7	1.90 ± 0.24	3.63 ± 0.49
	ν_1	5$_{14}$–4$_{13}$	2794.86	34.6	1.63 ± 0.24	2.58 ± 0.40
	blend	5 lines	2794.45	67.7	2.51 ± 0.27	2.03 ± 0.24
	ν_1	3 lines	2794.0	49.5	1.70 ± 0.25	1.88 ± 0.29
		5 lines	2793.1	26.5	1.69 ± 0.23	3.50 ± 0.51
		4$_{13}$–3$_{12}$	2792.35	31.4	1.54 ± 0.25	2.69 ± 0.46
		3 lines	2791.6	43.7	1.61 ± 0.28	2.02 ± 0.36
	blend	4 lines	2789.4	72.8	3.25 ± 0.33	2.45 ± 0.28
	blend	2 lines	2787.0	37.2	2.17 ± 0.26	3.20 ± 0.41
	blend	3 lines	2784.7	24.0	1.10 ± 0.25	2.53 ± 0.59
	ν_5	12 lines	2784.4	51.0	1.82 ± 0.30	1.96 ± 0.34
	blend	16 lines	2782.1	123	6.11 ± 0.46	2.73 ± 0.25
	ν_1	17 lines	2780.95	141	7.54 ± 0.28	2.94 ± 0.18
	blend	15 lines	2779.9	48.0	1.63 ± 0.31	1.87 ± 0.37
	ν_1	12 lines	2778.45	39.8	1.46 ± 0.27	2.02 ± 0.39
		1$_{10}$–2$_{11}$	2777.28	16.7	1.75 ± 0.24	5.78 ± 0.86
		2 lines	2775.2	40.1	0.97 ± 0.23	1.34 ± 0.32
	blend	4 lines	2774.75	44.4	2.28 ± 0.23	2.84 ± 0.32
	blend	3 lines	2772.3	50.2	1.78 ± 0.27	1.96 ± 0.31
	ν_1	4$_{14}$–5$_{15}$	2770.55	42.8	1.90 ± 0.24	2.45 ± 0.33
	blend	3 lines	2769.8	54.4	2.78 ± 0.23	2.83 ± 0.28
	ν_1	5$_{15}$–6$_{16}$	2768.20	45.6	1.87 ± 0.23	2.27 ± 0.31
		3 lines	2768.0	17.6	0.90 ± 0.24	2.83 ± 0.78

Table A5
(Continued)

Molecule	Band ID	Line ID[a]	Line Pos. (cm^{-1})[b]	g-factor (10^{-7} s^{-1})[c]	Line Flux (10^{-19} W m^{-2})[d]	Q (10^{27} s^{-1})[e]
		3 lines	2767.3	64.9	1.86 ± 0.25	1.59 ± 0.23
	blend	24 lines	2766.6	98.9	3.36 ± 0.38	1.88 ± 0.23
C_2H_4 (100 K)	ν_9	7 lines	3074	7.75	0.76 ± 0.33	2.16 ± 0.95
		20 lines	3069	13.9	2.09 ± 0.49	3.30 ± 0.79
		18 lines	3061	12.2	0.49 ± 0.62	0.89 ± 1.11
		3 lines	3054.4	3.85	-0.18 ± 0.26	-1.05 ± 1.49
NH_2 (100 K)	ν_1	$2_{20}-1_{11}$	3301.99	42.2	2.40 ± 0.16	
		$2_{20}-1_{11}$	3301.71	82.1	4.80 ± 0.16	
		$1_{01}-1_{10}$	3203.5	81.8	6.26 ± 0.36	
		$0_{00}-1_{11}$	3187.60	121	6.53 ± 0.26	
		$0_{00}-1_{11}$	3187.37	60.2	4.68 ± 0.28	
		$4_{13}-4_{22}$	3181.5	81.2	8.02 ± 0.31	
		$1_{01}-2_{12}$	3170.8	79.2	4.61 ± 0.20	
		$5_{23}-5_{32}$	3163.0	39.0	2.25 ± 0.17	
		$3_{13}-3_{22}$	3162.63	19.9	1.09 ± 0.13	
		$3_{31}-4_{40}$	3040.04	32.2	1.32 ± 0.21	
OH	$1 \rightarrow 0$	P2.5 2+/2−	3465.26		43.4 ± 0.6	
		P5.5 2+	3333.38		11.7 ± 0.3	
		P6.5 1+	3324.58		16.5 ± 0.6	
		P8.5 2−	3194.28		10.7 ± 0.2	
		P8.5 2+	3193.68		11.5 ± 0.2	
		P9.5 1−	3189.40		13.1 ± 0.2	
		P11.5 2+	3047.46		15.9 ± 0.3	
		P11.5 2−	3046.55		9.62 ± 0.22	
		P12.5 1+	3044.43		17.4 ± 0.3	
		P12.5 1−	3043.21		10.6 ± 0.2	
		P16.5 2−	2787.47		8.80 ± 0.31	
		P16.5 2+	2786.15		3.01 ± 0.26	
		P17.5 1−	2785.87		7.01 ± 0.31	
		P17.5 1+	2784.19		3.87 ± 0.26	
	$2 \rightarrow 1$	P2.5 1+/1−	3322.1		15.8 ± 0.3	
		P2.5 2+/2−	3303.81		10.8 ± 0.2	
		P5.5 2+	3176.59		5.29 ± 0.26	
		P5.5 2−	3176.32		4.97 ± 0.24	
		P6.5 1+	3167.67		4.83 ± 0.40	
		P6.5 1−	3167.07		18.6 ± 0.9	
		P8.5 2−	3042.07		4.67 ± 0.22	
		P8.5 2+	3041.51		5.06 ± 0.20	
		P9.5 1−	3037.05		4.45 ± 0.35	
	$3 \rightarrow 2$	P1.5 2+/2−	3183.5		2.17 ± 0.40	
		P2.5 1+/1−	3161.4		1.74 ± 0.14	

Notes.

[a] H_2O line identifications indicate emissions that are ortho (o), para (p), or a blend of both (b).

[b] Rest positions for single lines or average rest positions for multiple lines.

[c] The g-factors at $R_h = 1$ au for the derived or assumed rotational temperature given below the molecular assignment in parentheses.

[d] Line fluxes within a 3 spectral × 9 spatial pixel extract ($0\farcs432 \times 1\farcs71$) centered on the peak intensity of the gas spatial profile.

[e] Derived production rates for individual lines corrected for slit losses. Uncertainties include photon noise (reflected in the S/N of individual lines) and an assumed 5% uncertainty per emission in the continuum baseline fit. Calibration and growth factor uncertainties are not included.

Table A6
Line Positions, Fluxes, and Production Rates in C/2014 Q2 (Lovejoy) on UT 2015 Feb 3 Setting KL5

Molecule	Band ID	Line ID[a]	Line Pos. (cm^{-1})[b]	g-factor (10^{-7} s^{-1})[c]	Line Flux (10^{-19} W m^{-2})[d]	Q (10^{27} s^{-1})[e]
H$_2$O (82 $^{+5}/_{-4}$ K)	$\nu_1 + \nu_3 - \nu_1$	3_{13}–4_{14} (o)	3508.67	9.19	170 ± 12	395 ± 34
		3_{22}–4_{23} (o)	3494.26	2.34	62.9 ± 0.6	575 ± 29
	blend	3 lines (p)	3490.25	2.42	58.2 ± 0.5	516 ± 26
	blend	2 lines (b)	3489.7	1.18	27.1 ± 1.3	490 ± 34
	blend	3 lines (b)	3390.05	0.34	7.88 ± 0.37	519 ± 36
	$2\nu_1 + \nu_3 - 2\nu_1$	0_{00}–1_{01} (o)	3388.77	0.29	7.49 ± 0.24	574 ± 34
	$\nu_1 + \nu_3 - \nu_3$	4_{04}–5_{15} (o)	3387.54	0.27	5.22 ± 0.33	427 ± 34
	$2\nu_1 - \nu_3$	2_{12}–3_{13} (o)	3382.10	1.63	44.7 ± 0.3	610 ± 31
		2_{02}–3_{03} (p)	3378.48	0.47	12.2 ± 0.6	580 ± 39
	ν_1	5_{15}–6_{24} (p)	3374.68	0.10	4.98 ± 0.43	1162 ± 116
	$2\nu_1 - \nu_3$	2_{21}–3_{22} (o)	3372.75	0.89	23.0 ± 0.2	576 ± 29
	$2\nu_1 - \nu_1$	3_{13}–4_{22} (p)	3371.69	0.13	3.19 ± 0.45	572 ± 86
	ν_1	4_{04}–5_{33} (p)	3371.05	0.13	3.94 ± 0.36	679 ± 71
	$2\nu_1 + \nu_3 - 2\nu_1$	1_{11}–2_{12} (o)	3369.73	0.24	7.34 ± 1.00	693 ± 101
	blend	2 lines (b)	3361.0	0.36	8.59 ± 0.58	537 ± 45
	blend	2 lines (p)	3359.45	0.13	3.44 ± 0.54	614 ± 102
	$2\nu_1 - \nu_3$	3_{03}–4_{04} (o)	3358.92	0.82	24.2 ± 0.3	661 ± 34
	$\nu_1 + \nu_3 - \nu_1$	3_{13}–4_{32} (o)	3355.41	0.22	5.55 ± 0.56	575 ± 65
	blend	2 lines (b)	3349.4	0.10	3.41 ± 0.23	783 ± 66
	blend	2 lines (p)	3348.4	0.17	6.08 ± 0.44	827 ± 72
	blend	3 lines (b)	3347.9	0.36	10.0 ± 0.2	629 ± 35
	$2\nu_1 + \nu_3 - 2\nu_3$	2_{02}–3_{03} (o)	3346.99	0.40	11.2 ± 0.2	635 ± 33
	blend	2 lines (o)	3346.59	0.20	6.68 ± 0.42	761 ± 61
CH$_3$OH (69 ± 4 K)	ν_2	13 lines	3001.1	24.0	12.6 ± 0.3	14.7 ± 0.8
		15 lines	2999.85	20.0	6.39 ± 0.34	8.96 ± 0.66
		16 lines	2997.15	33.2	10.1 ± 0.3	8.55 ± 0.49
		8 lines	2996.4	12.5	7.31 ± 0.32	16.5 ± 1.1
		22 lines	2987.0	17.2	4.28 ± 0.39	7.01 ± 0.73
		28 lines	2981.9	36.6	15.2 ± 0.4	11.7 ± 0.7
		18 lines	2973.0	16.8	9.04 ± 0.61	15.2 ± 1.3
		19 lines	2972.55	13.4	6.67 ± 0.35	14.2 ± 1.0
		10 lines	2965.8	3.38	2.67 ± 0.52	22.4 ± 4.5
	ν_3	3 lines	2864.9	1.71	1.60 ± 0.27	26.1 ± 4.7
		14 lines	2862.2	15.1	4.95 ± 0.42	9.17 ± 0.90
		3 lines	2861.2	4.64	2.36 ± 0.24	14.2 ± 1.6
		9 lines	2860.7	13.4	3.73 ± 0.26	7.77 ± 0.66
		5 lines	2859.7	9.59	7.33 ± 0.32	21.4 ± 1.4
		9 lines	2859.15	14.7	6.21 ± 0.34	11.8 ± 0.9
		11 lines	2857.5	25.4	9.13 ± 0.40	10.1 ± 0.7
		3 lines	2857.12	9.52	4.14 ± 0.27	12.2 ± 1.0
		8_3–7_3	2856.88	2.40	2.08 ± 0.24	24.3 ± 3.0
		8 lines	2856.65	17.2	4.76 ± 0.30	7.76 ± 0.62
		10 lines	2856.0	23.7	12.2 ± 0.4	14.4 ± 0.9
		4 lines	2855.5	10.6	6.29 ± 0.31	16.7 ± 1.2
		10 lines	2855.15	26.5	9.19 ± 0.38	9.72 ± 0.63
		6 lines	2853.9	17.4	7.77 ± 0.36	12.5 ± 0.9
		6 lines	2853.6	20.2	7.10 ± 0.26	9.87 ± 0.61
		6 lines	2852.7	15.3	6.73 ± 0.31	12.4 ± 0.8
		3 lines	2852.3	13.8	5.90 ± 0.29	12.0 ± 0.8
		2 lines	2851.11	11.8	5.15 ± 0.38	12.2 ± 1.1
		2 lines	2849.51	9.89	3.99 ± 0.31	11.3 ± 1.1
		2 lines	2849.17	5.61	2.06 ± 0.36	10.3 ± 1.9
		5 lines	2848.95	12.9	4.07 ± 0.41	8.83 ± 1.00
		2 lines	2846.3	3.88	2.35 ± 0.32	17.0 ± 2.5
		many	2845.8	26.0	8.80 ± 0.63	9.52 ± 0.83
		many	2844.6	38.6	16.2 ± 0.5	11.8 ± 0.7
		many	2844.1	117	32.4 ± 0.7	7.77 ± 0.42
		6 lines	2843.1	4.81	3.49 ± 0.39	20.4 ± 2.5
		10 lines	2842.05	23.0	7.71 ± 0.45	9.43 ± 0.72
		6 lines	2841.5	8.57	3.87 ± 0.31	12.7 ± 1.2
		2 lines	2839.84	11.0	3.26 ± 0.29	8.36 ± 0.85
		2 lines	2838.22	13.0	5.24 ± 0.36	11.3 ± 1.0
		5 lines	2837.8	22.5	6.70 ± 0.42	8.39 ± 0.68
		4 lines	2836.58	16.3	5.50 ± 0.32	9.54 ± 0.73

Table A6
(Continued)

Molecule	Band ID	Line ID[a]	Line Pos. (cm^{-1})[b]	g-factor (10^{-7} s^{-1})[c]	Line Flux (10^{-19} W m^{-2})[d]	Q (10^{27} s^{-1})[e]
		3 lines	2836.25	16.9	5.40 ± 0.36	9.04 ± 0.75
		5 lines	2836.0	19.7	6.52 ± 0.38	9.33 ± 0.71
		2 lines	2833.6	5.01	2.36 ± 0.29	13.3 ± 1.8
		6 lines	2833.35	20.0	7.73 ± 0.38	10.9 ± 0.8
		2 lines	2833.1	11.3	3.36 ± 0.32	8.41 ± 0.91
C$_2$H$_6$ (85 $^{+10}/_{-11}$ K)	ν_7	10 lines	3000.65	22.0	2.67 ± 0.52	3.73 ± 0.37
		$^RQ_4$	3000.29	112	17.3 ± 0.3	3.91 ± 0.21
		$^rR_2(2)$	2997.4	52.8	6.77 ± 0.32	3.24 ± 0.22
		$^RQ_2$	2993.47	242	30.3 ± 0.5	3.16 ± 0.17
		$^RQ_1$	2990.07	289	34.1 ± 0.5	2.98 ± 0.16
		$^RQ_0$	2986.72	372	52.9 ± 0.3	3.60 ± 0.18
		$^PQ_1$	2983.38	295	35.3 ± 0.3	3.03 ± 0.15
		$^PQ_2$	2980.07	245	32.3 ± 0.4	3.34 ± 0.17
		$^PQ_3$	2976.78	220	25.8 ± 0.5	2.98 ± 0.16
		6 lines	2972.78	42.5	7.16 ± 0.35	4.29 ± 0.30
		Many lines	2970.3	106	14.3 ± 0.4	3.43 ± 0.20
		6 lines	2968.16	43.3	7.13 ± 0.60	4.20 ± 0.41
		many	2966.85	70.0	9.11 ± 0.46	3.32 ± 0.24
		many	2964.3	45.5	9.55 ± 0.33	5.36 ± 0.33
		3 lines	2963.00	13.7	2.77 ± 0.28	5.17 ± 0.58
		2 lines	2962.33	17.5	2.89 ± 0.38	4.21 ± 0.59
CH$_4$ (85 K)	ν_3	P2	2999.03	106	15.4 ± 0.4	3.68 ± 0.21
		P4	2978.65	42.6	8.10 ± 0.91	4.84 ± 0.59
		P5	2968.44	37.0	7.90 ± 1.36	5.47 ± 0.98
NH$_3$ (85 K)	ν_1	2 lines	3376.3	20.3	2.44 ± 0.31	3.55 ± 0.49
H$_2$CO (100 K)	ν_5	2 lines	2853.4	25.8	1.02 ± 0.24	1.36 ± 0.32
		2 lines	2838.4	15.7	0.47 ± 0.36	1.04 ± 0.80
		$3_{12}-3_{03}$	2833.8	57.8	1.24 ± 0.30	0.74 ± 0.18
NH$_2$ (100 K)	ν_1	3 lines	3250.4	157	8.20 ± 0.31	
		$2_{20}-2_{11}$	3249.95	79.7	4.37 ± 0.39	
		2 lines	3249.1	43.4	2.21 ± 0.26	
		3 lines	3248.55	94.7	3.50 ± 0.33	
		4 lines	3239.45	226	8.95 ± 0.48	
		2 lines	3234.05	54.4	4.04 ± 0.60	
		$2_{20}-3_{31}$	3089.64	78.5	2.45 ± 0.24	
		$2_{20}-3_{31}$	3089.35	51.0	3.26 ± 0.25	
OH	$1 \rightarrow 0$	P1.5 2-/2+	3507.8		22.4 ± 2.0	
		P2.5 1+	3484.74		32.6 ± 3.4	
		P4.5 2−	3378.07		10.4 ± 0.5	
		P7.5 2+	3241.52		6.70 ± 0.41	
		P7.5 2−	3241.02		10.8 ± 0.7	
		P8.5 1+	3235.65		8.92 ± 0.31	
		P8.5 1−	3234.84		9.97 ± 0.40	
		P11.5 1−	3093.71		10.7 ± 1.4	
		P11.5 1+	3092.60		7.70 ± 0.29	
		P15.5 2+	2840.82		6.50 ± 0.33	
	$2 \rightarrow 1$	P4.5 1+	3248.13		3.36 ± 0.29	
		P7.5 1+	3124.66		4.31 ± 0.55	
		P13.5 1−	2848.10		3.43 ± 0.45	

Notes.

[a] H$_2$O line identifications indicate emissions that are ortho (o), para (p), or a blend of both (b).

[b] Rest positions for single lines or average rest positions for multiple lines.

[c] The g-factors at $R_h = 1$ au for the derived or assumed rotational temperature given below the molecular assignment in parentheses.

[d] Line fluxes within a 3 spectral $\times$ 9 spatial pixel extract ($0\rlap{.}''432 \times 1\rlap{.}''71$) centered on the peak intensity of the gas spatial profile.

[e] Derived production rates for individual lines corrected for slit losses. Uncertainties include photon noise (reflected in the S/N of individual lines) and an assumed 5% uncertainty per emission in the continuum baseline fit. Calibration and growth factor uncertainties are not included.

Table A7
Line Positions, Fluxes, and Production Rates in C/2014 Q2 (Lovejoy) on UT 2015 Feb 3 Setting M2

Molecule	Band ID	Line ID[a]	Line Pos. (cm^{-1})[b]	g-factor (10^{-7} s^{-1})[c]	Line Flux (10^{-19} W m^{-2})[d]	Q (10^{27} s^{-1})[e]
H$_2$O (88 ± 5 K)	$\nu_1 + \nu_3 - 2\nu_2$	0_{00}–1_{01} (o)	2155.82	0.76	18.8 ± 3.7	635 ± 130
	$\nu_3 - \nu_2$	1_{11}–1_{10} (o)	2151.20	4.29	136 ± 8	817 ± 61
	$\nu_1 - \nu_2$	2_{21}–1_{10} (o)	2148.19	1.21	45.3 ± 3.8	966 ± 95
	$\nu_3 - \nu_2$	2_{20}–2_{21} (o)	2144.81	2.11	52.4 ± 3.9	641 ± 57
	blend	2 lines (p)	2142.25	0.73	16.9 ± 2.9	601 ± 107
	$\nu_3 - \nu_2$	2 lines (o)	2137.36	5.37	129 ± 22	622 ± 111
	$\nu_2 + \nu_3 - 2\nu_2$	1_{01}–2_{02} (p)	2132.91	0.37	10.3 ± 2.9	713 ± 206
	$\nu_1 - \nu_2$	0_{00}–1_{11} (p)	2022.09	1.30	44.6 ± 5.5	1366 ± 181
	$\nu_3 - \nu_2$	4_{22}–5_{23} (o)	2012.15	0.25	13.3 ± 5.3	2134 ± 850
	$\nu_1 - \nu_2$	1_{01}–2_{12} (o)	2003.39	4.34	92.0 ± 4.6	849 ± 60
		2_{12}–3_{03} (o)	2003.00	2.58	74.1 ± 4.2	1152 ± 86
CO (58 ± 8 K)	$1 \rightarrow 0$	R3	2158.30	187	117 ± 5	19.6 ± 1.3
		R2	2154.60	198	118 ± 4	18.7 ± 1.2
		R1	2150.86	171	98.7 ± 4.2	18.2 ± 1.2
		R0	2147.08	102	80.8 ± 4.0	25.1 ± 1.8
		P1	2139.43	111	66.2 ± 7.4	18.9 ± 2.3
		P2	2135.55	204	118 ± 3	18.3 ± 1.1
		P3	2131.63	257	154 ± 4	19.0 ± 1.1
		P4	2127.68	265	180 ± 12	21.7 ± 1.8

Notes.

[a] H$_2$O line identifications indicate emissions that are ortho (o), para (p), or a blend of both (b).

[b] Rest positions for single lines or average rest positions for multiple lines.

[c] The g-factors at $R_h = 1$ au for the derived or assumed rotational temperature given below the molecular assignment in parentheses.

[d] Line fluxes within a 3 spectral × 9 spatial pixel extract ($0\rlap{.}{''}432 \times 1\rlap{.}{''}71$) centered on the peak intensity of the gas spatial profile.

[e] Derived production rates for individual lines corrected for slit losses. Uncertainties include photon noise (reflected in the S/N of individual lines) and an assumed 5% uncertainty per emission in the continuum baseline fit. Calibration and growth factor uncertainties are not included.

Table A8
Setting-by-setting Characteristics of Volatile Spatial Profiles

Molecule	Setting	Order	Multiplicative Growth Factor[a]	Differences (Volatile – Dust)		Sunward/Antisunward[d]
				HWHM (pixels)[b]	Peak Position (pixels)[c]	
H_2O	KL3	25	1.56 ± 0.03	0.20 ± 0.14	0.21 ± 0.12	0.91 ± 0.03
		26	1.53 ± 0.03	0.32 ± 0.14	0.11 ± 0.13	0.85 ± 0.03
	KL1	26	1.52 ± 0.03	0.10 ± 0.15	0.12 ± 0.14	0.79 ± 0.03
		27	1.63 ± 0.04	0.73 ± 0.33	-0.10 ± 0.29	1.01 ± 0.06
	KL2	25	1.61 ± 0.04	0.76 ± 0.30	0.14 ± 0.26	1.07 ± 0.06
		26	1.59 ± 0.03	0.35 ± 0.14	0.13 ± 0.12	0.98 ± 0.03
	M1	16	1.69 ± 0.04	0.64 ± 0.20	-0.15 ± 0.17	1.02 ± 0.04
	AVERAGE	FEB 2	$\mathbf{1.58 \pm 0.02}$	$\mathbf{0.33 \pm 0.07}$	$\mathbf{0.10 \pm 0.06}$	$\mathbf{0.91 \pm 0.03}$
	KL4	25	2.15 ± 0.06	0.40 ± 0.29	-0.72 ± 0.25	1.04 ± 0.06
		26	2.10 ± 0.06	0.30 ± 0.20	-0.08 ± 0.17	1.00 ± 0.04
	KL5	26	2.41 ± 0.07	0.10 ± 0.18	0.29 ± 0.15	0.97 ± 0.03
		27	2.39 ± 0.07	-0.43 ± 0.46	-0.48 ± 0.38	0.88 ± 0.09
	M2	16	1.77 ± 0.09	0.23 ± 0.38	0.30 ± 0.34	0.86 ± 0.08
	AVERAGE	FEB 3	$\mathbf{2.19 \pm 0.09}$	$\mathbf{0.19 \pm 0.11}$	$\mathbf{-0.02 \pm 0.16}$	$\mathbf{0.97 \pm 0.02}$
CO	M1	**16**	$\mathbf{1.65 \pm 0.04}$	$\mathbf{0.51 \pm 0.13}$	$\mathbf{1.10 \pm 0.11}$	$\mathbf{1.22 \pm 0.03}$
	M2	**16**	$\mathbf{2.17 \pm 0.06}$	$\mathbf{1.39 \pm 0.26}$	$\mathbf{1.06 \pm 0.22}$	$\mathbf{0.96 \pm 0.07}$
CH_3OH	KL3	22	1.57 ± 0.03	0.37 ± 0.13	0.31 ± 0.12	0.99 ± 0.03
	KL1	22	1.54 ± 0.03	0.40 ± 0.16	0.48 ± 0.14	1.08 ± 0.03
		23	1.53 ± 0.03	0.03 ± 0.12	0.45 ± 0.11	0.91 ± 0.03
	KL2	22	1.53 ± 0.03	-0.18 ± 0.16	0.37 ± 0.15	0.79 ± 0.04
		23	1.52 ± 0.03	-0.58 ± 0.17	0.72 ± 0.15	0.80 ± 0.04
	AVERAGE	FEB 2	$\mathbf{1.54 \pm 0.02}$	$\mathbf{0.05 \pm 0.15}$	$\mathbf{0.45 \pm 0.06}$	$\mathbf{0.94 \pm 0.05}$
	KL4	22	2.20 ± 0.11	0.69 ± 0.18	0.15 ± 0.15	1.05 ± 0.03
	KL5	22	2.56 ± 0.07	-0.22 ± 0.25	0.97 ± 0.20	0.99 ± 0.04
		23	2.70 ± 0.08	0.55 ± 0.23	1.27 ± 0.18	1.05 ± 0.04
	AVERAGE	FEB 3	$\mathbf{2.54 \pm 0.10}$	$\mathbf{0.43 \pm 0.21}$	$\mathbf{0.70 \pm 0.29}$	$\mathbf{1.03 \pm 0.02}$
C_2H_6	KL3	22	1.56 ± 0.03	0.20 ± 0.12	0.46 ± 0.11	1.08 ± 0.03
	KL1	23	1.53 ± 0.03	-0.03 ± 0.11	0.53 ± 0.10	1.00 ± 0.03
	KL2	22	1.59 ± 0.03	0.14 ± 0.14	0.41 ± 0.12	0.89 ± 0.03
	AVERAGE	FEB 2	$\mathbf{1.56 \pm 0.02}$	$\mathbf{0.09 \pm 0.07}$	$\mathbf{0.47 \pm 0.06}$	$\mathbf{0.99 \pm 0.04}$
	KL4	22	2.13 ± 0.06	0.33 ± 0.17	0.69 ± 0.14	1.08 ± 0.04
	KL5	23	2.42 ± 0.07	-0.01 ± 0.19	1.40 ± 0.15	1.13 ± 0.04
	AVERAGE	FEB 3	$\mathbf{2.25 \pm 0.10}$	$\mathbf{0.18 \pm 0.13}$	$\mathbf{1.02 \pm 0.25}$	$\mathbf{1.10 \pm 0.03}$
CH_4	KL3	23	1.55 ± 0.03	0.08 ± 0.11	0.78 ± 0.10	1.11 ± 0.03
	KL1	23	1.49 ± 0.03	-0.12 ± 0.14	0.52 ± 0.12	1.01 ± 0.03
	KL2	23	1.84 ± 0.07	0.11 ± 0.12	0.61 ± 0.11	1.00 ± 0.03
	AVERAGE	FEB 2	$\mathbf{1.55 \pm 0.05}$	$\mathbf{0.04 \pm 0.07}$	$\mathbf{0.65 \pm 0.06}$	$\mathbf{1.04 \pm 0.03}$
	KL4	23	2.13 ± 0.06	0.30 ± 0.22	1.14 ± 0.18	1.20 ± 0.04
	KL5	23	2.42 ± 0.09	0.78 ± 0.43	1.41 ± 0.34	1.30 ± 0.08
	AVERAGE	FEB 3	$\mathbf{2.22 \pm 0.10}$	$\mathbf{0.40 \pm 0.20}$	$\mathbf{1.20 \pm 0.16}$	$\mathbf{1.22 \pm 0.04}$
HCN	KL3	25	1.52 ± 0.03	-0.04 ± 0.12	0.54 ± 0.11	0.99 ± 0.03
	KL2	25	1.57 ± 0.03	0.00 ± 0.12	0.59 ± 0.11	0.92 ± 0.03
	AVERAGE	FEB 2	$\mathbf{1.54 \pm 0.02}$	$\mathbf{-0.02 \pm 0.08}$	$\mathbf{0.56 \pm 0.08}$	$\mathbf{0.96 \pm 0.03}$
	KL4	**25**	$\mathbf{2.17 \pm 0.06}$	$\mathbf{0.34 \pm 0.22}$	$\mathbf{1.12 \pm 0.18}$	$\mathbf{1.05 \pm 0.05}$
C_2H_2	KL3	25	3.45 ± 0.08	0.49 ± 0.30	0.34 ± 0.26	0.90 ± 0.06
	KL2	25	2.67 ± 0.07	1.01 ± 0.24	0.33 ± 0.21	0.89 ± 0.05
	AVERAGE	FEB 2	$\mathbf{3.01 \pm 0.27}$	$\mathbf{0.81 \pm 0.19}$	$\mathbf{0.33 \pm 0.16}$	$\mathbf{0.89 \pm 0.04}$
NH_3	KL3	25	1.76 ± 0.11	0.71 ± 0.42	-0.09 ± 0.37	1.04 ± 0.10
		26	1.55 ± 0.10	-0.14 ± 0.41	0.23 ± 0.37	0.86 ± 0.10
	KL1	26	1.75 ± 0.09	1.47 ± 0.52	-0.99 ± 0.44	0.66 ± 0.13
	KL2	25	2.41 ± 0.10	1.52 ± 0.54	0.62 ± 0.45	0.93 ± 0.14
		26	2.14 ± 0.09	0.13 ± 0.32	-0.38 ± 0.29	1.21 ± 0.08
	AVERAGE	FEB 2	$\mathbf{1.93 \pm 0.14}$	$\mathbf{0.53 \pm 0.28}$	$\mathbf{-0.15 \pm 0.21}$	$\mathbf{1.00 \pm 0.08}$
H_2CO	KL3	21	4.04 ± 0.10	1.66 ± 0.36	0.06 ± 0.30	0.86 ± 0.07
	KL2	21	4.08 ± 0.10	0.93 ± 0.33	-0.40 ± 0.28	0.83 ± 0.07
	AVERAGE	FEB 2	$\mathbf{4.06 \pm 0.07}$	$\mathbf{1.26 \pm 0.26}$	$\mathbf{-0.19 \pm 0.20}$	$\mathbf{0.84 \pm 0.05}$
	KL4	**21**	$\mathbf{4.61 \pm 0.14}$	$\mathbf{0.49 \pm 0.37}$	$\mathbf{-1.41 \pm 0.31}$	$\mathbf{1.04 \pm 0.07}$
OH $1 \rightarrow 0$	KL3	21		1.16 ± 0.19	-0.33 ± 0.17	0.93 ± 0.04
		22		1.26 ± 0.19	-0.94 ± 0.16	0.93 ± 0.04
		23		1.28 ± 0.14	-0.82 ± 0.12	0.97 ± 0.03
		24		1.71 ± 0.21	-0.88 ± 0.18	0.88 ± 0.04
		25		1.03 ± 0.18	-0.31 ± 0.16	0.96 ± 0.04
		26		1.27 ± 0.16	-0.52 ± 0.14	0.85 ± 0.04

Table A8
(Continued)

Molecule	Setting	Order	Multiplicative Growth Factor[a]	Differences (Volatile – Dust)		Sunward/Antisunward[d]
				HWHM (pixels)[b]	Peak Position (pixels)[c]	
	KL1	24		0.74 ± 0.47	−0.52 ± 0.41	0.77 ± 0.10
		25		1.44 ± 0.21	−0.72 ± 0.18	0.89 ± 0.04
		27		0.91 ± 0.21	−0.62 ± 0.19	0.81 ± 0.05
	KL2	22		1.37 ± 0.20	−0.77 ± 0.17	0.94 ± 0.04
		23		1.27 ± 0.15	−0.88 ± 0.13	0.96 ± 0.03
		24		1.35 ± 0.19	−0.48 ± 0.16	0.87 ± 0.04
		25		1.69 ± 0.22	−0.78 ± 0.18	0.90 ± 0.04
		26		1.01 ± 0.16	−0.50 ± 0.14	0.90 ± 0.04
	AVERAGE	**FEB 2**		**1.26 ± 0.06**	**−0.66 ± 0.05**	**0.91 ± 0.01**
	KL4	21		1.23 ± 0.41	−0.71 ± 0.33	0.99 ± 0.08
		23		1.53 ± 0.20	−0.83 ± 0.16	0.95 ± 0.04
		24		1.68 ± 0.30	−0.59 ± 0.24	0.94 ± 0.06
		25		0.66 ± 0.33	−0.23 ± 0.27	0.94 ± 0.07
		26		0.99 ± 0.35	−0.50 ± 0.28	0.87 ± 0.07
	KL5	25		1.32 ± 0.30	−0.42 ± 0.24	0.77 ± 0.06
	AVERAGE	**FEB 3**		**1.32 ± 0.13**	**−0.60 ± 0.10**	**0.91 ± 0.03**
OH 2 → 1	KL3	23		0.81 ± 0.14	−0.89 ± 0.12	0.96 ± 0.03
		24		1.71 ± 0.21	−0.42 ± 0.18	0.90 ± 0.04
		25		0.83 ± 0.26	−0.12 ± 0.23	0.91 ± 0.06
	KL1	24		2.31 ± 0.55	−0.43 ± 0.44	0.93 ± 0.11
		25		1.52 ± 0.30	0.13 ± 0.26	1.04 ± 0.07
	KL2	21		1.07 ± 0.36	−0.38 ± 0.31	0.79 ± 0.08
		23		1.28 ± 0.21	−0.75 ± 0.18	1.04 ± 0.04
		24		2.67 ± 0.50	−0.99 ± 0.39	0.92 ± 0.10
		25		0.67 ± 0.18	−0.58 ± 0.16	0.97 ± 0.04
	AVERAGE	**FEB 2**		**1.10 ± 0.16**	**−0.59 ± 0.10**	**0.96 ± 0.02**
	KL4	23		1.45 ± 0.31	−0.33 ± 0.24	0.87 ± 0.06
		24		0.18 ± 0.43	−0.80 ± 0.37	1.18 ± 0.09
		25		1.83 ± 0.58	−0.25 ± 0.45	0.65 ± 0.11
	AVERAGE	**FEB 3**		**1.14 ± 0.36**	**−0.43 ± 0.18**	**0.91 ± 0.10**
OH 3 → 2	**KL2**	**24**		**2.09 ± 0.60**	**−0.57 ± 0.49**	**0.76 ± 0.19**
NH_2	KL3	24		2.66 ± 0.37	−0.56 ± 0.29	0.95 ± 0.07
		25		4.18 ± 0.89	−1.20 ± 0.63	0.88 ± 0.16
	KL1	25		2.19 ± 0.55	0.03 ± 0.45	1.04 ± 0.11
	KL2	24		−0.17 ± 0.36	−0.55 ± 0.32	0.91 ± 0.08
		25		3.01 ± 0.54	−0.13 ± 0.40	0.98 ± 0.10
	AVERAGE	**FEB 2**		**1.78 ± 0.65**	**−0.44 ± 0.17**	**0.95 ± 0.04**
	KL4	**24**		**2.28 ± 0.60**	**−0.43 ± 0.46**	**1.01 ± 0.12**

Notes.

[a] Multiplicative growth factors calculated independently for each parent molecule within a setting.

[b] The difference in the spatial profile half-width at half-maximum between the volatile and co-measured dust in pixels (each pixel represents a projected distance at the comet of ∼110 km in the spatial direction). Positive values represent a broader volatile profile compared with the dust, whereas negative values indicate a narrower profile.

[c] The difference between the spatial profile peak position of the volatile and the co-measured dust. Positive values represent a sunward volatile shift, negative values, and antisunward volatile shift.

[d] The symmetry of the spatial profile as measured by the ratio of sunward to antisunward flux along the slit, excluding the central 5 pixels around the peak flux position. Boldface values are daily averages listed in Table 4 and are used for the points in the graph shown in Figure 10 (except for OH 2 → 1 and 3 → 2).

Table A9
Spatial Profile Characteristics of the 16 Strongest Unidentified Emissions

Line Rest Position	Settings	Line ID[a]	Order	HWHM (pixels)[b]	Peak Position (pixels)[c]
2763.23	KL2	1	21	1.15 ± 0.43	0.34 ± 0.37
3150.82	KL2	2	24	2.25 ± 0.49	-0.76 ± 0.39
3165.37[d]	KL2/KL3	3	24	1.81 ± 0.64 2.20 ± 0.26 **2.14 ± 0.24**	-1.44 ± 0.53 -1.16 ± 0.22 **-1.20 ± 0.20**
3165.62[d]	KL2/KL3	4	24	0.59 ± 0.53 2.17 ± 0.40 **1.60 ± 0.54**	-1.22 ± 0.46 -0.67 ± 0.32 **-0.85 ± 0.26**
3176.88[e]	KL2/KL3	5	24	2.41 ± 0.52 1.46 ± 0.27 **1.66 ± 0.27**	-1.01 ± 0.41 -0.88 ± 0.23 **-0.91 ± 0.20**
3193.93[e]	KL3	6	24	0.93 ± 0.33	-0.30 ± 0.28
3236.40	KL1	7	25	1.27 ± 0.56	0.40 ± 0.47
3299.95[e]	KL2/KL3	8	25	2.80 ± 0.35 1.31 ± 0.28 **1.89 ± 0.51**	-0.31 ± 0.27 -1.15 ± 0.24 **-0.78 ± 0.29**
3372.56[d]	KL1	9	26	2.11 ± 0.45	-0.28 ± 0.37
3402.89[d,e]	KL2	10	26	1.28 ± 0.26	-0.78 ± 0.28
3408.51[e]	KL2	11	26	0.47 ± 0.27	-0.96 ± 0.23
3414.53[d,e]	KL2	12	26	1.19 ± 0.19	-0.48 ± 0.16
3432.28[e]	KL3	13	26	-0.43 ± 0.25	0.99 ± 0.23
3435.96[d]	KL3	14	26	0.33 ± 0.19	-0.40 ± 0.17
3445.16	KL3	15	26	0.30 ± 0.18	-0.60 ± 0.16
3453.88[d,e]	KL3	16	26	1.04 ± 0.23	-0.61 ± 0.20

Notes.

[a] Line IDs correspond to the points on the graph in Figure A8.

[b] The difference in the spatial profile half-width at half-maximum of the unidentified emission and co-measured dust in pixels (on these dates each pixel represents a projected distance at the comet of ~110 km). Positive values indicate a broader profile than the co-measured dust. Multiple entries indicate detections in two settings with the average values in bold.

[c] The difference in spatial profile peak position of the unidentified emission and co-measured dust. Positive values represent a sunward shift, negative values an antisunward shift. Multiple entries indicate detections in two settings with the average values in bold.

[d] Lines detected in a survey of comet C/1999 H1 (Lee) (Dello Russo et al. 2006).

[e] Lines detected in a survey of comet 103P/Hartley 2 (Dello Russo et al. 2013).

ORCID iDs

Neil Dello Russo ⬤ https://orcid.org/0000-0002-8379-7304
Ronald J. Vervack, Jr. ⬤ https://orcid.org/0000-0002-8227-9564
Hideyo Kawakita ⬤ https://orcid.org/0000-0003-2011-9159
Boncho P. Bonev ⬤ https://orcid.org/0000-0002-6391-4817
Michael A. DiSanti ⬤ https://orcid.org/0000-0001-8843-7511
Erika L. Gibb ⬤ https://orcid.org/0000-0003-0142-5265
Adam J. McKay ⬤ https://orcid.org/0000-0002-0622-2400
Anita L. Cochran ⬤ https://orcid.org/0000-0003-4828-7787
Harold A. Weaver ⬤ https://orcid.org/0000-0003-0951-7762
Nicolas Biver ⬤ https://orcid.org/0000-0003-2414-5370
Dominique Bockelée-Morvan ⬤ https://orcid.org/0000-0002-8130-0974
Hitomi Kobayashi ⬤ https://orcid.org/0000-0002-1632-5489
Walter M. Harris ⬤ https://orcid.org/0000-0002-8378-4503
Nathan X. Roth ⬤ https://orcid.org/0000-0002-6006-9574
Mohammad Saki ⬤ https://orcid.org/0000-0003-2277-6232
Younas Khan ⬤ https://orcid.org/0000-0003-4773-2674

References

A'Hearn, M. F., Millis, R. L., Schleicher, D. G., Osip, D. J., & Birch, P. V. 1995, Icar, 118, 223
A'Hearn, M. F., Belton, M. J. S, Delamere, W. A., et al. 2011, Sci, 332, 1396
Altwegg, K., Balsiger, H., Berthelier, J. J., et al. 2017, MNRAS, 469, S130
Altwegg, K., Balsiger, H., Hänni, N., et al. 2020, NatAs, 4, 533
Biver, N., Bockelée-Morvan, D., Moreno, R., et al. 2015, SciA, 1, e1500863
Biver, N., Moreno, R., Bockelée-Morvan, D., et al. 2016, A&A, 589, A78
Bockelée-Morvan, D., & Biver, N. 2017, RSPTA, 375, 20160252
Bockelée-Morvan, D., Boissier, J., Biver, N., & Crovisier, J. 2010, Icar, 210, 898
Bonev, B. P. 2005, PhD thesis, Univ. Toledo, http://astrobiology.gsfc.nasa.gov/Bonev_thesis.pdf
Bonev, B. P., Mumma, M. J., DiSanti, M. A., et al. 2006, ApJ, 653, 774
Bonev, B. P., Mumma, M. J., Villanueva, G. L., et al. 2007, ApJL, 661, L97
Bonev, B. P., Villanueva, G. L., Paganini, L., et al. 2013, Icar, 222, 740
Bonev, B. P., DiSanti, M. A., Villanueva, G. L., et al. 2014, ApJL, 796, L6
Bonev, B. P., Dello Russo, N., DiSanti, M. A., et al. 2021, PSJ, 2, 45
Cochran, A. L., Barker, E. S., & Gray, C. L. 2012, Icar, 218, 144
Combi, M. R., Mäkinen, T. T., Bertaux, J.-L., et al. 2018, Icar, 300, 33
Cordiner, M. A., Remijan, A. J., Boissier, J., et al. 2014, ApJL, 792, L2
Cottin, H., & Fray, N. 2008, SSRv, 138, 179
Dello Russo, N., Bonev, B. P., DiSanti, M. A., et al. 2005, ApJ, 621, 537
Dello Russo, N., DiSanti, M. A., Mumma, M. J., Magee-Sauer, K., & Rettig, T. W. 1998, Icar, 135, 377
Dello Russo, N., Kawakita, H., Vervack, R. J., & Weaver, H. A. 2016a, Icar, 278, 301
Dello Russo, N., Mumma, M. J., DiSanti, M. A., et al. 2000, Icar, 143, 324
Dello Russo, N., Mumma, M. J., DiSanti, M. A., Magee-Sauer, K., & Novak, R. 2001, Icar, 153, 162
Dello Russo, N., DiSanti, M. A., Magee-Sauer, K., et al. 2004, Icar, 168, 186
Dello Russo, N., Mumma, M. J., DiSanti, M. A., et al. 2006, Icar, 184, 255
Dello Russo, N., Vervack, R. J., Weaver, H. A., et al. 2007, Natur, 448, 172
Dello Russo, N., Vervack, R. J., Lisse, C. M., et al. 2011, ApJL, 734, L8
Dello Russo, N., Vervack, R. J., Jr., Weaver, H. A., et al. 2013, Icar, 222, 707
Dello Russo, N., Vervack, R. J., Kawakita, H., et al. 2016b, Icar, 266, 152
de Val-Borro, M., Milam, S. N., Cordiner, M. A., et al. 2018, MNRAS, 474, 1099
DiSanti, M. A., Bonev, B. P., Magee-Sauer, K., et al. 2006, ApJ, 650, 470
DiSanti, M. A., Bonev, B. P., Villanueva, G. L., & Mumma, M. J. 2013, ApJ, 763, 1
DiSanti, M. A., Mumma, M. J., Dello Russo, N., et al. 1999, Natur, 399, 662
DiSanti, M. A., Mumma, M. J., Dello Russo, N., et al. 2001, Icar, 153, 361
DiSanti, M. A., Villanueva, G. L., Paganini, L., et al. 2014, Icar, 228, 167
DiSanti, M. A., Bonev, B. P., Gibb, E. L., et al. 2016, ApJ, 820, 34
Dudley, W. W., & Hu, A. 2009, ApJ, 698, 808
Duvernay, F., Rimola, A., Theule, P., et al. 2014, PCCP, 16, 24200
Eberhardt, P. 1999, SSRv, 90, 45
Escamilla-Roa, E., & Sainz-Diaz, C. I. 2014, J. Phys. Chem. C., 118, 3554
Faggi, S., Villanueva, G. L., Mumma, M. J., et al. 2016, ApJ, 830, 157
Faure, A., Hily-Blant, P., Rist, C., et al. 2019, MNRAS, 487, 3392
Feldman, P. D., Weaver, H. A., A'Hearn, M. F., Combi, M. R., & Dello Russo, N. 2018, AJ, 155, 193

Fink, U. 2009, Icar, 201, 311

Fray, N., Bénilan, Y., Biver, N., et al. 2006, Icar, 184, 239

Geiss, J., Altwegg, K., Anders, E., et al. 1991, A&A, 247, 226

Gibb, E. L., Mumma, M. J., Dello Russo, N., DiSanti, M. A., & Magee-Sauer, K. 2003, Icar, 165, 391

Gomes, R., Levison, H. L., Tsiganis, K., & Morbidelli, A. 2005, Natur, 435, 466

Hama, T., Kouchi, A., & Watanabe, N. 2018, ApJL, 857, L13

Hiraoka, K., Takayama, T., Euchi, A., Handa, H., & Sato, T. 2000, ApJ, 532, 1029

Huebner, W. F., Keady, J. J., & Lyon, S. P. 1992, Ap&SS, 195, 1

Huebner, W. F., & Mukherjee, J. 2015, P&SS, 106, 11

Jackson, W. M. 1976, in Goddard Space Flight Center The Study of Comets, Part 2 (NASA SP-393) (Goddard Space Flight Center) ed. B. Donn et al. (Washington, DC: NASA), 679

Kawakita, H., & Mumma, M. J. 2011, ApJ, 727, 91

Kawakita, H., Watanabe, J., Furusho, R., Fuse, T., & Boice, D. C. 2005, ApJL, 623, L49

Kawakita, H., Kobayashi, H., Dello Russo, N., et al. 2013, Icar, 222, 723

Kleiner, I., Brown, L. R., Tarrago, G., et al. 1999, JMoSp, 193, 46

Kobayashi, H., Hidaka, H., Lamberts, T., et al. 2017, ApJ, 833, 155

Langland-Shula, L. E., & Smith, G. H. 2011, Icar, 213, 280

Lippi, M., Villanueva, G. L., Mumma, M. J., & Faggi, S. 2021, AJ, 162, 74

Luspay-Kuti, A., Hässig, M, Fuselier, S. A., et al. 2015, A&A, 583, A4

McLean, I. A., Becklin, E. E., Bendiksen, O., et al. 1998, Proc. SPIE, 3354, 566

Meier, R., Eberhardt, P., & Krankowsky, H. R. R. 1993, A&A, 277, 677

Miani, A., & Tennyson, J. 2004, JChPh, 120, 2732

Mumma, M. J., & Charnley, S. B. 2011, ARA&A, 49, 471

Mumma, M. J., Bonev, B. P., Villanueva, G. L., et al. 2011, ApJL, 734, L7

Paganini, L., Mumma, M. J., Gibb, E. L., & Villanueva, G. L. 2017, ApJL, 836, L25

Paganini, L., Mumma, M. J., Villanueva, G. L., et al. 2014, ApJ, 791, 122

Pine, A. S., & Dang-Nhu, M. 1993, JQSRT, 50, 565

Poch, O., Istiqomah, I., Quirico, E., et al. 2020, Sci, 367, eaaw7462

Rubin, M., Altwegg, K., Balsiger, H., et al. 2015, Sci, 348, 232

Schleicher, D. G., & Bair, A. N. 2011, AJ, 141, 177

Schleicher, D. G., Farnham, T. L., & Bair, A. N. 2007, Workshop on Planetary Atmospheres, LPI Contribution No. 1376, 103

Serra-Ricart, M., & Licandro, J. 2015, ApJ, 814, 49

Shinnaka, Y., & Kawakita, H. 2016, AJ, 154, 145

Tsiganis, K., Gomes, R., Morbidelli, A., & Levison, H. F. 2005, Natur, 435, 459

Tzeli, D., Mavridis, A., & Xantheas, S. S. 2000, JChPh, 112, 6178

Venkataramani, K., Ghetiya, S., Ganesh, S., et al. 2016, MNRAS, 463, 2137

Villanueva, G. L., Mumma, M. J., DiSanti, M. A., et al. 2011a, Icar, 216, 227

Villanueva, G. L., Mumma, M. J., Bonev, B. P., DiSanti, M. A., & Gibb, E. L. 2009, ApJL, 690, L5

Villanueva, G. L., Mumma, M. J., Bonev, B. P., et al. 2012, JQSRT, 113, 202

Villanueva, G. L., Mumma, M. J., & Magee-Sauer, K. 2011b, JGR, 116, E8

Villanueva, G. L., Mumma, M. J., Novak, R. E., & Hewagama, T. 2008, JQSRT, 109, 883

Villanueva, G. L., Mumma, M. J., Novak, R. E., et al. 2015, Sci, 348, 218

Villanueva, G. L., Smith, M. D., Protopapa, S., Faggi, S., & Mandell, A. M. 2018, JQSRT, 217, 86

Wirström, E. S., Lerner, M. S., Källström, P., et al. 2016, A&A, 588, A72

Xie, X., & Mumma, M. J. 1996, ApJ, 464, 457